

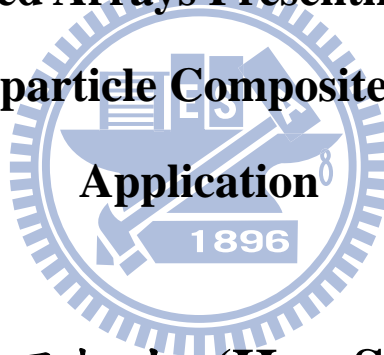
國立交通大學

材料科學與工程學系

博士論文

共軛高分子/奈米顆粒陣列結構應用於高分子太陽能
電池之研究

**Nanostructured Arrays Presenting Conjugated
Polymer/Nanoparticle Composite for Solar Cells
Application**



研究生：王旭生 (Hsu-Shen Wang)

指導教授：韋光華 (Kung-Hwa Wei)

中華民國 九十九年七月

Abstract

The main objective of this dissertation is to study the performance of polymer heterojunction solar cell involving conjugated polymers/nanoparticles incorporating nanostructured rod arrays of device. In the introduction of this dissertation, we gave an explanation on the historical evolution of polymer nanocomposites heterojunction solar cell, and summarized the literatures in the recent years. In the chapter 2, we have used melt-assisted wetting of porous alumina templates to prepare ordered core-shell nanorod arrays of poly(3-hexylthiophene) (P3HT) and [6,6]-phenyl-C₆₁-butyric acid methyl ester (PCBM). This particular core-shell nanorod arrays are characterized by using transmission electron microscopy and conductance atomic force microscopy, which revealed the presence of phase-separated shell (p-type) and core (n-type) regions. Under illumination, we observed a variation of several picoamperes between the currents in the core and shell regions of the P3HT/PCBM nanorod arrays. In the chapter 3, the internal quantum efficiencies (IQE) and external quantum efficiencies (EQE) of these core/shell nanorod inverted solar cells were higher than those of the corresponding conventional inverted bulk heterojunction device. The optimized nanorod array structure had a high hole mobility that was over one order magnitude greater than that of the conventional BHJ structure, as determined by fitting the dark $J-V$ curves into the space charge-limited current model. The more efficient carrier transport of the device incorporating the core/shell nanorod arrays provided it with both a higher short-circuit current density and power conversion efficiency. The rod array devices incorporating titanium dioxide nanorod/P3HT were discussed in chapter 4. This arrays was revealed that phase-separated TiO₂ rich (n-type) and P3HT rich (p-type) regions. The optimized composite array structure had a higher hole mobility than that

of the film consisting of TiO₂ nanorod and P3HT blend evidenced by fitting the dark *J–V* curves into the space charge–limited current model.

In the chapter 5, we have used Grignard metathesis polymerization to prepare poly(3-hexylthiophene)-based copolymers containing electron-withdrawing 4-*tert*-butylphenyl-1,3,4-oxadiazole-phenyl moieties as side chains. The quenching effects was observed in the photoluminescence spectra of the copolymers incorporating pendent electron-deficient 1,3,4-oxadiazole moieties on the side chains. The photocurrents of devices were enhanced in the presence of an optimal amount of the 1,3,4-oxadiazole moieties, thereby leading to improved power conversion efficiencies.

摘要

本論文利用陽極氧化鋁(AAO)模板製備聚共軛高分子/奈米顆粒一維奈米棒陣列結構後分別針對陣列奈米結構分析、太陽能電池元件的結構設計以及奈米棒尺寸對元件效率的影響等逐步深入探討。其中依序針對奈米結構與元件性質探討：(1)穿隧式電子顯微鏡與導電模式之原子力顯微鏡分析奈米棒之殼層結構、(2)奈米棒尺寸部分：針對一系列不同尺寸的奈米棒尺寸對元件的內部量子轉換效率、外部量子轉換效率與太陽能電池元件效率的影響進行研究、(3)太陽能電池元件結構部分：針對一般結構(normal structure)與反式結構(inverted structure)來討論不同元件結構對元件效率的影響、(4)研究奈米棒的電洞傳導與元件效率的關係、(5)導入不同奈米顆粒於此一維陣列結構中，增加其在太陽能電池元件研究的廣度。我們可以非常有系統的找出元件效率與奈米棒陣列結構間的關聯性。此完整的研究內容對未來高效率高分子太陽能電池的製作極具貢獻，其研究充分的被參考及引用。

此外，高分子太陽能電池的新材料開發上我們使用Grignard metathesis聚合法合成一系列具有強拉電子oxadiazole (OXD)基團之共軛高分子。在導入最佳比例的拉電子OXD基團下，使高分子在適度的結晶條件下以及在短波長區域(~304nm)具備額外的吸收波段，進而提升了高分子太陽能電池元件之效率。

致謝

近六年的博士生涯中首先要感謝指導教授韋光華老師在學術論文寫作與科學研究的指導。感謝口試委員王玉麟老師、黃華宗老師、林宏洲老師、鄭有舜博士、郭宗枋老師、陳方中老師百忙中撥空蒞臨口試，提供寶貴的意見使論文更趨完善。

在論文研究過程中，特別感謝王玉麟老師與陳師詠同學於實驗上的支持與協助使研究能順利進展且使成果更加完善。感謝郭宗枋老師與蕭宇哲同學在元件製備上的討論與經驗分享。感謝已畢業的的學長葉孝蔚博士、翁錦成博士、李中斌博士、黃清茂博士在奈米複合材料分析技術上的指導與經驗分享；周嘉宏博士、張耀德博士在聚合物材料合成與分子結構設計上的指導與經驗分享；感謝一起建立實驗室有機光電元件製程設備的夥伴：邱茂源、許碩麟、蘇明鑫等人；另外感謝我帶的學妹林莉華在實驗上的熱心參與及協助；許碩麟、陳冠宇、袁茂川、江建銘、游士彬學弟在材料合成上的相互討論讓我獲益良多；感謝學妹張含章對量子點合成的經驗分享；也感謝學長姐、同學與學弟妹們在實驗與實驗室事務的協助及精神上的支持，於此感謝田運宜、周靜怡、李世莉、劉曉雯、郭芝吟、許毓倩、林慧妮、陳振平、陳家閔、許昌隆、紀傑元、陳紘揚、劉永盛、吳宗諭、余璨丞、林柏宇、周奕任以及其他許多學弟妹之多方協助；歷年來行政助理們在行政事務上的處理與幫忙。感謝童學長在洛杉磯機場的鼎力相助，讓那趟難忘的美國迷航記以最戲劇化的方式完美落幕。

最後感激媽媽以及家人在精神上的鼓勵與生活上的支持與包容。老弟們在求學過程中的鼓勵；好友偉聖、嘉駿、攬揚、逸恆、義智、宏義的支持與鼓勵，使我可以走過在此一階段所遇見的種種挫折完成學業，在此致以誠摯的感激。

Table of Content

Abstract	i
摘要	iii
Figure List	vii
Scheme and Table List	xii
Appendix List	xiv
Chapter 1: Introduction	1
1-1 Introduction of Polymer Solar cell.....	1
1-2 The Principle of Polymer Solar Cell.....	2
1-2-1 Mechanisms leading to the charge generation and collection in organics.....	2
1-2-2 Characterization of a solar cell device.....	6
1-3 Literature Review of Polymer Solar Cell.....	8
1-3-1 Materials: Polymers and Inorganic Nanocrystals.....	8
1-3-2 the wetting transition in nanopores of conjugated polymer.....	11
1-3-3 Inverted solar cell.....	14
1-4 Motivation.....	15
Chapter 2: Ordered Polythiophene/Fullerene Composite Core–Shell Nanorod Arrays for Solar Cell Applications	17
2-1. Introduction.....	17
2-2. Experimental.....	18
2-3. Results and Discussions.....	20
2-4. Conclusions.....	23

Chapter 3: Inverted Heterojunction Solar Cells Incorporating Fullerene /	
Polythiophene Composite Core/Shell Nanorod Arrays.....	33
3-1. Introduction.....	33
3-2. Experimental.....	35
3-3. Results and Discussions.....	37
3-4. Conclusions.....	43
Chapter 4: Nanostructured Nanorod Arrays Presenting TiO₂ Nanorods/	
Poly(3-hexylthiophene) for Solar Cells Application.....	60
4-1. Introduction.....	60
4-2. Experimental.....	62
4-3. Results and Discussions.....	65
4-4. Conclusions.....	69
Chapter 5: Synthesis and Characterization of Donor–Acceptor	
Poly(3-hexylthiophene) Copolymers Presenting 1,3,4-Oxadiazole	
Units and Their Application to Photovoltaic Cells.....	79
5-1. Introduction.....	79
5-2. Experimental.....	82
5-3. Results and Discussions.....	90
5-4. Conclusions.....	97
Chapter 6: Conclusions.....	114
References and Notes.....	115

Figure Lists

Chapter 1: Introduction

- Figure 1-1.** General mechanism for photo energy conversion in solar cells.....4
- Figure 1-2.** Elementary steps in the process of photoinduced charge separation for a donor (D) and an acceptor (A): (1) Photoexcitation of the donor; (2) diffusion of the exciton and formation of an encounter pair; (3) electron transfer within the encounter pair to form a geminate pair; (4) charge separation.....4
- Figure 1-3.** Schematic drawing of the donor and acceptor energy levels.....5
- Figure 1-4.** The Characterization of a solar cell device. Current-voltage (I-V) curves of an organic solar cell. The characteristic intersections with the abscissa and ordinate are the open circuit voltage (V_{oc}) and the short circuit current (I_{sc}), respectively. The largest power output (P_{max}) is determined by the point where the product of voltage and current is maximized. Division of P_{max} by the product of I_{sc} and V_{oc} yields the fill factor FF.....7
- Figure 1-5.** The example of organic semiconductors used in polymer solar cells. The structure of P3HT, MDMO-PPV, F8T2, PSiF-DBT, PCDTBT, PBDTTBT, PBDTTT-CF, PCBM, and PCBM derivatives.....10
- Figure 1-6.** 1-6 Schematic diagram of the template-assisted fabrication of cross-linked free-standing nanorod arrays.....13
- Figure 1-7.** Schematic depiction of the regular structure and inverted structure of the polymer solar cell devices.....14

Chapter 2: Ordered Polythiophene/Fullerene Composite Core–Shell Nanorod Arrays for Solar Cell Applications

Figure 2-1. Cartoon representation of the well-ordered nanorod structures.....26

Figure 2-2. (a) SEM image of the P3HT/PCBM (1:1, w/w) nanorod array; the inset displays the ordered Al membrane (scale bar: 100 nm). (b) Top view TEM image of the P3HT/PCBM (1:4, w/w) nanorod structure (scale bar: 50 nm).....26

Figure 2-3. UV spectrums of P3HT/PCBM(1:1, w/w) as-cast film (circle) and nanorods structures (square).....27

Figure 2-4. C-AFM (a) topographic vertical distance: 70 nm (b) current images of a thin film of P3HT/PCBM nanorods and (c) The variation in current between the labeled core (PCBM rich region) and shell (P3HT rich region) regions was 14.3 pA.28

Figure 2-5. *J–V* characteristics of P3HT/PCBM nanorod array devices prepared after annealing at various temperatures, measured under AM 1.5G illumination at an intensity of 100 mW/cm²29

Chapter 3: Inverted Heterojunction Solar Cells Incorporating Fullerene / Polythiophene Composite Core/Shell Nanorod Arrays

Figure 3-1. (a) Schematic representations of the inverted structure and the PCBM/P3HT core/shell structure of the inverted solar cell device. (b) Energy level diagram of the inverted solar cell device. And SEM images of PCBM/P3HT (1:1, w/w) nanorod arrays featuring nanorods having diameters and covered densities (D) on the substrate of (c) 70 nm and 54%, (d) 80 nm and 64%, respectively.....46

Figure 3-2. (a). Reflectance spectra of PCBM/P3HT nanorod array BHJ solar cell devices (conventional structure; nanorod array) and of the electrodes. Device structure: glass/ITO (250 nm)/TiO_x (45 nm)/nanorod array(200nm long, 80nm

diameter) /MoO₃ (20 nm)/Ag (80 nm); sample only with electrodes: a device fabricated without the active layer. Inset: Schematic representation of the incident light path in a completed device and sample only with electrode. (b) Absorption efficiency ($\eta_{A,a}$) of the devices. (c) EQE spectra of the nanorod array inverted devices and the conventional structure inverted devices. (d) Internal quantum efficiency (η_{IQE}) spectra of **PCBM/P3HT** BHJ solar cells (conventional structure; nanorod array with diameter: 80 nm; length: 200 nm).....49

Figure 3-3. (a) the EQEs of 120nm length nanorods with diameter of 65, 70 or 80nm. (b) the EQEs of 80nm diameter nanorods with length of 120, 150 or 300nm. (c) the IQEs of 120nm length nanorods with diameter of 65, 70 or 80nm. (d) the IQEs of 80nm diameter nanorods with length of 120, 150 or 300nm.....52

Figure 3-4. (a) *J–V* characteristics of **PCBM/P3HT** nanorod array devices incorporating 120-nm-length nanorods with diameter of 65, 70 and 80nm. (b) *J–V* characteristics of **PCBM/P3HT** nanorod array devices incorporating 80-nm-diameter nanorods having lengths of 120, 150, and 300 nm. Devices were measured under AM 1.5G illumination at an intensity of 100 mW cm⁻². The thickness of active layer for conventional structure is 120nm.....54

Figure 3-5. Conducting atomic force microscopy (C-AFM) dark *J–V* curves for hole-dominated carrier samples incorporating **PCBM/P3HT** (0.8:1, w/w) in conventional structure and nanorod array structures. Inset: C-AFM current images of **PCBM /P3HT** nanorods.....55

Figure 3-6. *J–V* characteristics of annealed **PCBM/P3HT** nanorod array devices incorporating 80-nm-diameter nanorods having lengths of 120, 150, and 200 nm. Devices were annealed at 120 °C for 10 min and then measured under AM 1.5G illumination at an intensity of 100 mW cm⁻².....56

Chapter 4: Nanostructured Nanorod Arrays Presenting TiO₂

Nanorods/Poly(3-hexylthiophene) for Solar Cells Application

- Figure 4-1.** Schematic representations of the TiO₂/P3HT nanorod core/shell structure of the inverted solar cell device.....72
- Figure 4-2.** (a) High-resolution TEM (HRTEM) image of TiO₂ nanorods. The scale bar is 20nm. (b) X-ray diffraction pattern of TiO₂ nanorods.....73
- Figure 4-3.** The TEM images of cross-section and top view of pure P3HT nanorod array and TiO₂ nanorod/P3HT nanorod array with different weight ratio. (a), (b) for pure P3HT, (c), (d) for TiO₂ nanorod/P3HT: w/w=1/1. The scale bar is 100nm.....74
- Figure 4-4.** (a) Normalized optical absorption spectra of the nanorod arrays with different weight ratio of P3HT/TiO₂ and pure P3HT. (b) PL spectra of nanorod arrays, recorded at an excitation wavelength of 500 nm. The size of the nanorod is 110nm long with 80nm diameter.....75
- Figure 4-5.** C-AFM image (Image size: 0.5 μm × 0.5 μm) of TiO₂ nanorod/P3HT array (a) topographic image. (vertical distance: 100 nm) and (b) current images of a thin film of TiO₂ nanorod/P3HT array; Z-range: 20 pA.....76
- Figure 4-6.** Conducting atomic force microscopy (C-AFM) dark *J–V* curves for hole-dominated carrier samples incorporating TiO₂ nanorod/P3HT arrays.....77
- Figure 4-7.** *J–V* characteristics of TiO₂ nanorod/P3HT array devices. Devices were measured under AM 1.5G illumination at an intensity of 100 mW cm⁻².....78

Chapter 5: Synthesis and Characterization of Donor–Acceptor

Poly(3-hexylthiophene) Copolymers Presenting 1,3,4-Oxadiazole Units and Their Application to Photovoltaic Cells

- Figure 1.** Normalized optical absorption spectra of the self-made P3HT, the copolymers **P05-P20** and comonomer (compound 3) in (a) THF solution (9.6×10^{-5} M) and (b) self-made P3HT and the copolymers **P05-P20** as thin films (the thickness of film is 90nm on quartz.).....101
- Figure 2.** PL spectra of films of the self-made P3HT and the copolymers **P05, P15,** and **P20**, recorded at an excitation wavelength of 450 nm. The thickness of film is 90nm on ITO substrate.....102
- Figure 3.** Cyclic voltammograms of films of the self-made P3HT and the copolymers **P05, P15,** and **P20**, recorded at a scan rate of 50 mV/s.....103
- Figure 4.** Current density–voltage characteristics of illuminated (AM 1.5G, 100 mW cm^{-2}) polymer photovoltaic cells incorporating PCBM blends of the self-made P3HT and the copolymers **P05, P15** and **P20**.....104
- Figure 5.** (a) EQEs of solar cells incorporating copolymer **P15/PCBM** and the self-made P3HT/PCBM blends. (b) Absorption spectra of the copolymer **P15/PCBM** and the self-made P3HT/PCBM at blend ratios of 1:1.....105
- Figure 6.** Topographic AFM images of films of PCBM blends (1:1, w/w) with (a) the self-made P3HT and (b–d) the copolymers (b) **P05**, (c) **P15**, and (d) **P20**. Image size: $2.5 \mu\text{m} \times 2.5 \mu\text{m}$106

Scheme & Table Lists

Chapter 2: Ordered Polythiophene/Fullerene Composite Core–Shell Nanorod Arrays for Solar Cell Applications

Table 2-1. Electronic parameters of vertical p–n junction structure devices prepared from various P3HT/PCBM weight ratios and annealed at various temperatures.....25

Chapter 3: Inverted Heterojunction Solar Cells Incorporating Fullerene / Polythiophene Composite Core/Shell Nanorod Arrays

Table 3-1. External quantum efficiencies (EQEs) and internal quantum efficiencies (IQEs) at 520nm from nanorods of various sizes.....44

Table 3-2. Electronic parameters of vertical p–n junction devices prepared from nanorods of various sizes.....44

Table 3-3. Electronic parameters of annealed vertical p–n junction devices prepared from nanorods of various sizes.....45

Chapter 4: Nanostructured Nanorod Arrays Presenting TiO₂ Nanorods/Poly(3-hexylthiophene) for Solar Cells Application

Table 4-1. Electronic parameters of one dimensional structure array devices prepared from various P3HT/TiO₂ nanorod weight ratios.....71

Chapter 5: Synthesis and Characterization of Donor–Acceptor

Poly(3-hexylthiophene) Copolymers Presenting 1,3,4-Oxadiazole Units and Their Application to Photovoltaic Cells

Table 5-1. Polymerization Data and Thermal Properties of the Copolymers.....98

Table 5-2. Optical and Redox Properties of the Copolymers.....98

Table 5-3. Photovoltaic Properties of Polymer Photovoltaic Cells Incorporating Blends (1:1, w/w) of P3HT/PCBM and P05–P20 /PCBM.....	99
Scheme 5-1. Synthetic Routes Toward M1 and M2	100
Scheme 5-2. Synthetic Route Toward the Copolymers.....	100

Appendix

Chapter 2: Ordered Polythiophene/Fullerene Composite Core–Shell Nanorod

Arrays for Solar Cell Applications

Figure A.2-1. Grazing-incidence XRD diffraction diagrams of P3HT/PCBM(1:1, w/w) as-cast films, identically annealed at 120°C for 10 minutes and P3HT/PCBM nanorods structure. The increase at $2\Theta\sim 5^{\circ}$ (interchain distance of interdigitated alkyl chain in P3HT) and $2\Theta\sim 22^{\circ}$ (interchain distance of face-to-face packing of the thiophene ring) are observed. That means crystallinity is improved.....30

Figure A.2-2. Atomic force microscopy (AFM) topographic images for of a thin film P3HT/PCBM nanorods structure. The image size is $1.48\mu\text{m}\times 1.48\mu\text{m}$, and the vertical scale is 70 nm.....31

Figure A.2-3. Scanning electron microscopy (SEM) images of the **P3HT/PCBM** nanorod nanostructures. The length of rod is 110nm.....32

Chapter 3: Inverted Heterojunction Solar Cells Incorporating Fullerene /

Polythiophene Composite Core/Shell Nanorod Arrays

Figure A3-1. Large-area SEM image of the **PCBM/P3HT** (1:1, w/w) nanorod array; inset: magnified image (scale bar: 100 nm).....57

Figure A3-2. SEM images of **PCBM/P3HT** (1:1, w/w) nanorod arrays having lengths of (a) 200 and (b) 300 nm. Inset to (b): Cartoon representation of the structure in the cross-sectional image.....58

Figure A3-3. (a) Cross-sectional SEM image of ITO glass/ TiO_x ; the thickness of the TiO_x layer was 45 nm. (b) AFM image of glass/ TiO_x surface; the RMS roughness of this film was 1.2 nm.....58

Figure A3-4. (a) and (b) reflectance spectra of **PCBM/P3HT** nanorod array with different diameters (65nm to 80nm) and length (120nm to 300nm) respectively, solar cell devices. (c) and (d) absorption efficiency ($\eta_{A,a}$) of the devices with different diameters and lengths, respectively.....59

Chapter 5: Synthesis and Characterization of Donor–Acceptor

Poly(3-hexylthiophene) Copolymers Presenting 1,3,4-Oxadiazole Units and Their

Figure A5-1. Display the ^1H NMR spectra of self-made P3HT and copolymer **P05-P20**. (a) self-made P3HT, (b) P05, (c) P15, (d) P20.....110

Figure A5-2. shows the dihedral angel between the plane of thiophene and the plane of 1,3,4-oxadiazole moiety simulated from the ChemBio3D Ultra software. The dihedral angel between the polymeric main chain and the 1,3,4-oxadiazole moiety is 32.11°111

Figure A5-3. The Photoluminescence of the comonomer (compound 3) in THF solution (9.6×10^{-5} M) recorded at an excitation wavelength of 310 nm..... 112

Figure A5-4. Synchrotron Grazing-incidence XRD diffraction diagrams of self-made P3HT and copolymer P05-P20 as-cast films (100nm on ITO substrate), identically annealed at 150°C for 10 min. The decrease at $2\theta \sim 5^\circ$ (interchain distance of interdigitated alkyl chain in Polythiophene backbone) is observed obviously for P20. That means ordering of polymer chain is decreased.....113

Chapter 1: Introduction

1-1 Introduction of Polymer Solar cell

Conjugated polymers possessing extended delocalized π electrons are being investigated intensively for their potential uses in such organic optoelectronic devices as light emitting diodes (LEDs), thin film transistors, and photovoltaic cells incorporating bulk heterojunctions (BHJ).¹⁻⁸ In the last fifteen years, a significant progress has been made on the improvement of the power-conversion efficiency (PCE) of polymer BHJ solar cells, and the achieved efficiencies have evolved from less than 1% in the poly(phenylene vinylene) (PPV) system in 1995, to 4–5% in the poly(3-hexylthiophene) (P3HT) system⁹⁻¹², as reported in 2005. The PCE value was further improved to 7%¹³ in recent year. The improvement of PCE resulted from the development of novel conjugated polymer with low band gap, high open-circuit voltage and the well-controllable nanoscale morphology of composite film. Here a brief introduction and overview is given of the field of polymer solar cell.

This dissertation is organized as follow. In the first part, we will give the work principles, critical parameters, the materials, wetting transition of polymers and the nanostructured polymer solar cell. In the second part, we will focus on our recently studies of fabricate and characterize the core-shell nanorod arrays of fullerene/polymer applied for solar cell device. The internal and external quantum

efficiency, hole mobility, and the performance of conjugated polymer/fullerene BHJ solar cells are investigated. In the third part, we will discuss nanostructured arrays of conjugated polymer/inorganic nanocrystals for solar cell application. In the fourth part, a new class of conjugated polymer was synthesized and characterized for solar cell application. Finally, we will finish with some conclusions.

1-2 The Principle of Polymer Solar Cell

1-2-1 Mechanisms leading to the charge generation and collection in organics

Efforts to optimize the performance of organic solar cells should find their basis in the fundamental mechanism of operation. Figure 1-1 illustrates the mechanism by which light energy is converted into electrical energy in the devices. The energy conversion process has four fundamental steps in the commonly accepted mechanism:^[14] (1) Absorption of light and generation of excitons, (2) diffusion of the excitons, (3) dissociation of the excitons with generation of charge, and (4) charge transport and charge collection. Figure 1-1 shows a schematic representation of a typical BHJ solar cell, illustrating the components involved in the mechanistic steps as well as a current–voltage curve defining the primary quantities used to validate the performance of a solar cell.

The elementary steps involved in the pathway from photoexcitation to the

generation of free charges are shown in Figure 1-2.^[15, 16] The processes can also occur in an analogous fashion in the case of an excited acceptor, and the details of these mechanistic steps have been described extensively in the literature.^[17] The key point is that electron transfer is not as simple as depicted in Figure 1-1. The process must be energetically favorable to form the geminate pair in step 3 of Figure 1-2 and an energetic driving force must exist to separate this Coulombically bound electron–hole pair. The open circuit voltage (V_{oc}) is also governed by the energetic relationship between the donor and the acceptor (Figure 1-3) rather than the work functions of the cathode and anode, as would be expected from a simplistic view of these diode devices. Specifically, the energy difference between the HOMO of the donor and the LUMO of the acceptor is found to most closely correlate with the V_{oc} value.^[18, 19] Figure 1-3 shows a schematic drawing of the energy levels in an organic solar cell. The maximum short-circuit current is determined by the smaller optical band gap of the two materials, and V_{oc} is proportional to the difference between the HOMO level of the donor material and the LUMO level of the acceptor compound. For an efficient charge generation in the donor–acceptor blend, a certain offset of the HOMO and LUMO levels (ΔE_{HOMO} , ΔE_{LUMO}) is required,^[20] which is believed to be a few hundred milli-electron Volts. This offset, a minimum energy offset of 0.3 eV between the donor and acceptor, which is often referred to as the exciton binding energy,^[21]

determines the ultimate device efficiency of bulk-heterojunction solar cells.^[22-23]

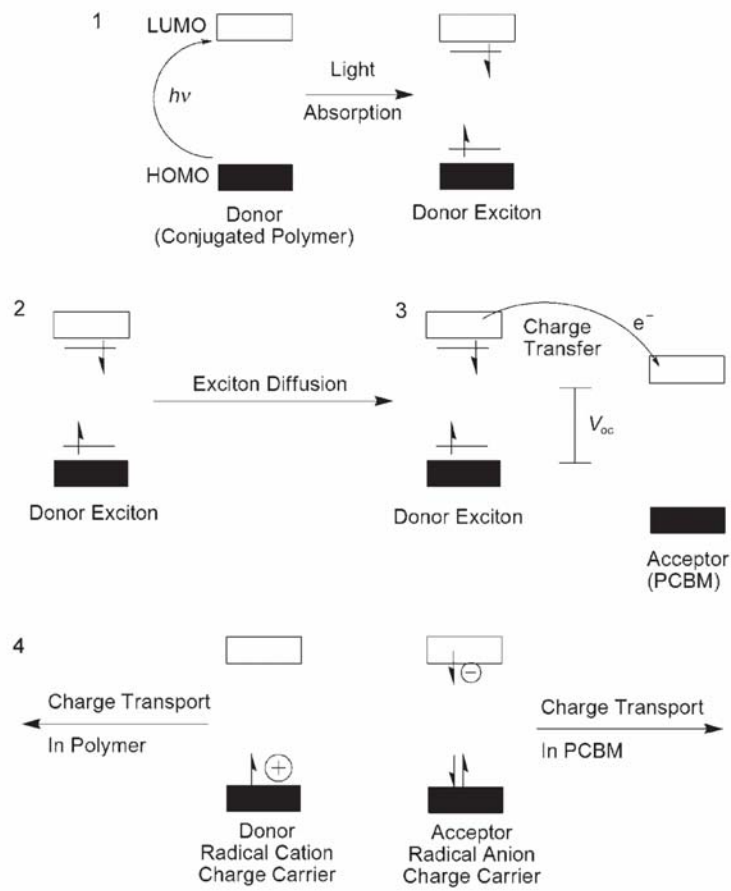


Figure 1-1 General mechanism for photo energy conversion in solar cells.

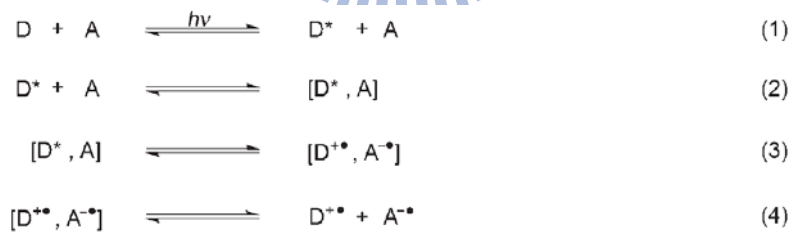


Figure 1-2 Elementary steps in the process of photoinduced charge separation for a donor (D) and an acceptor (A):

- (1) Photoexcitation of the donor;
- (2) diffusion of the exciton and formation of an encounter pair;
- (3) electron transfer within the encounter pair to form a geminate pair;
- (4) charge separation.

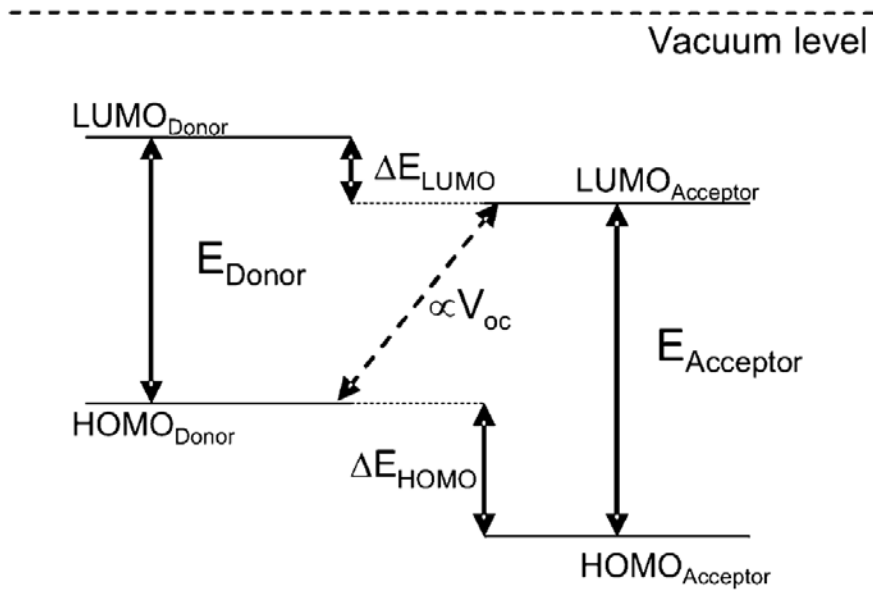
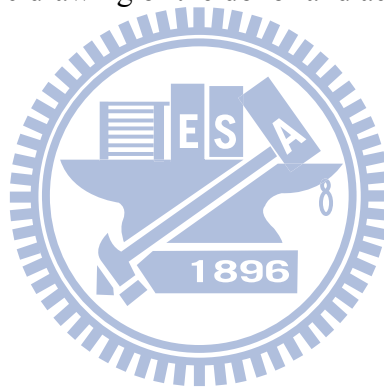


Figure 1-3 Schematic drawing of the donor and acceptor energy levels.



1-2-2 Characterization of a solar cell device

The current-voltage characteristics of a solar cell in the dark and under illumination are shown in Figure 1-4. In the dark, there is almost no current flowing, until the contacts start to inject at forward bias for voltages larger than the open circuit voltage. The device generates power under light. At maximum power point (MPP), the product of current and voltage is the largest.^[24] The photovoltaic power conversion efficiency (η_e) of a solar cell is determined by the following formula:

$$\eta_e = \frac{V_{oc} * I_{sc} * FF}{P_{in}}$$

$$FF = \frac{I_{mpp} * V_{mpp}}{I_{sc} * V_{oc}}$$

where V_{oc} is the open circuit voltage, I_{sc} is the short circuit current, FF is the fill factor, and P_{in} is the incident light power density. This light intensity is standardized at 1000 W/m² with a spectral intensity distribution matching that of the sun on the earth's surface at an incident angle of 48.2°, which is called the AM 1.5 spectrum.^[25] I_{mpp} and V_{mpp} are the current and voltage at the maximum power point.

The external quantum efficiency(EQE) or incident photon to current efficiency

(IPCE) is simply the number of electrons collected under short circuit conditions, divided by the number of incident photons. IPCE is calculated using the following formula:

$$\text{IPCE} = \frac{1240I_{\text{sc}}}{\lambda P_{\text{in}}}$$

where λ [nm] is the incident photon wavelength, I_{sc} [$\mu\text{A}/\text{cm}^2$] is the photocurrent of the device, and P_{in} [W/m^2] is the incident power.

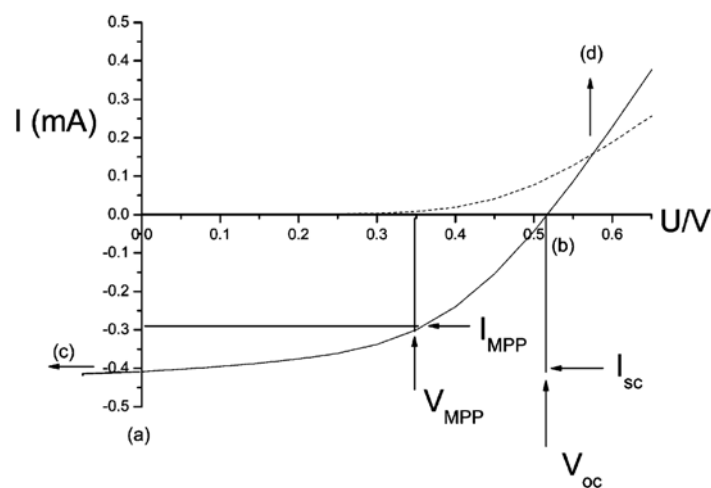


Figure 1-4: The Characterization of a solar cell device. Current-voltage (I-V) curves of an organic solar cell (Dark, - - -; illuminated, -). The characteristic intersections with the abscissa and ordinate are the open circuit voltage (V_{oc}) and the short circuit current (I_{sc}), respectively. The largest power output (P_{max}) is determined by the point where the product of voltage and current is maximized. Division of P_{max} by the product of I_{sc} and V_{oc} yields the fill factor FF.

1-3 Literature Review of Polymer Solar Cell

1-3-1 Materials: Polymers and Inorganic Nanocrystals

Generally, the organic materials having a delocalized π electron system can absorb sunlight, create photogenerated charge carriers, and transport these charge carriers for solar cell application. The conjugated polymers are named as the electron donor polymer in a BHJ solar cell device. Figure 1-5 shows the conjugated polymers which are widely applied to polymer solar cell devices. At present, the polymers poly(3-hexylthiophene) (**P3HT**), poly[2-methoxy-5-(3,7-dimethyloctyloxy)-1,4-phenylenevinylene] (**MDMOPPV**), and poly[2,7-(9,9-dihexylfluorene)-*alt*-bithiophene] (**F8T2**) have been applied to polymer solar cell. However, the narrow absorption spectrum of polymers in 300–650 nm is one of the main hindrances to the further improvement of the efficiencies of conjugated polymer-based solar cell devices. To overcome this problem, some low-band-gap polymer materials as donors have been synthesized successfully and applied to photovoltaic devices.

Recently, the polymers with high open-circuit voltages and consequently high PCEs (above 5 %) have been reported and further investigated for three kinds of polymers, poly[(2,7-silafluorene)-*alt*-(4,7-di-2-thienyl-2,1,3-benzothiadiazole)] (**PSiFDBT**), poly[N-9'-heptadecanyl-2,7-carbazole-*alt*-5,5-(4',7'-di-2-thienyl-benzothiadiazole)] (**PCDTBT**), and poly{4,8-bis(2,5-dioctyl-2-thienyl)-benzo

[1,2-b:4,5-b']dithiophene -alt-[4,7-bis(2-thienyl)-2,1,3-benzothiadiazole)-5,5'-diyl]} (PBDTTBT).^[26-29] Furthermore, the performance of PBDTTT-CF, the derivatives of PBDTTBT, shows PCE value of 7%.^[13, 30, 31] There are number of excellent in-depth reviews covering materials selection for polymer solar cells.^[32-37]

The electron acceptor like Fullerenes derivatives [6,6]-phenyl-C61-butyric acid methyl ester (PCBM), and PC₇₀BM is most commonly used when blended with a light absorbing and hole-conducting conjugated polymer to afford the bulk-heterojunction active layer in a photovoltaic device (shown in Figure 1-5). The [6,6]-phenyl-C61-butyric acid methyl ester (PCBM)-like fullerene derivatives with the different side chain in PCBM are designed and synthesized to investigate the relationship between photovoltaic properties and the molecular structure of fullerene derivative acceptors.^[38,39]

Various hybrid polymer solar cells such as polymer:inorganic-nanoparticle BHJs have been reported, using CdSe nanodots, nanorods,^[40] and tetrapods,^[41,42] and nanoparticles of TiO₂,^[43] ZnO,^[44,45] PbS,^[46,47] PbSe,^[48,49] and CuInSe₂.^[50] In a related approach, nanostructured TiO₂ has been filled with conjugated polymers,^[51-56] but up to now random mixtures of conjugated polymers and inorganic nanoparticles have given the better efficiencies.

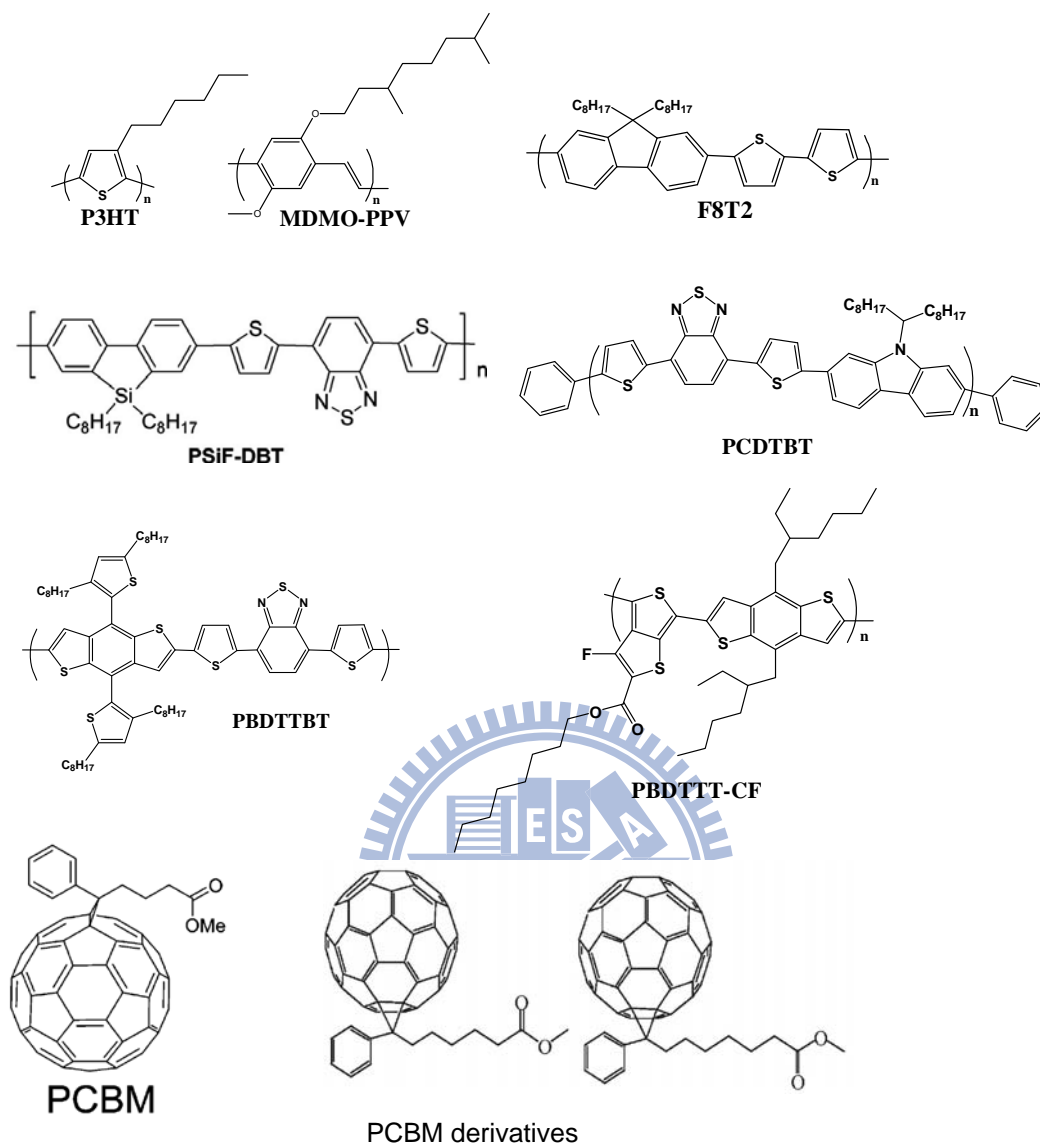


Figure 1-5 The example of organic semiconductors used in polymer solar cells. The structure of P3HT, MDMO-PPV, F8T2, PSiF-DBT, PCDTBT, PBDTTBT, PBDTTT-CF, PCBM, and PCBM derivatives.

1-3-2 the wetting transition in nanopores of conjugated polymer

The wetting of a solid substrate with a liquid has attracted substantial interest because of its various technical applications, including coatings, lubrication, adhesion, painting, and nanoimprinting. Different wetting regimes can be classified according to the spreading coefficient S , which is defined by^[59-61]

$$S = \gamma_{SG} - \gamma_{SL} - \gamma$$

where, γ_{SG} , γ_{SL} , and γ represent the solid-gas, solid-liquid, and liquid-gas interfacial tensions, respectively. S measures the interfacial energy difference between the bare substrate and the substrate covered with a film of liquid. If $S \geq 0$, complete wetting will occur and a liquid droplet will spread spontaneously on the solid substrate until a complete coverage of the substrate with a thin liquid film is achieved. If $S < 0$, a liquid drop deposited on the solid substrate will spread partially. Wetting, in the case of a negative spreading coefficient, is called partial wetting.

The wetting of porous templates with polymer melts and solutions or polymer-containing mixtures is a simple and versatile method for the preparation of tube or rod structures with diameters ranging from a few tens of nanometers to micrometers. Template wetting also makes it possible to modify the nanotubes in a variety of ways, for example through the controlled generation of pores or the embedding of nanoparticles into the rods. This method offers a promising approach to

functionalized nanorods– template hybrid systems and free-standing nanorods. For example, the Poly(9,9-dioctylfluorene) (PFO) polymer nanowires was fabricated by melt-assisted wetting of porous alumina templates.^[57] The single-nanowire imaging, spectroscopy, and nano-optical behavior were investigated for waveguides application.

The template-based preparation of free-standing semiconducting polymeric nanorod arrays on conductive substrates is currently reported. The topography and local conductivity variations on fragile free-standing nanopillar arrays were investigated. The local current-voltage characteristics suggest a space-charge limited conduction in the semiconducting nanopillars. These nanorod arrays are highly interesting for the fabrication of multilayered device architectures to be used in organic photovoltaics.^[58]

The pure P3HT nanorods oriented perpendicularly to indium tin oxide (ITO) glass are fabricated using an anodic aluminum oxide template. Furthermore, the donor/acceptor contact area of polymer solar cells could be increasing for using P3HT nanorods as donor and C₆₀ as acceptor. In a photovoltaic device employing this structure, remarkable photoluminescence quenching (88%) and a seven-fold efficiency increase (relative to a device with a planar bilayer) are achieved.^[59]

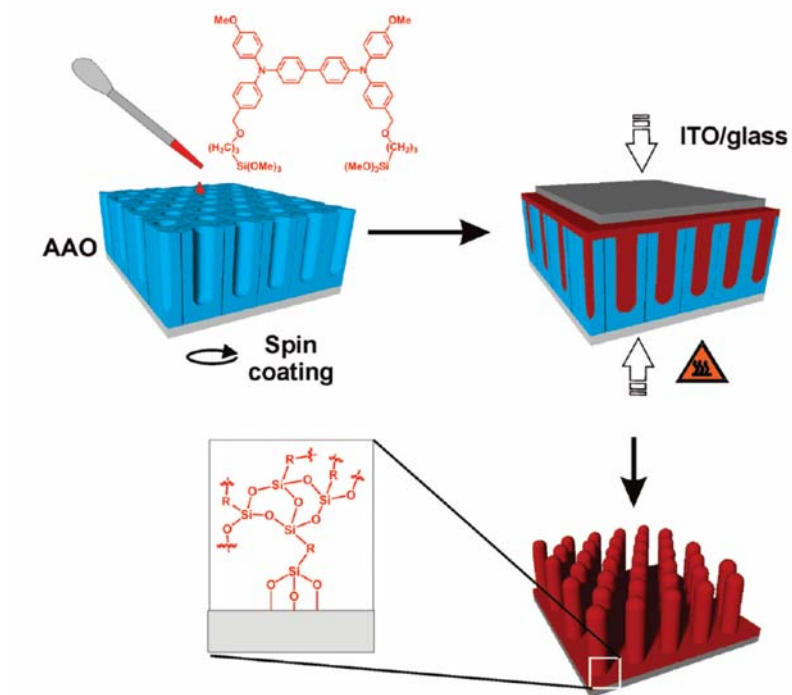
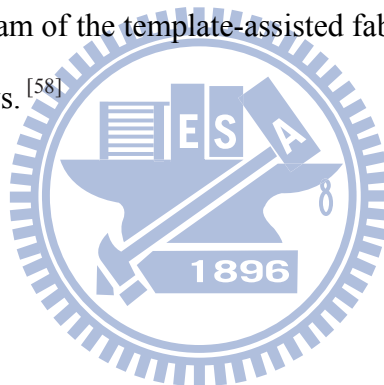


Figure 1-6 Schematic diagram of the template-assisted fabrication of cross-linked free-standing nanorod arrays. [58]



1-3-3 Inverted solar cell

In most regular solar cell devices, the hole-collecting electrode consists of both an acidic PEDOT: PSS layer on high-work-function transparent conducting oxide, and a low work function metal as electron-collecting electrode. In such a device, the oxidation of air-sensitive low-work-function metal cathode such as Al and the degradation of indium tin oxide (ITO/poly (3, 4-ethylene dioxythiophene):

(polystyrene sulfonic acid) (PEDOT:PSS) interface represents an instability that

demands encapsulation techniques to prevent exposure to air [62,63]. The TiO_x and ZnO

(Zinc Oxide) [64-67] as electron collecting electrode and the V_2O_5 (Vanadium (V) oxide)

and MoO_3 [68-70] (Molybdenum (VI) oxide) as hole transport layer are used to replace

Al and PEDOT: PSS for the fabrication of polymer heterojunction solar cell device

with an inverted geometry. Furthermore, this inverted structure has been shown that

high-workfunction metals such as Au and Ag [71,72] can be deposited onto

polymer/metal oxide layers via thermal evaporation to prevent the oxidation of

electrode.

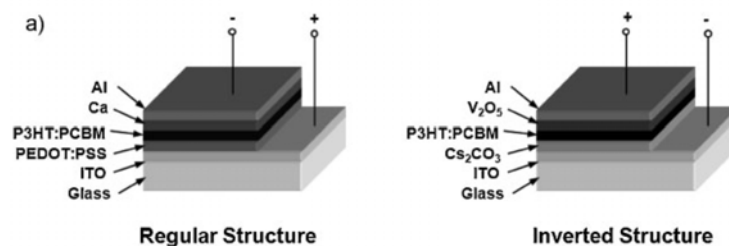


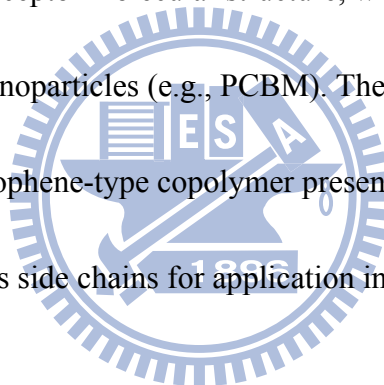
Figure 1-7 Schematic depiction of the regular structure and inverted structure of the polymer solar cell devices.

1-4 Motivation

The morphology of the photoactive layer P3HT/PCBM without post treatment does not have severe suitable phase separation. However, the ordering of donor material (P3HT) and acceptor (PCBM, or inorganic crystals) domain size of phase separation which contribute to the charge transfer and percolation do not develop adequately. In particular, because the ordering and phase separation occur simultaneously with post treatment, it is difficult to control the morphology to achieve the optimum state. Therefore, the fabrication of an ordered bulk heterojunction that can help enhance charge transport and overcome exciton recombination is a promising way to obtain high performance solar cell devices.^[73-75] Such structures offer solar cell performance advantages compared with the planar bilayer, such as efficient charge extraction by the increase of donor-acceptor interfacial area, the decrease of exciton recombination loss, carrier transfer time and reverse electron transfer, and retention of the electron and hole pathways.^[76,77] Therefore, we try to fabricate ordered conjugated polymer/ nanoparticle composite nanorod arrays which contribute efficient transport of electrons and holes along the phase-separated regions in the nanorod array structure, respectively.

For the development of novel materials, the conjugated polymers containing electron donor-acceptor pairs in the polymeric main chain and/or side chains has

become quite attractive recently^{78–85} because such system exhibit tunable electronic properties and enlarged spectral absorption ranges. Alternatively, the introduction of a side-chain electron-acceptor unit—usually a conjugated species that absorbs a wavelength different from that of the conjugated polymer—can increase the breadth of the wavelengths of light absorbed. Furthermore, the photogenerated excitons can be dissociated into electrons and holes more efficiently in these types of conjugated polymer because of the internal field produced by the inherent dipole moment resulting from the donor–acceptor molecular structure, with subsequent charge transfer to nearby n-type nanoparticles (e.g., PCBM). Therefore, we developed a new class of donor–acceptor thiophene-type copolymer presenting electron-withdrawing 1,3,4-oxadiazole moieties as side chains for application in photovoltaic cells.



Chapter 2: Ordered Polythiophene/Fullerene Composite Core–Shell Nanorod Arrays for Solar Cell Applications

2-1 Introduction Materials

The development of conjugated polymers for use in organic optoelectronic devices has advanced dramatically in recent years. In particular, polymer heterojunction solar cell devices are receiving considerable attention.^[1, 5, 86–90] Typically, the active layer of a polymer heterojunction solar cell is prepared from a thin film of an electron-donating conjugated polymer and an electron-accepting species. The power conversion efficiency (PCE) of polymer heterojunction solar cells has improved dramatically over the last few years; those containing blends of regioregular poly(3-hexylthiophene) (**P3HT**) and [6,6]-phenyl-C₆₁-butyric acid methyl ester (**PCBM**), have recently reached PCEs of ca. 4–5% under standard solar conditions (AM 1.5G, 100 mW/cm²).^[91–93]

There is generally no preferred direction for the internal fields of separated charges for a polymer heterojunction solar cell device; that is, the electrons and holes created within the volume have no net resulting direction in which they should move.^[33] Furthermore, because the separated holes and electrons require percolated pathways for transport to their contacts, device structures containing a two-phase donor/acceptor film must exhibit features interspaced with an average length of ca. 10–20 nm, equal to or less than the exciton diffusion length. This structure minimizes

the losses that arise from recombination of charges moving in the wrong direction.

The wetting of porous alumina membrane (AAO) templates with polymer melts, solutions, or polymer-containing mixtures is a simple and versatile method for the fabrication of one-dimensional structures having diameters ranging from a few tens of nanometers to several micrometers. This approach is a promising one for preparing functionalized nanorod–template hybrid systems and free-standing nanotubes and nanorods.^[61, 94–96] Additionally, the hole mobility of a pure **P3HT** nanowire in a straight AAO pore is enhanced by as much as a factor of 20 compared with that in a neat film^[97] because the polymer chains are partially aligned in the charge-transport direction after infiltrating the vertically straight nanopores of the anodic alumina. Therefore, in this present study, we used the wetting of ordered AAO templates to fabricate (figure 2-1) **P3HT/PCBM** core–shell nanorods for use in solar cell devices. We expect that such ordered nanorod structures will provide more-efficient polymer solar cells.

2-2 Experimental

We prepared **P3HT/PCBM** films having a thickness of 120 nm through solution casting onto ITO glass slides and then placed an alumina membrane (AAO) on top of the **P3HT/PCBM** film. This **P3HT/PCBM** film/alumina membrane was sandwiched

between two glass slides and then placed in an oven and annealed under vacuum.

After 6 h, the assembled system was cooled to room temperature. Dissolving the alumina membranes in 10 wt% NaOH solution released the **P3HT/PCBM** core-shell nanorod structures, which were dried under vacuum for 12 h prior to characterization.

Scanning electron microscopy (SEM) images of the resultant **P3HT/PCBM** nanostructures were investigated using a JEOL 6500 model scanning electron microscope at an accelerating voltage of 15 kV. The samples were coated with a thin layer of platinum (thickness: ca. 3 nm) prior to SEM imaging. Transmission electron microscopy (TEM) images were obtained using a Hitachi H-600 transmission electron microscope. The sample for the TEM analysis was prepared by removing the nanorod array thin film from the ITO substrate with 1% HF, and then collecting the thin film with a TEM Grid coated with carbon. We performed conductance atomic force microscopy (C-AFM) experiments using platinum-coated silicon cantilevers [NanoSensors Inc. (PPP-ContPt, spring constant $k = 0.2$ N/m)] and a Digital Nanoscope IV operated under ambient conditions. The current density-voltage ($J-V$) characteristics of the polymers were measured using devices having the structure ITO/PEDOT:PSS/**P3HT:PCBM**/Al. The ITO-coated glass substrate was pre-cleaned and treated with oxygen plasma prior to use. The **P3HT/PCBM** layer was spin-coated from a chlorobenzene solution. Using a base pressure below 1×10^{-6} torr, a layer of

Al (100 nm) was vacuum-deposited as the cathode. Testing of the devices was performed under simulated AM 1.5G irradiation (100 mW/cm^2) using a xenon lamp-based Newport 66902 150W solar simulator equipped with an AM1.5 filter as the white light source; the optical power at the sample was 100 mW/cm^2 , detected using an OPHIR thermopile 71964. The current density–voltage (J – V) characteristics were measured using a Keithley 236 source-measure unit.

2-3 Results and Discussions

Figure 2-2a displays an SEM image of the **P3HT/PCBM** (1:1, w/w) nanorod array structure. The average diameter of the nanorods was ca. 65 nm, equal to the diameter of the nanopores (65 nm) in the ordered AAO membrane (inset to Figure 2-2a). Figure 2-2b provides a TEM top-view image of the **P3HT/PCBM** (1:4, w/w) nanorods, revealing their core–shell-like structures; the dark central region of the nanorods represents the **PCBM**-rich region, which has a higher electron density than that of the **P3HT**-rich region.

Intensity normalized absorption spectrum of **P3HT/PCBM** (1:1, w/w) thin film and nanorods are shown in figure 2-3. The maximum absorption (λ_{max}) took place at ca. 504 nm for the **P3HT/PCBM** thin film, resulting from π – π^* transitions. In comparison, the absorption peak of P3HT/PCBM nanorod array shifted slightly

towards a longer wavelength at 508 nm displayed. The Full-width-at-half -maximum (FWHM) increase to 231nm for P3HT/PCBM nanorod array from 173nm for P3HT/PCBM thin film, an increase of 58nm.

Figure 2-4 displays C-AFM images of the **P3HT/PCBM** (1:1, w/w) nanorods embedded onto the ITO glass substrate. In the topographic image (Figure 4a), the light regions having a height of ca. 70 nm represent the **P3HT/PCBM** nanorods. In the current image (Figure 4b), measured at a sample bias of -1 V, the currents of the **P3HT/PCBM** nanorods (light regions) were ca. 30 pA, whereas those of the spaces between the rods (dark regions) were at the level of the noise (ca. 0.5 pA); this image also reveals the contrast between the current images of the core and shell regions. The current resulted mainly from hole transport because Pt and ITO have high work functions of ca. 5.7 and 4.8 eV, respectively. Because the Pt-coated tip was biased, the influence of the surface electrical properties of ITO played only a minor role^[98]. We observed a variation in current of 14.3 pA between the charge transport of the core and shell regions of the nanorods, despite have some inhomogeneities in their compositions. This phenomenon resulted primarily from the composition difference between the core and shell region, where the dark central region of the nanorods represent the PCBM-rich region and the light region of the nanorods represent the P3HT-rich region. The nanorods of the **P3HT/PCBM** blend possessed core-shell

structures, with the **P3HT**-rich regions of the shell evident in the C-AFM current image. Therefore, we expected most of the electron/hole pairs to separate at the p–n interface, such that the electron and hole transport would occur through the **PCBM**-rich region (n-type) and **P3HT**-rich region (p-type) individually and efficiently in this core–shell structure.

The phase separation of P3HT/PCBM blends in the wetting of porous AAO membrane is determined by the flow induced shear stress, which is the largest along the AAO pore wall and is the lowest in the center of AAO pore. Since the viscosity of PCBM is much larger than that of P3HT at 120°C, the largest stress along the AAO pore wall will induce lower viscosity part of the blend, i.e. P3HT rich region to flow along. Whereas, the minimum stress in the center of AAO pore will have higher viscosity part of the blend, PCBM rich region, to flow along. Consequently, this phase separation of the P3HT/PCBM blend during flow results in the core-shell structured nanorods after quenching to room temperature.

Figure 2-5 displays the J – V characteristics of solar cell devices incorporating ordered nanorods of various compositions. The performance increased upon decreasing the **PCBM** content (Table 2-1). For the device containing **P3HT** and **PCBM** at a 1:2 ratio (w/w), the values of the short circuit current density (J_{sc}), the fill factor (FF), and the PCE were 4.4 mA/cm², 38%, and 0.66%, respectively; these values increased to 5.9

mA/cm^2 , 53%, and 1.30%, respectively, for the 1:0.6 (w/w) **P3HT/PCBM** device.

This improvement in efficiency might be caused by more efficient charge transport in the device structure, due to the high difference in their composition of core and shell.

To improve the performance of our solar cell devices, we subjected them to annealing at various temperatures. For the device incorporating **P3HT/PCBM** at a 1:0.6 ratio

(w/w), the values of PCE and J_{sc} improved to 2.0% (from 1.3%) and $8.7 \text{ mA}/\text{cm}^2$

(from $5.9 \text{ mA}/\text{cm}^2$), respectively, after thermal annealing at $120 \text{ }^\circ\text{C}$ for 10 min. This

improved performance after annealing quite possibly resulted from increases in the

degree of crystallization,^[10] the transport properties,^[99] and the light absorption^[100]

of the P3HT-rich region and also from the improved contact at the electrode for the

transfer of electrons. The area covered by the nanorods on the substrate determines

the amount of incident light absorbed. In our devices, this area was ca. 43% (defined

by the AAO membrane) of the total substrate surface. Hence, increasing the packing

density of the nanorods so that they occupy a greater percentage of the surface area

might improve the devices' performance further so that they would have potential for

use in solar cell applications.

2-4 Conclusions

In summary, we have used the melt-assisted wetting of porous alumina templates

to fabricate vertical nanorod arrays of P3HT and PCBM having core-shell nanostructures for application in polymer solar cells. C-AFM current images revealed the difference of charge transport behavior of the core and shell moieties.



TABLE 2-1. Electronic parameters of vertical p–n junction structure devices prepared from various P3HT/PCBM weight ratios and annealed at various temperatures.

P3HT/PCBM ratio	J_{sc}^a (mA/cm ²)	V_{oc}^b (V)	FF ^c (%)	η^d (%)	Annealing Temperature ^e (°C)
1:0.6	5.9	0.41	53	1.30	–
1:1	5.8	0.42	35	0.85	–
1:2	4.4	0.40	38	0.66	–
1:0.6	7.2	0.45	45	1.43	100
1:0.6	8.7	0.46	50	2.00	120

^aShort-circuit current density.

^bOpen circuit voltage.

^cFill factor.

^dPower conversion efficiency.

^eAnnealing time: 10 min.



Figure

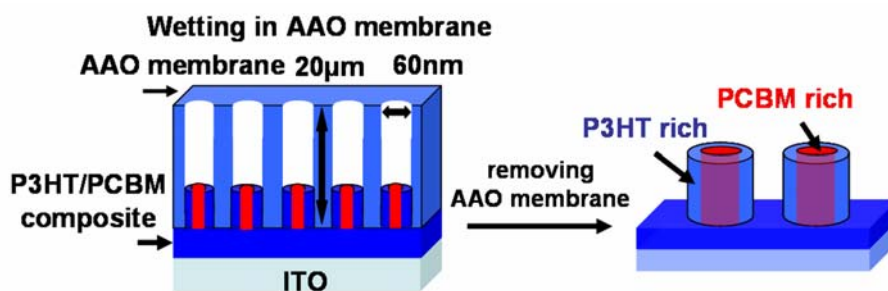


Figure 2-1 Cartoon representation of the well-ordered nanorod structures.

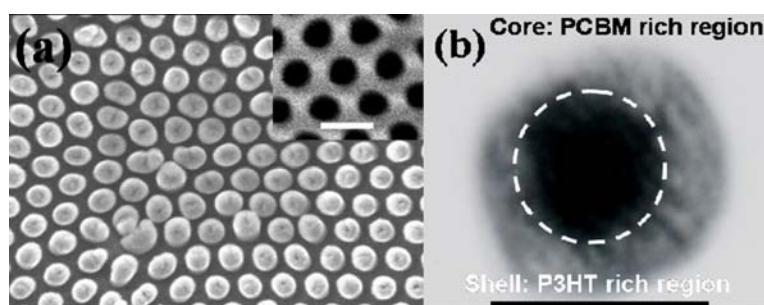


Figure 2-2 (a) SEM image of the P3HT/PCBM (1:1, w/w) nanorod array; the inset displays the ordered Al membrane (scale bar: 100 nm). (b) Top view TEM image of the P3HT/PCBM (1:4, w/w) nanorod structure (scale bar: 50 nm).

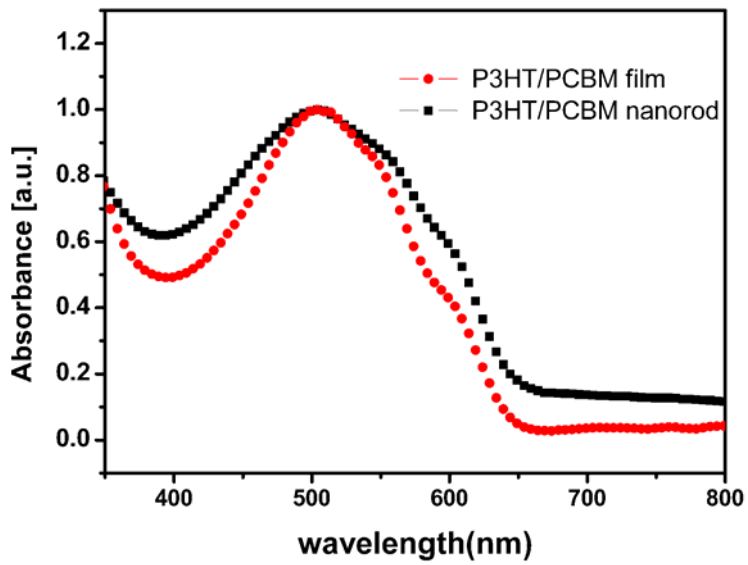
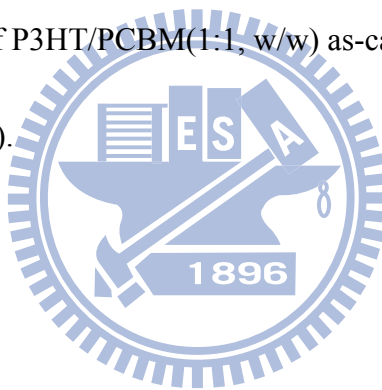


Figure 2-3 UV spectrums of P3HT/PCBM(1:1, w/w) as-cast film (circle) and nanorods structures (square).



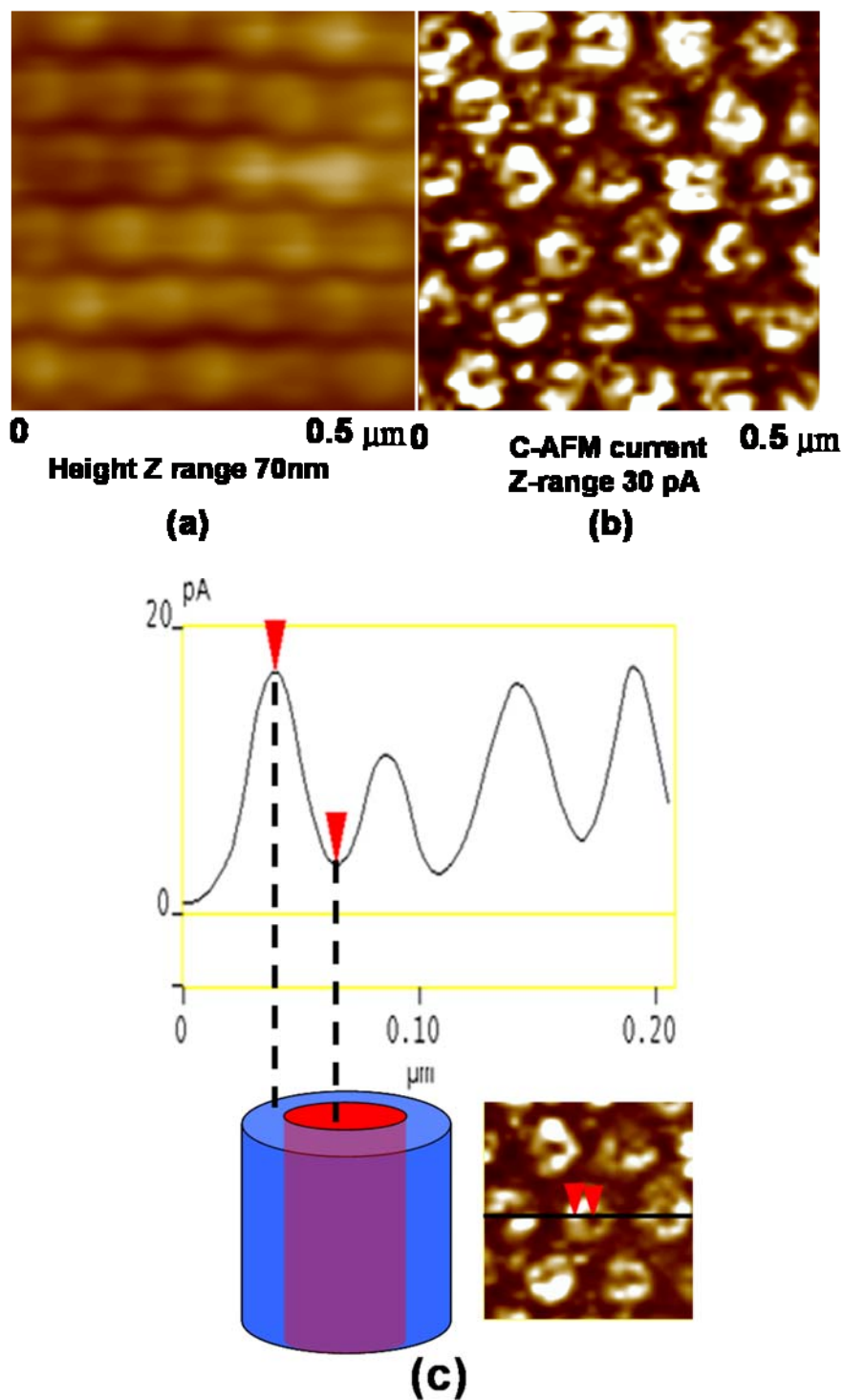


Figure 2-4 C-AFM (a) topographic vertical distance: 70 nm (b) current images of a thin film of P3HT/PCBM nanorods and (c) The variation in current between the labeled core (PCBM rich region) and shell (P3HT rich region) regions was 14.3 pA

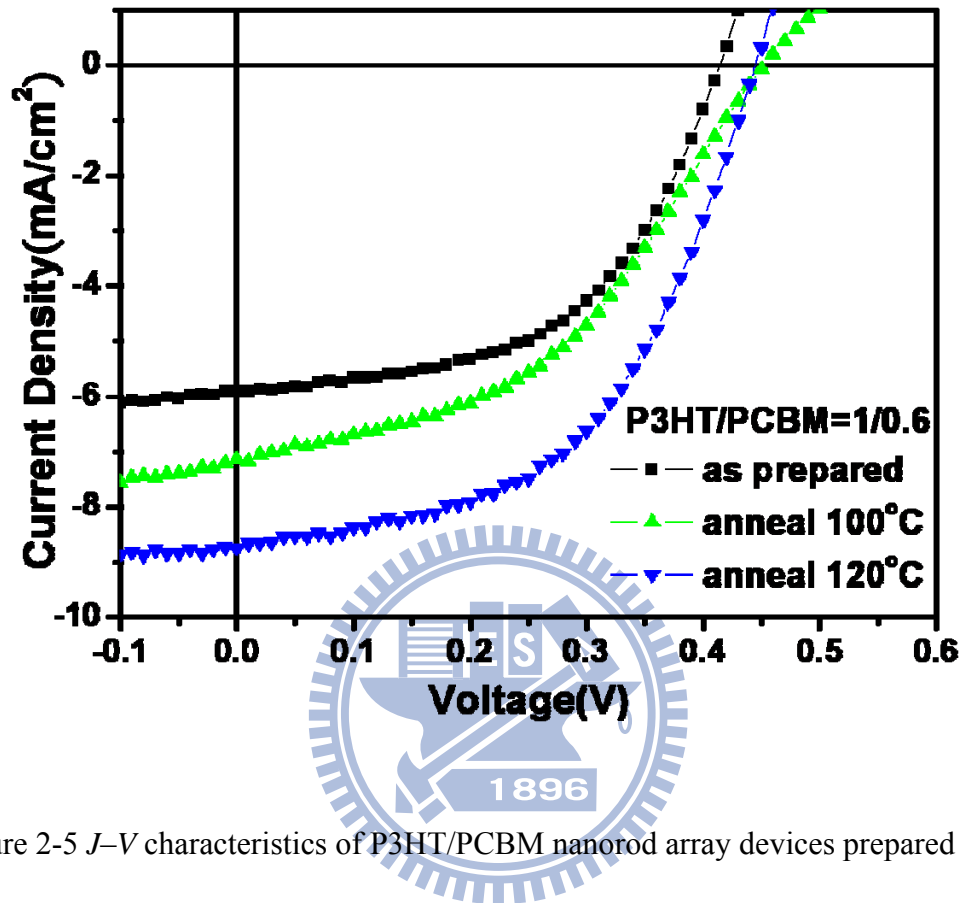
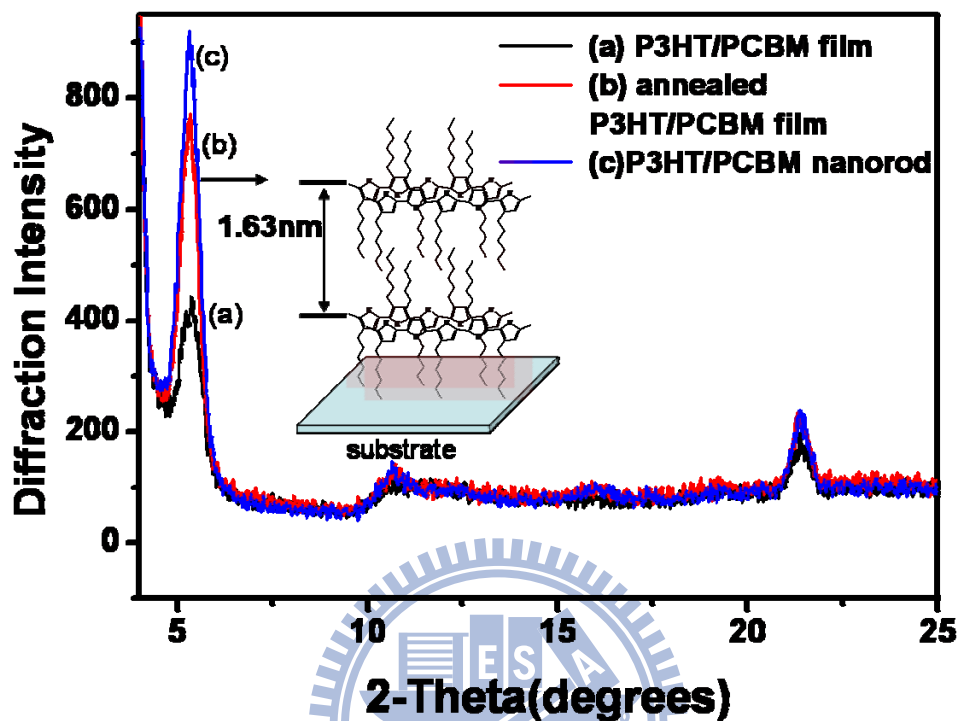


Figure 2-5 J - V characteristics of P3HT/PCBM nanorod array devices prepared after annealing at various temperatures, measured under AM 1.5G illumination at an intensity of 100 mW/cm^2 .

Appendices



FigureA.2-1 Grazing-incidence XRD diffraction diagrams of P3HT/PCBM(1:1, w/w) as-cast films, identically annealed at 120°C for 10 minutes and P3HT/PCBM nanorods structure. The increase at $2\Theta\sim 5^{\circ}$ (interchain distance of interdigitated alkyl chain in P3HT) and $2\Theta\sim 22^{\circ}$ (interchain distance of face-to-face packing of the thiophene ring) are observed. That means crystallinity is improved.

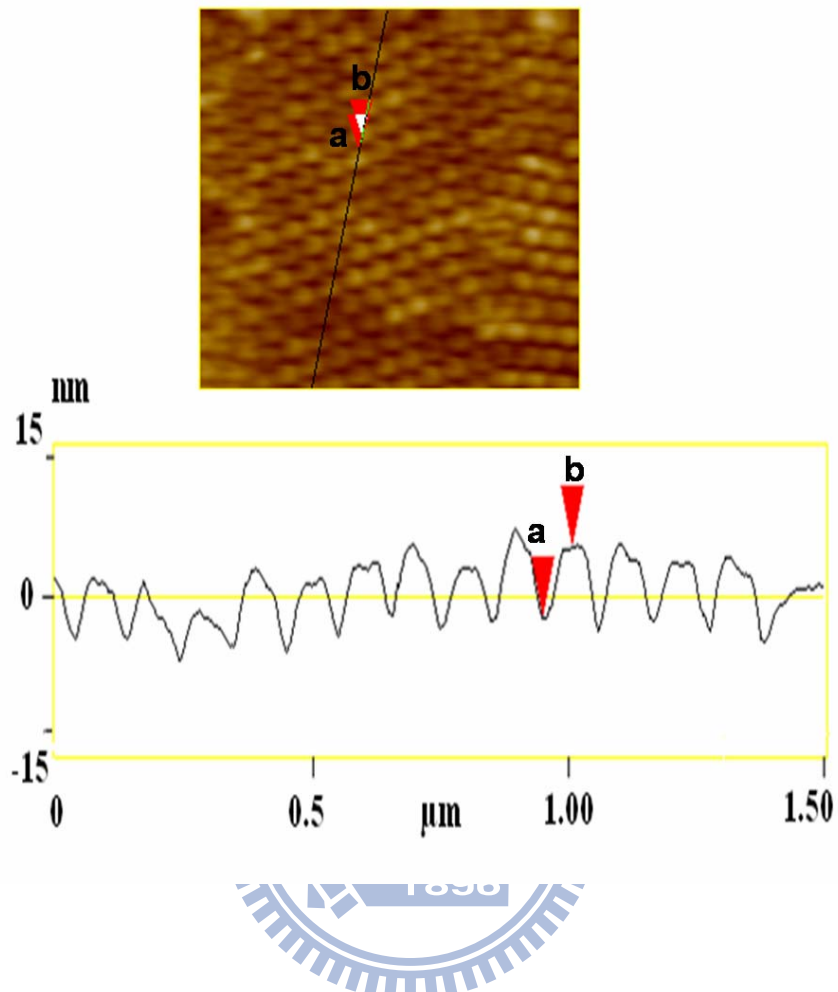


Figure A.2-2 Atomic force microscopy (AFM) topographic images for of a thin film P3HT/PCBM nanorods structure. The image size is $1.48\mu\text{m} \times 1.48\mu\text{m}$, and the vertical scale is 70 nm.

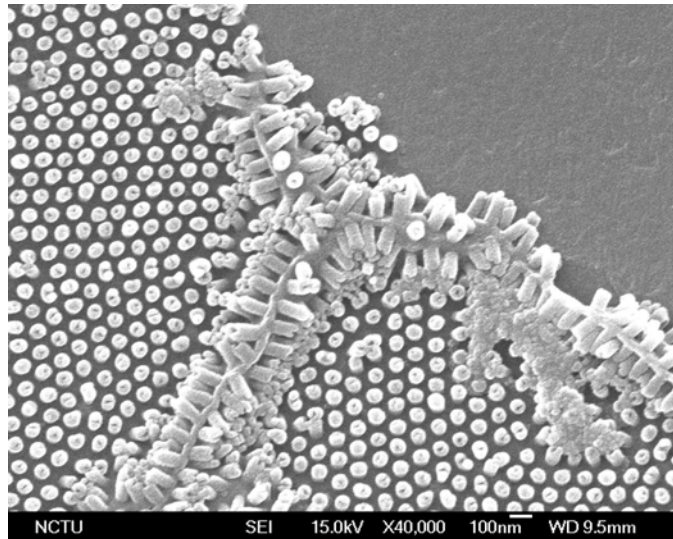
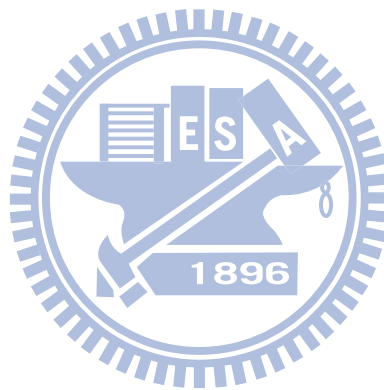


Figure A.2-3 Scanning electron microscopy (SEM) images of the **P3HT/PCBM** nanorod nanostructures. The length of rod is 110nm.



Chapter 3:

Inverted Heterojunction Solar Cells Incorporating Fullerene / Polythiophene Composite Core/Shell Nanorod Arrays

3-1 Introduction Materials

The development of conjugated polymers for use in organic optoelectronic devices is an active field of research. In particular, polymer heterojunction solar cells have attracted much attention because of their potential application in large-area, flexible, low-cost devices.^[1-7, 86] The power conversion efficiencies (PCEs) of bulk heterojunction (BHJ) solar cells have improved dramatically over the last few years. For example, the PCEs of BHJ solar cells incorporating regioregular poly(3-hexylthiophene) (**P3HT**) as the donor and [6,6]-phenyl-C₆₁-butyric acid methyl ester (**PCBM**) as the acceptor have recently reached values of ca. 4–5% under standard solar conditions (AM 1.5G, 100 mW/cm²).^[8-12, 92] Nevertheless, the PCEs of these polymer BHJ devices must improve further if they are to be employed practically, necessitating the development of unconventional structures. Alternating donor and acceptor phases possessing vertically aligned geometries, such as alternating nanorods, appear to be ideal structures for independent carrier transport.^[101,102] These structures are, however, difficult to obtain because of the complexity of the fabrication tools available. For the production of ordered polymeric nanorod arrays, template-based approaches are probably most suitable.

Inverted BHJ devices incorporating metal oxides^[64-69, 103] such as TiO_x and MoO₃ as electrodes and high-work-function anodes (e.g., Ag and Au) have been developed recently because of avoiding the problems of oxidation,^[62,63] which occurs in low-work-function cathodes, and degradation of the indium tin oxide (ITO)–poly(ethylenedioxythiophene) (PEDOT) interface, which occurs frequently in conventional solar cell structures. In this study, we use core/shell-structured **PCBM/P3HT** nanorod arrays as the active layer, which we fabricated using an anodic aluminum oxide (AAO) membrane, to construct an inverted solar cell. To the best of our knowledge, this is the first report of **PCBM/P3HT** nanorod arrays being incorporated into inverted BHJ solar cells. Our approach has several advantageous features (Figure 3-1): (i) the energy level of the highest occupied molecular orbital (HOMO) of the shell (**P3HT**-rich region) can match that of the metal oxide electrode deposited for hole transport on the shell; (ii) the energy level of the lowest unoccupied molecular orbital (LUMO) of the core (**PCBM** rich region) can also match that of the other metal oxide layer for the transport of electrons; and (iii) the direct transport of holes and electrons along the phase-separated shell and core, respectively, occurs in the nanorods. Hence, we expected that such core/shell nanorod array devices featuring a high covered density of nanorods on the substrate and an inverted device geometry would provide more-efficient devices.

3-2 Experimental Section

Regioregular **P3HT** (4002-E, Rieke Metals), **PCBM** (Nano-C, Inc.), and poly(3,4-ethylenedioxythiophene: polystyrenesulfonate) (PEDOT: PSS) (Baytron P VP Al 4083, Inc.) were obtained commercially.

A solution of titanium isopropoxide (Alfa, 99.995%; 10 wt%) in isopropyl alcohol was spin-coated onto pre-cleaned ITO glass substrates under a N₂ ambient and then it was converted to 40-nm-thick TiO_x via hydrolysis at room temperature in air for 2 h.

The substrate was then heated at 450 °C for 30 min to complete the hydrolysis reaction.

PCBM/P3HT films of various thicknesses were prepared through solution casting onto ITO/TiO_x substrates; an AAO membrane was then placed on top of the **PCBM/P3HT** films. This **PCBM/P3HT** film/AAO membrane was sandwiched between two glass slides and then placed in an oven and annealed at 120 °C under vacuum. After 6 h, the assembled system was cooled to room temperature. Dissolving the alumina membranes in 10 wt% NaOH solution released the **PCBM/P3HT** core/shell nanorod structures, which were dried under vacuum for 12 h prior to characterization. SEM images of the resultant **PCBM/P3HT** nanostructures were recorded using a JEOL 6500 scanning electron microscope operated at an accelerating voltage of 15 kV. The samples were coated with a thin (ca. 3 nm) layer of Pt prior to

SEM imaging.

The current density–voltage (J – V) characteristics of the polymers were measured using devices having the structure ITO/TiO_x/ **PCBM:P3HT** /MoO₃/Ag. The ITO-coated glass substrate was pre-cleaned and treated with oxygen plasma prior to use. The TiO_x layer was prepared using the spin-coating process described above. The **PCBM/P3HT** layer was spin-coated from a chlorobenzene solution. Using a base pressure of less than 1×10^{-6} torr, layers of MoO₃ (20 nm) and Ag (80 nm) were vacuum-deposited to form the anode.

The devices were tested under simulated AM 1.5G irradiation (100 mW cm^{-2}) using a Xe lamp–based Newport 66902 150W solar simulator equipped with an AM1.5 filter as the white light source; the optical power at the sample was 100 mW cm^{-2} , detected using an OPHIR thermopile 71964. The J – V characteristics were measured using a Keithley 236 source-measure unit. The EQEs were measured using a Keithley 236 source-measure unit coupled with an Oriel Cornerstone 130 monochromator. The light intensity at each wavelength was calibrated using an OPHIR 71580 diode.

The Hole-only sample, used to investigate hole transport in the polymer/PCBM layers, were fabricated with the structure of ITO/PEDOT/nano rod array. The J – V curves was measured using a conductive atomic force microscopy (C-AFM)

experiments using platinum-coated silicon cantilevers [NanoSensors Inc. (PPP-ContPt, spring constant $k = 0.2$ N/m), tip diameter ~ 20 nm] and a Digital Nanoscope IV operated under ambient conditions. For J - V measurement of C-AFM, we determined the contact area between tip and sample assuming a 20nm diameter circle. The J - V curves from each sample were averaged from four different regions.

3-3 Results and Discussion

Figures 3-1a and 3-1b provide a schematic representation of the **PCBM/P3HT** core/shell nanorod arrays in an inverted solar cell structure and an energy level diagram for each material, respectively. In this nanorod-based inverted architecture, we positioned a TiO_x layer between the ITO glass and the active layer because it is an appropriate material for the electron-collecting ITO/ TiO_x bottom electrode. The energy level of the LUMO of TiO_x is -4.4 eV, which suggests that electrons (LUMO of PCBM: -4.3 eV) can be injected into the TiO_x interlayer, while the holes from the active layer blend levels can be effectively blocked (HOMO of TiO_x : -7.5 eV). The thickness of the TiO_x thin film was 45 nm; its root-mean-square (RMS) roughness, determined through atomic force microscopic analysis, was 1.2 nm (see Appendix: Figure A3-3). In this study, the configuration of the device, stacked from bottom to top, was ITO/ TiO_x / **PCBM:P3HT** (0.8:1, w/w) nanorod arrays/ MoO_3 /Ag. Here, the

hole transport layer (MoO_3) was deposited on the shell (p-type rich region) of the nanorods as a hole-selecting layer.

Figure 3-1c and 3-1d display scanning electron microscopy (SEM) images of the **PCBM/P3HT** (1:1, w/w) nanorod array structure with 54% and 64% covered density determined by pore size of AAO template 70nm and 80nm on the substrate. The average diameter of the nanorods was equal to the diameter of the nanopores in the ordered AAO template, revealing our good control over the nanorod diameter. We used melt-assisted wetting of ordered AAO templates to fabricate the **PCBM/P3HT** core/shell nanorods (core: **PCBM**-rich region; shell: **P3HT**-rich region) structure. The phase separation of the **PCBM/P3HT** blends during the wetting of porous AAO membrane was determined by the flow-induced shear stress, and its mechanism was described in a previous report¹⁶.

Figure 3-2a displays the reflectance spectra of the **PCBM/P3HT** nanorod array solar cell device and of the device formed without the active layer. The actual amount of the light absorbed in each device (A) can be estimated by deducting the reflectance in the device (R) from the intensity of incident light ($A = 1 - R$), because the metal electrodes (MoO_3/Ag) of the devices did not allow any transmission of incident light. The absorption efficiency in the active layer $\eta_{A,a}$ was determined^[104] from the light absorbed in the photoactive layer (A_a) and reflectances of the device (R_d) and the

electrodes (R_e):

$$\eta_{A,a} = 1 - \frac{R_d}{R_e} \quad (1)$$

For the control experiment, we employed a conventional BHJ device having an active layer thickness that was the same as the length of the nanorods. The nanorod arrays having a diameter of 80 nm and a length of 200 nm exhibited a reflection intensity that was lower than that of the conventional device.

Figure 3-2b displays the absorption efficiencies of the devices. Even though it featured a smaller absorption area, associated with the gaps between the nanorods, our nanorod array-based device exhibited superior absorption efficiency relative to that of the conventional BHJ structure.

Figure 3-2c presents the external quantum efficiencies (EQEs) of **PCBM/P3HT** nanorod array devices. The nanorod array device structure provided higher EQEs in the region from 420 to 600 nm than did the conventional device; e.g., at 520 nm, they were 57% and 37%, respectively. Therefore, we expected most of the electron/hole pairs to separate efficiently at the p-n interface, such that electron and hole transport would occur through the **PCBM**-rich (n-type) and **P3HT**-rich (p-type) regions, respectively.

Figure 3-2d displays the internal quantum efficiency (IQE) spectra of the devices; the values of η_{IQE} were obtained using the equation

$$\eta_{IQE} = \frac{\eta_{EQE}}{\eta_{A,a}} \quad (2)$$

The device featuring the nanorod arrays exhibited enhanced IQEs at wavelengths in the region 440–620 nm, due to their more efficient charge carrier transport, relative to those of the conventional inverted device; e.g., the IQEs at 520 nm were 66 and 43%, respectively.

Figure 3-3 reveals the EQEs and IQEs of devices with different nanorod dimensions without annealing. Figure 3-3a shows that at 520nm wavelength the EQE increased to 48% for 80nm diameter nanorods from 40% for 65nm diameter nanorods at a fixed nanorod length of 120nm. Figure 3-3b shows the EQE value increased to 53% for 300nm length nanorods from 48% for 120nm length nanorods at a fixed diameter of 80nm. Whereas, Figure 3-3c shows that at 520nm wavelength the IQE increased to 59% for 80nm diameter nanorods from 49% for 65nm diameter nanorods at a fixed nanorod length of 120nm. Figure 3-3d shows the IQE increased to 62% for 300nm length nanorods from 59% for 120nm length nanorods at a fixed nanorod diameter of 80nm. Table 1 summarizes the EQEs and IQEs of the devices with various nanorod dimensions. The increase in IQEs of these nanorod devices can be reasonably assumed by the fact that their rod structure facilitates the charge transport as opposed to the case in the conventional device structure. This requires further

investigation of their transport properties. We used conductive atomic force microscopy rather than using a sandwiched device structure because the active layer are not planar; depositing a thin layer of electrode would cause uneven conducting path.

Figure 3-4 displays the $J-V$ characteristics of solar cell devices incorporating different nanorod dimensions without annealing. Figure 3-4a shows that the short current densities (J_{sc}) and power conversion efficient (PCE) increased to 7.5 mA cm^{-2} and 2.5%, respectively, for 80nm diameter nanorods from 6.1 mA cm^{-2} and 2.2% for 65nm diameter nanorods at a fixed nanorod length of 120nm. Figure 3-4b shows the J_{sc} and PCE increased to 9.6 mA cm^{-2} and 3.2%, respectively for 300nm length nanorods from 7.5 mA cm^{-2} and 2.5% for 120nm length nanorods at a fixed diameter of 80nm. This shows that the devices with longer and larger nanorod result in higher power conversion efficiency. Table 2 summarizes the performance factors of the devices with different nanorod dimensions without annealing.

Figure 3-5 presents the dark $J-V$ curves by hole-dominated conductive atomic force microscopy measurement. We determined the hole mobilities by fitting the dark $J-V$ curves into the space charge-limited current (SCLC) model using the equation

$$J = 9\varepsilon_0\varepsilon_r\mu_h V^2/8L^3 \quad (3)$$

where ε_0 is the permittivity of free space, ε_r is the dielectric constant of the polymer, μ_h is the hole mobility, V is the voltage drop across the device, and L is the polymer thickness.^[105,106] The **PCBM/P3HT** (0.8:1, w/w) nanorod array structure exhibited a hole mobility ($5.98 \times 10^{-4} \text{ cm}^2 \text{ V}^{-1} \text{ s}^{-1}$) that was relative greater than that ($4.73 \times 10^{-5} \text{ cm}^2 \text{ V}^{-1} \text{ s}^{-1}$) of the conventional BHJ structure. The device featuring the 80-nm-diameter, 200-nm-long core/shell nanorod arrays exhibited a higher mobility of $5.98 \times 10^{-4} \text{ cm}^2 \text{ V}^{-1} \text{ s}^{-1}$ along the out-of-plane direction, indicating that the **P3HT**-rich shell on these nanorods facilitated hole transport, even though a small amount of **PCBM** was quite possibly present in the **P3HT**-rich shell. We believe that the increase in hole mobility was due to the phase separation in the core/shell nanorod structure and the increased crystallinity^[16] of **P3HT** in the **P3HT**-rich shells, caused by the much lower **PCBM** concentration than that found in the active **P3HT/PCBM** layers in conventional BHJ devices.

Further improvement on the PCE of the devices with nanorod structures can be carried out by annealing. Figure 3-6 displays the J - V characteristics of solar cell devices incorporating the annealed **PCBM/P3HT** nanorod arrays. The short current densities (J_{sc}) and the PCEs both increased after annealed at 120°C for 10 min; e.g.,

the annealed device increased to 10.7 mA cm^{-2} and 3.6%, respectively, from 9.4 mA cm^{-2} and 3.3%, for the pristine device with the 200-nm nanorod. Table 3 summarizes the performance factors of the various devices. We suspect that the improved performance after annealing resulted from improved contact at the electrodes, allowing more-efficient transfer of holes and electrons, and also from increases in the degree of polymer crystallization^[11] and the transport efficiency of the **P3HT**-rich region.

3-4 Conclusions

In conclusion, we have fabricated inverted BHJ solar cell devices incorporating **PCBM/P3HT** core/shell nanorod arrays. As a result of superior carrier transport, the internal and external quantum efficiencies of these core/shell nanorod inverted solar cells were both higher than those of the corresponding conventional inverted BHJ device. The optimized nanorod array structure had a high hole mobility that was over one order magnitude greater than that of the conventional BHJ structure, as determined by fitting the dark $J-V$ curves into the space charge-limited current model; the corresponding device displayed more efficient carrier transport, which contributed to a higher short-circuit current density and PCE, relative to those of the conventional device.

Table 3-1. external quantum efficiencies (EQEs) and internal quantum efficiencies (IQEs) at 520nm from nanorods of various sizes.

Pore size (nm)	Length (nm)	EQE (%)	IQE (%)
conventional	--	39	47
65	120	40	49
70	120	42	51
80	120	48	59
80	150	51	56
80	200	57	66
80	300	53	62

Table 3-2. Electronic parameters of vertical p–n junction devices prepared from nanorods of various sizes.

Pore size	Length (nm)	J_{sc}^a (mA cm ⁻²)	V_{oc}^b (V)	FF ^c (%)	η^d (%)
conventional	--	5.33	0.63	56.6	1.90
65	120	6.05	0.61	59.1	2.18
70	120	6.82	0.62	57.2	2.43
80	120	7.48	0.62	53.9	2.50
80	150	8.54	0.60	55.1	2.82
80	200	9.44	0.59	58.4	3.25
80	300	9.61	0.60	55.5	3.20

^aShort-circuit current density.

^bOpen circuit voltage.

^cFill factor.

^dPower conversion efficiency.

Active layer: **PCBM/P3HT** (0.8:1, w/w)

TABLE 3-3. Electronic parameters of vertical p–n junction devices prepared from nanorods of various sizes.

Pore size	Length (nm)	J_{sc}^a (mA cm ⁻²)	V_{oc}^b (V)	FF ^c (%)	η^d (%)	Annealing temperature ^e (°C)
80	120	7.48	0.62	53.9	2.50	–
80	120	8.43	0.59	57.1	2.83	120
80	150	9.21	0.59	56.8	3.08	120
80	200	10.70	0.59	56.8	3.60	120

^aShort-circuit current density.

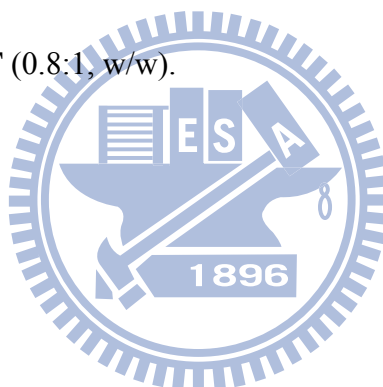
^bOpen circuit voltage.

^cFill factor.

^dPower conversion efficiency.

^eAnnealing time: 10 min.

Active layer: **PCBM/P3HT** (0.8:1, w/w).



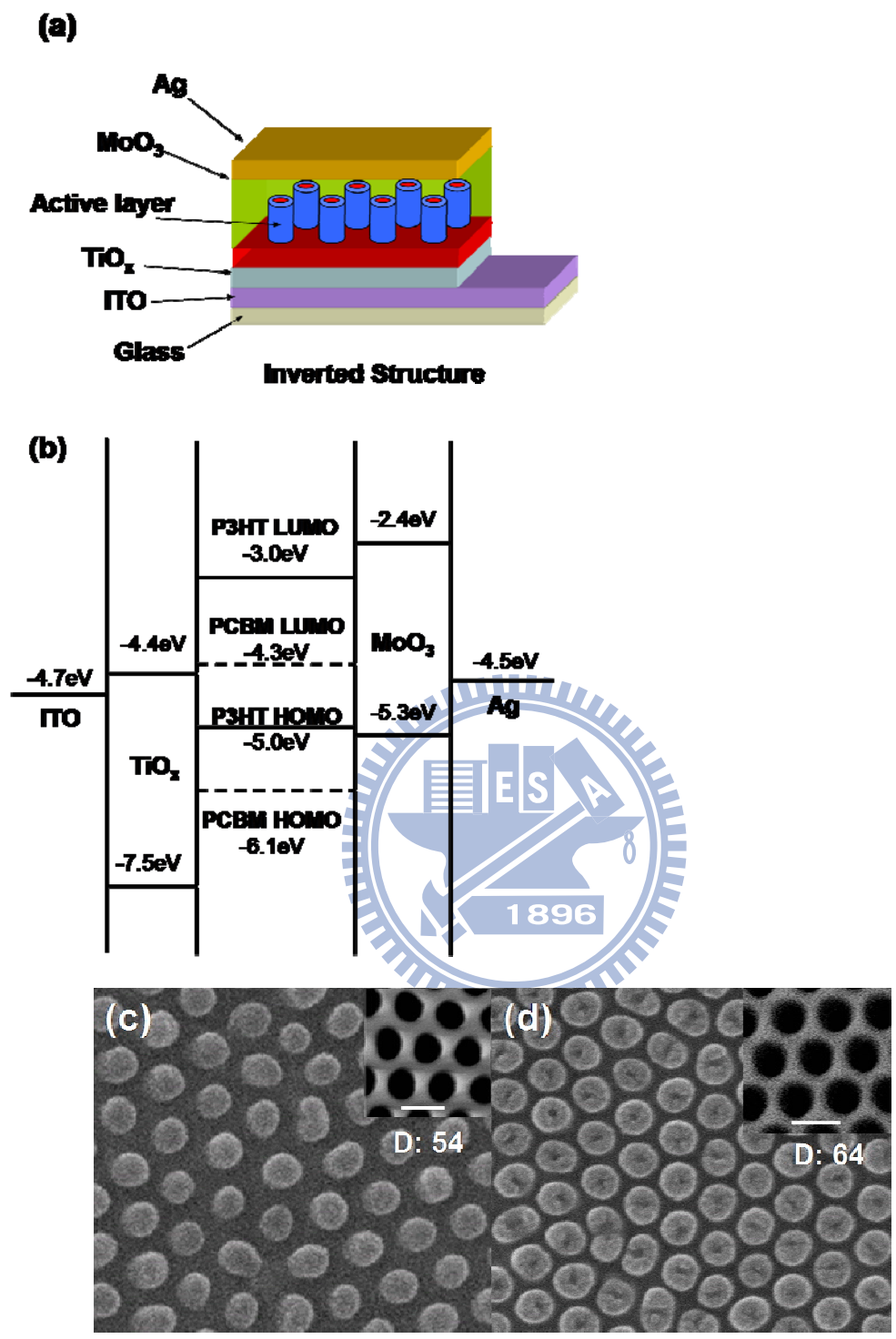


Figure 3-1

Figure 3-1. (a) Schematic representations of the inverted structure and the **PCBM/P3HT** core/shell structure of the inverted solar cell device. (b) Energy level diagram of the inverted solar cell device. And SEM images of **PCBM/P3HT** (1:1, w/w) nanorod arrays featuring nanorods having diameters and covered densities (D) on the substrate of (c) 70 nm and 54%, (d) 80 nm and 64%, respectively.

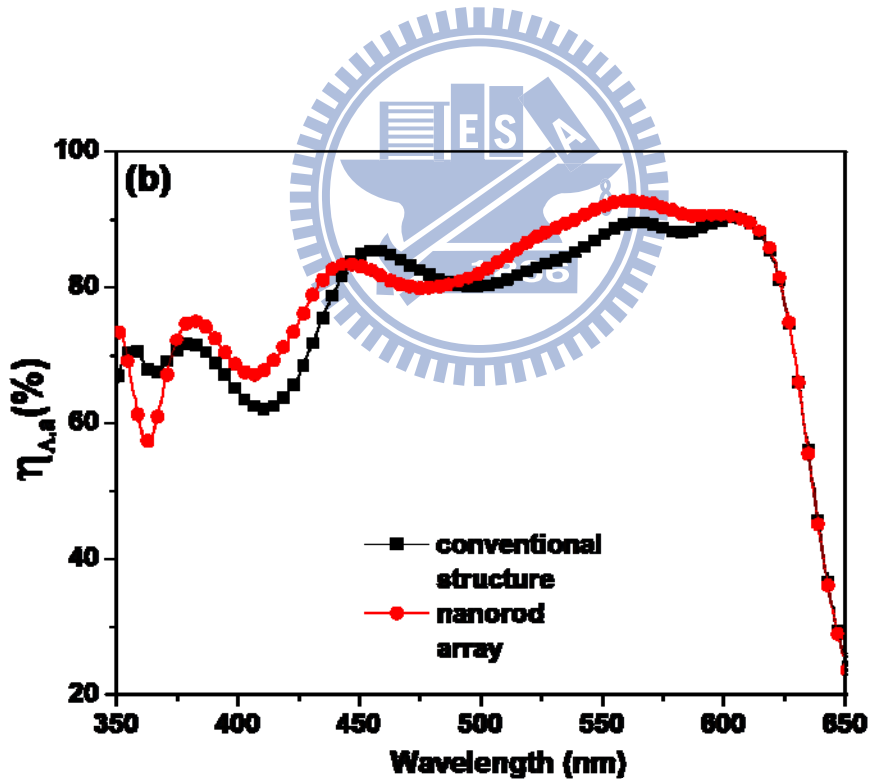
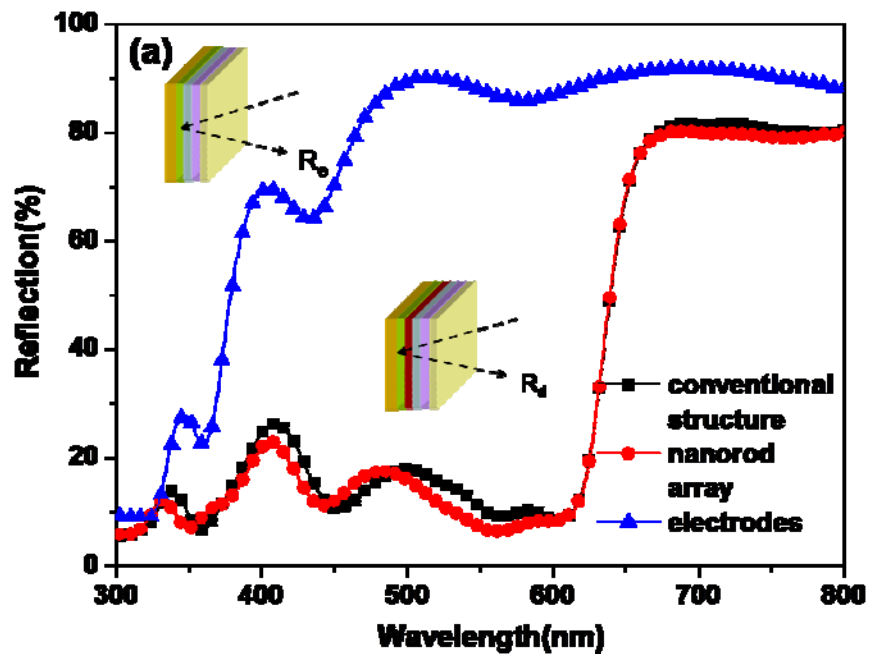


Figure 3-2

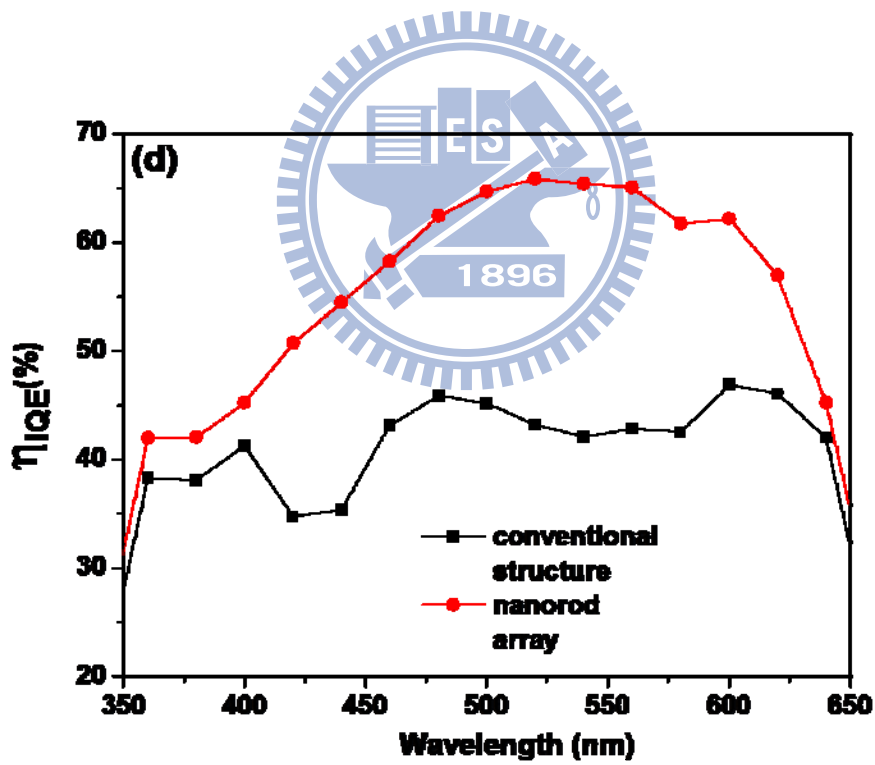
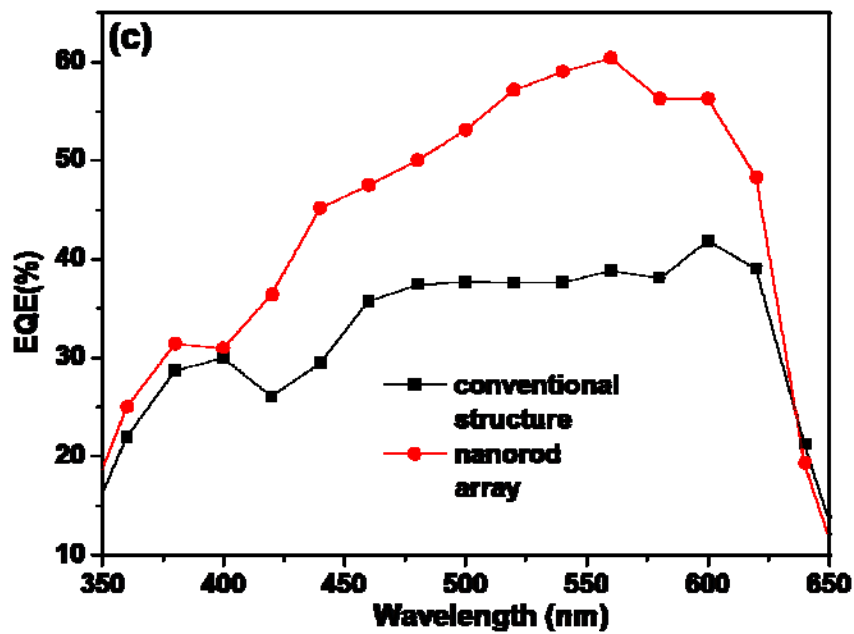


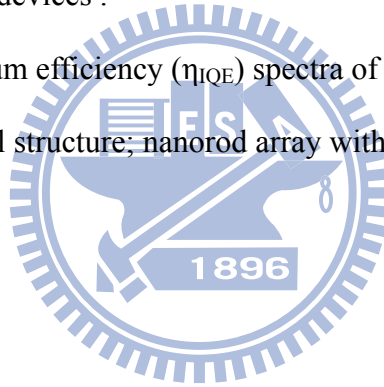
Figure 3-2

Figure 3-2. (a). Reflectance spectra of **PCBM/P3HT** nanorod array BHJ solar cell devices (conventional structure; nanorod array) and of the electrodes.
Device structure: glass/ITO (250 nm)/TiO_x (45 nm)/nanorod array(200nm long, 80nm diameter) /MoO₃ (20 nm)/Ag (80 nm); sample only with electrodes: a device fabricated without the active layer. Inset: Schematic representation of the incident light path in a completed device and sample only with electrode.

(b) Absorption efficiency ($\eta_{A,a}$) of the devices.

(c) EQE spectra of the nanorod array inverted devices and the conventional structure inverted devices .

(d) Internal quantum efficiency (η_{IQE}) spectra of **PCBM/P3HT** BHJ solar cells (conventional structure; nanorod array with diameter: 80 nm; length: 200 nm).



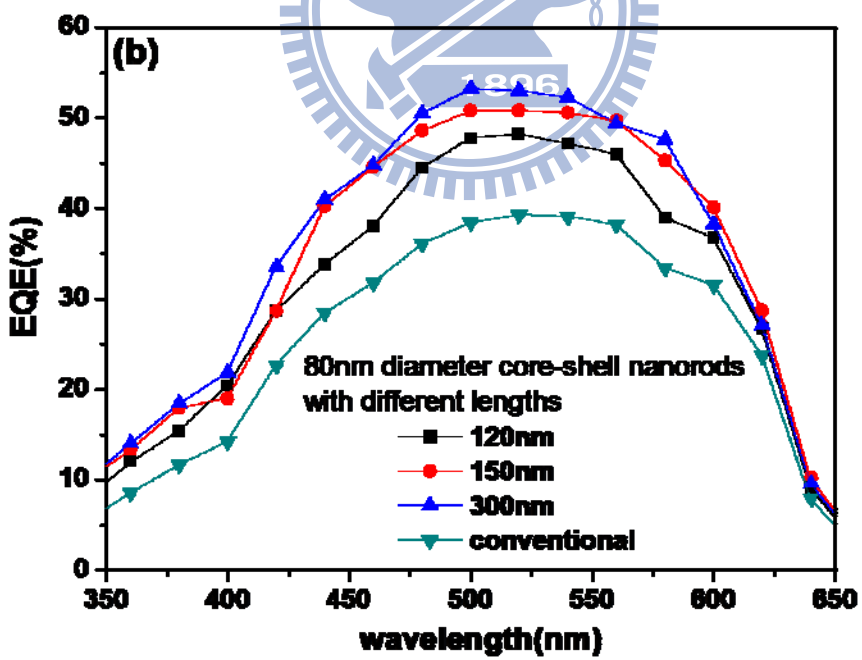
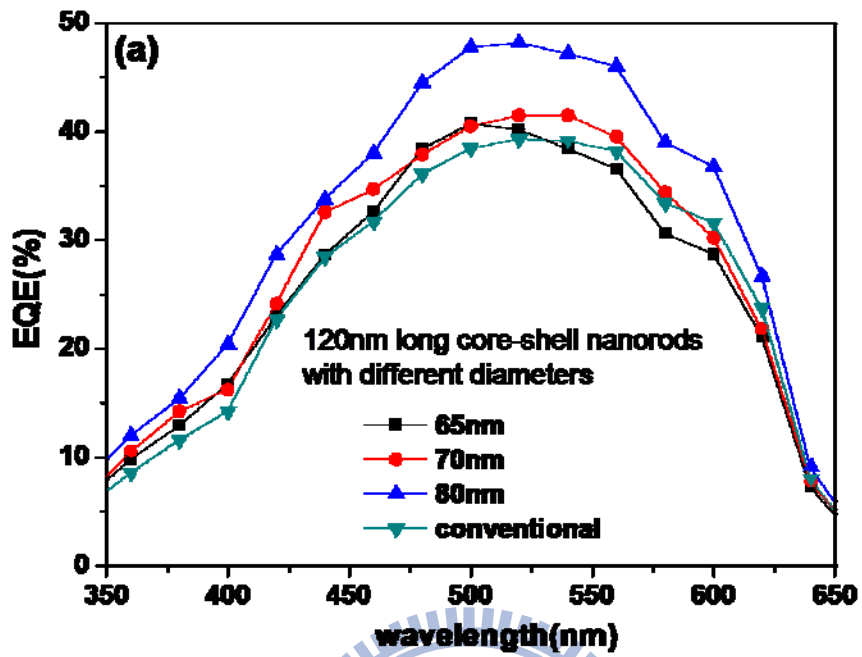


Figure 3-3

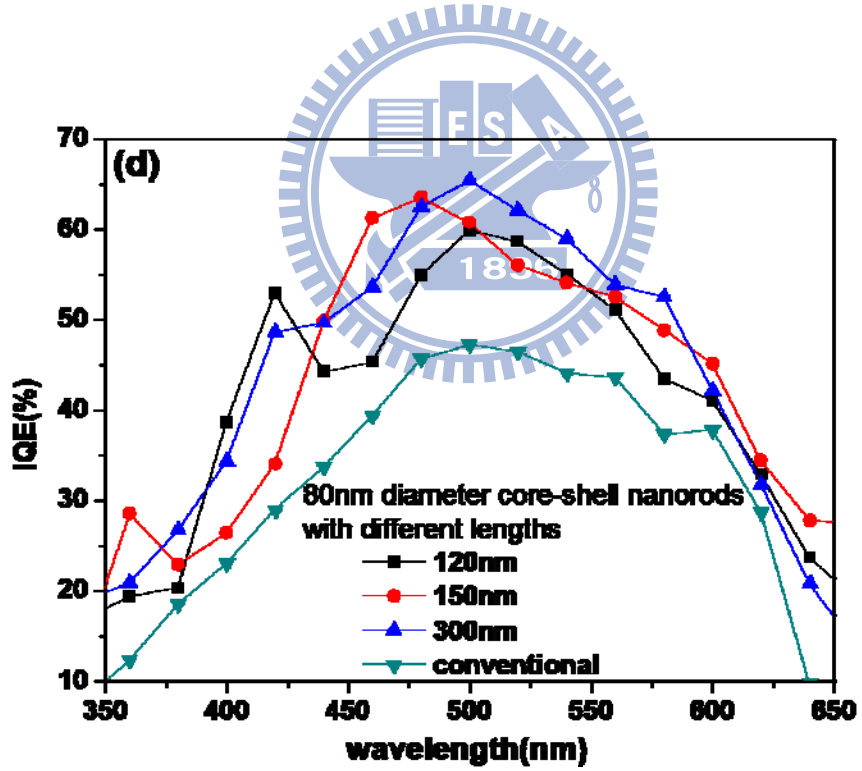
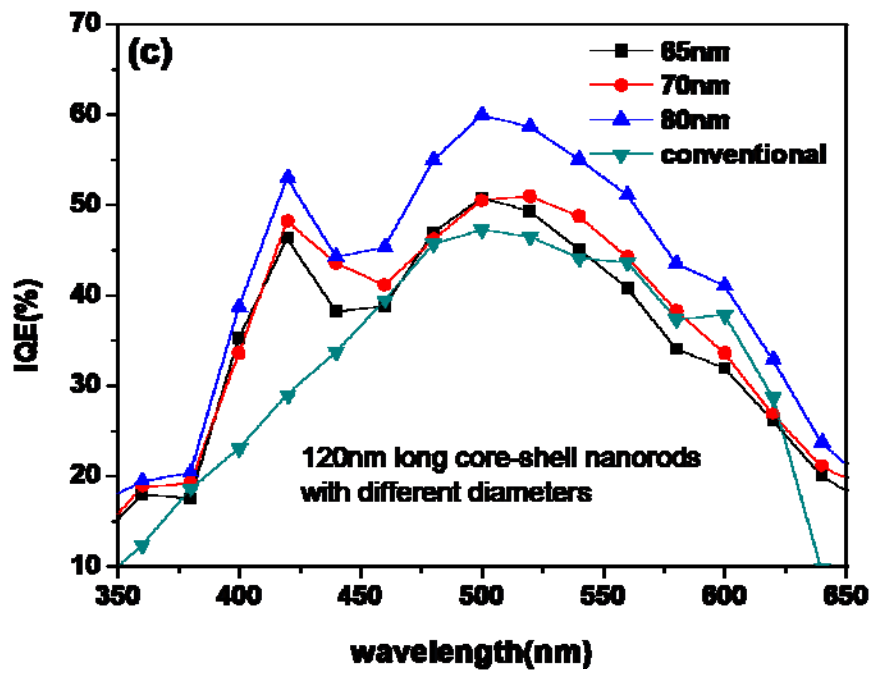
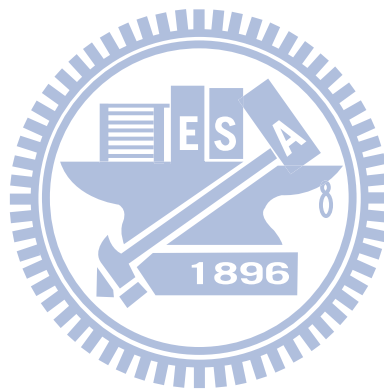


Figure 3-3

Figure 3-3. (a) the EQEs of 120nm length nanorods with diameter of 65, 70 or 80nm.
(b) the EQEs of 80nm diameter nanorods with length of 120, 150 or 300nm.
(c) the IQEs of 120nm length nanorods with diameter of 65, 70 or 80nm.
(d) the IQEs of 80nm diameter nanorods with length of 120, 150 or 300nm.



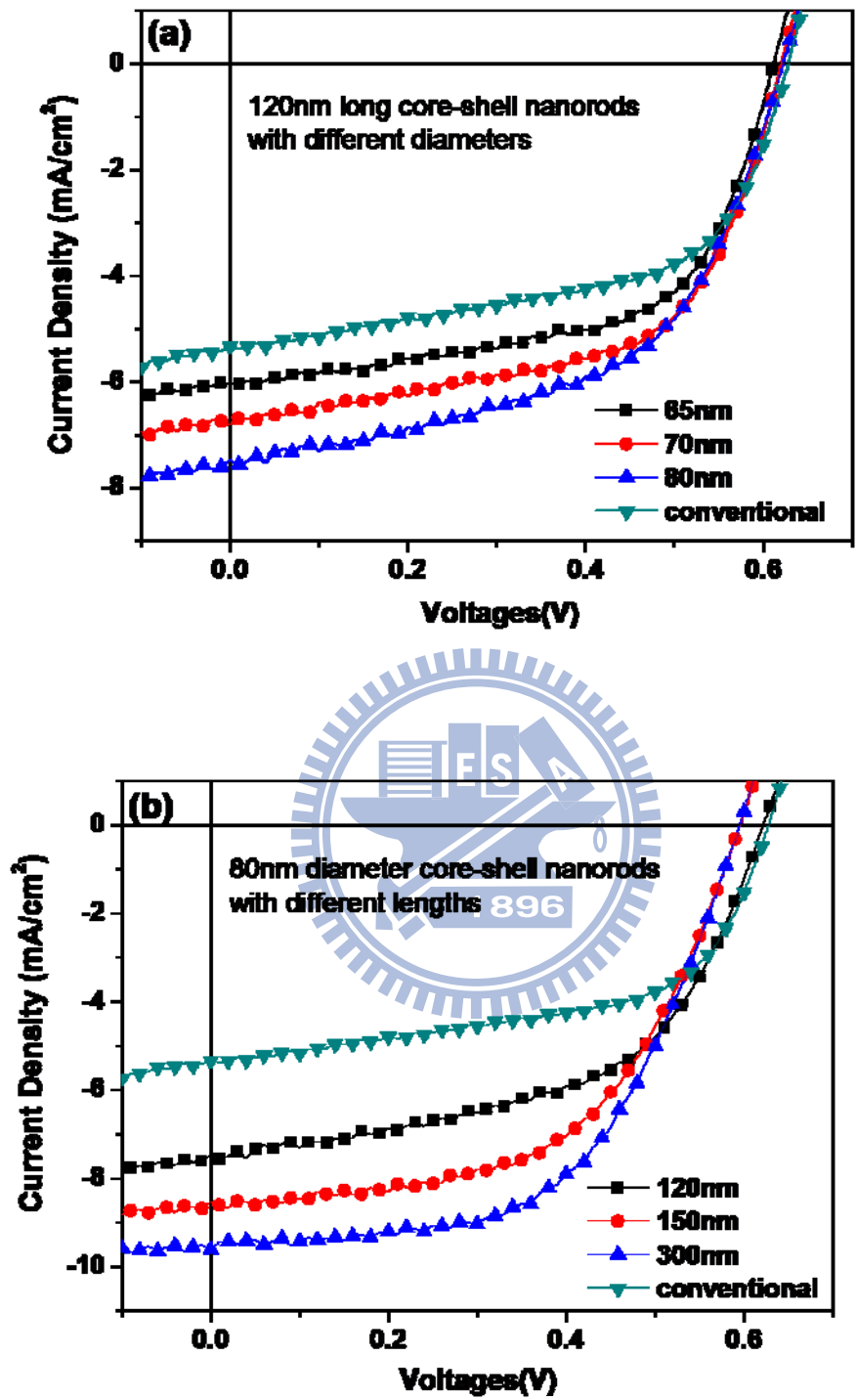


Figure 3-4

Figure 3-4. (a) $J-V$ characteristics of **PCBM/P3HT** nanorod array devices

incorporating 120-nm-length nanorods with diameter of 65, 70 and 80nm.

(b) $J-V$ characteristics of **PCBM/P3HT** nanorod array devices incorporating

80-nm-diameter nanorods having lengths of 120, 150, and 300 nm.

Devices were measured under AM 1.5G illumination at an intensity of 100

mW cm^{-2} . The thickness of active layer for conventional structure is 120nm.



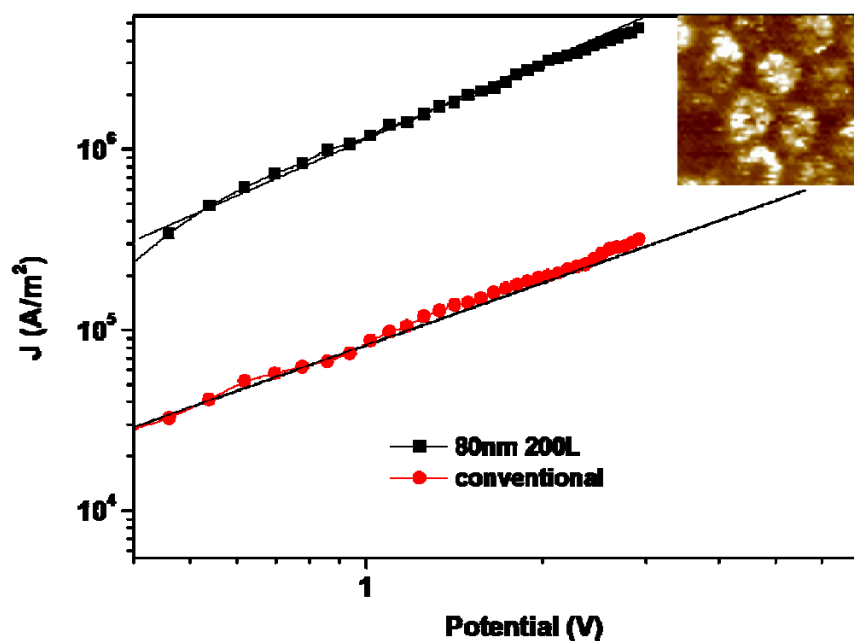


Figure 3-5

Figure 3-5. Conducting atomic force microscopy (C-AFM) dark $J-V$ curves for hole-dominated carrier samples incorporating **PCBM/P3HT** (0.8:1, w/w) in conventional structure and nanorod array structures. Inset: C-AFM current images of **PCBM /P3HT** nanorods.

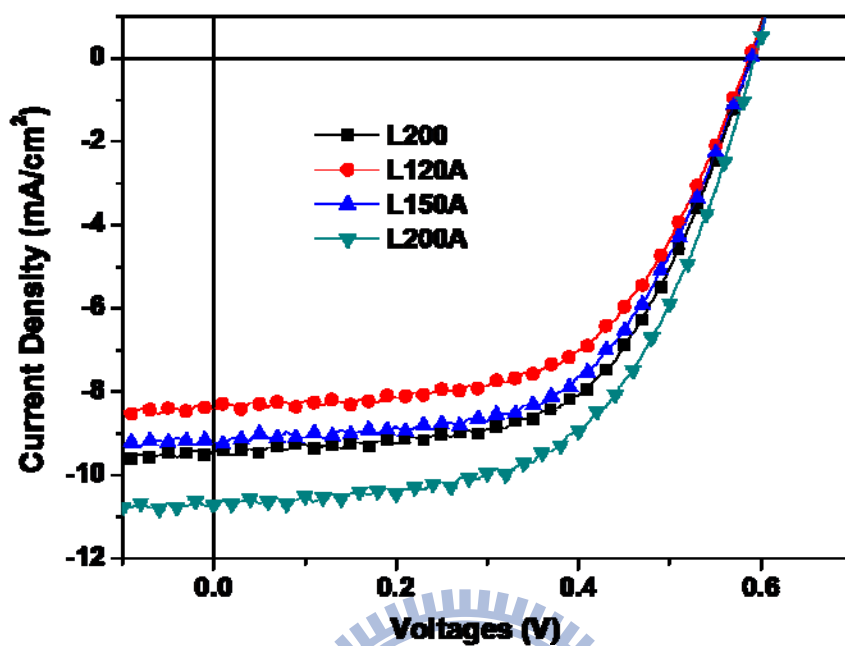


Figure 3-6

Figure 3-6. J - V characteristics of annealed PCBM/P3HT nanorod array devices incorporating 80-nm-diameter nanorods having lengths of 120, 150, and 200 nm. Devices were annealed at 120 °C for 10 min and then measured under AM 1.5G illumination at an intensity of 100 mW cm⁻².

Appendices

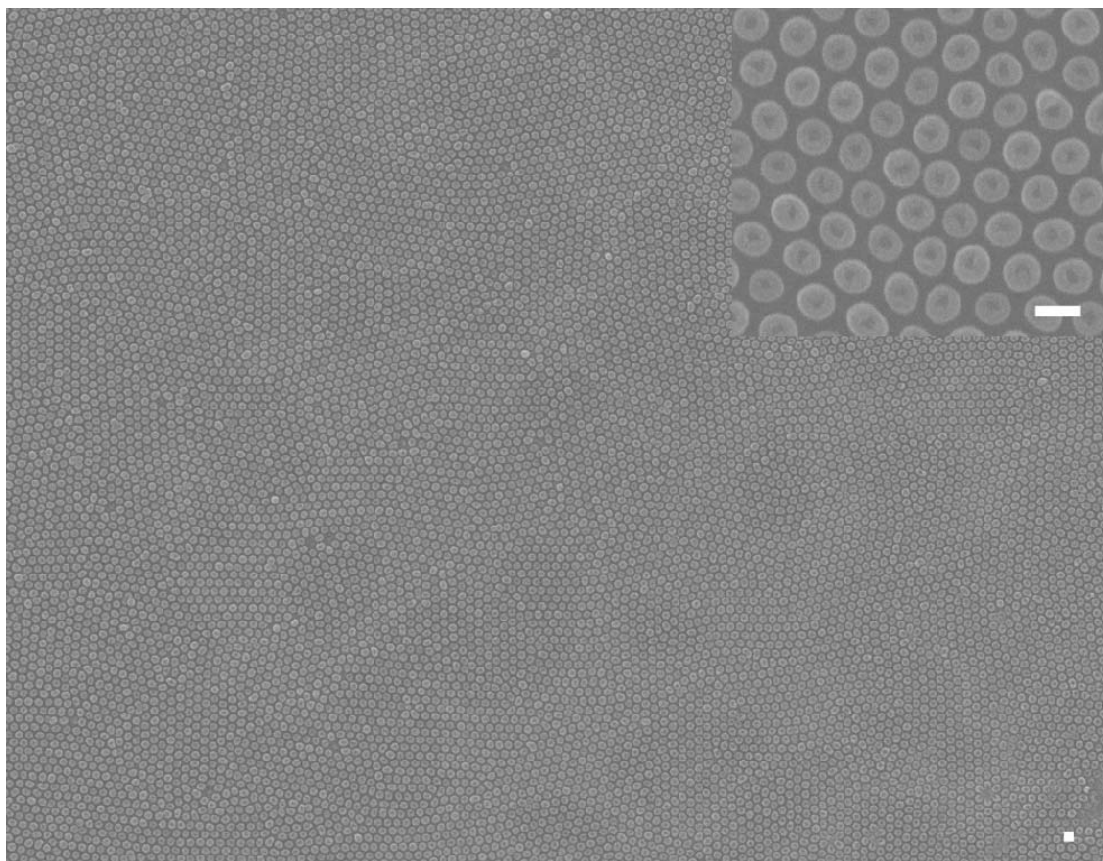


Figure A3-1. Large-area SEM image of the **PCBM/P3HT** (1:1, w/w) nanorod array; inset: magnified image (scale bar: 100 nm).

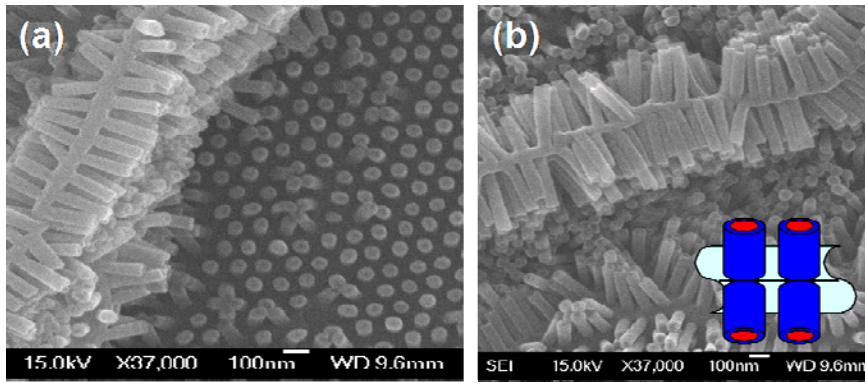


Figure A3-2. SEM images of PCBM/P3HT (1:1, w/w) nanorod arrays having lengths of (a) 200 and (b) 300 nm. Inset to (b): Cartoon representation of the structure in the cross-sectional image.

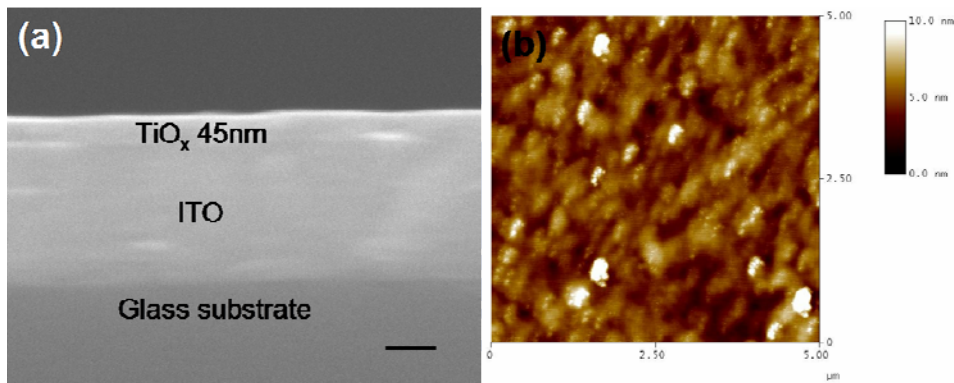


Figure A3-3. (a) Cross-sectional SEM image of ITO glass/TiO_x; the thickness of the TiO_x layer was 45 nm. (b) AFM image of glass/TiO_x surface; the RMS roughness of this film was 1.2 nm.

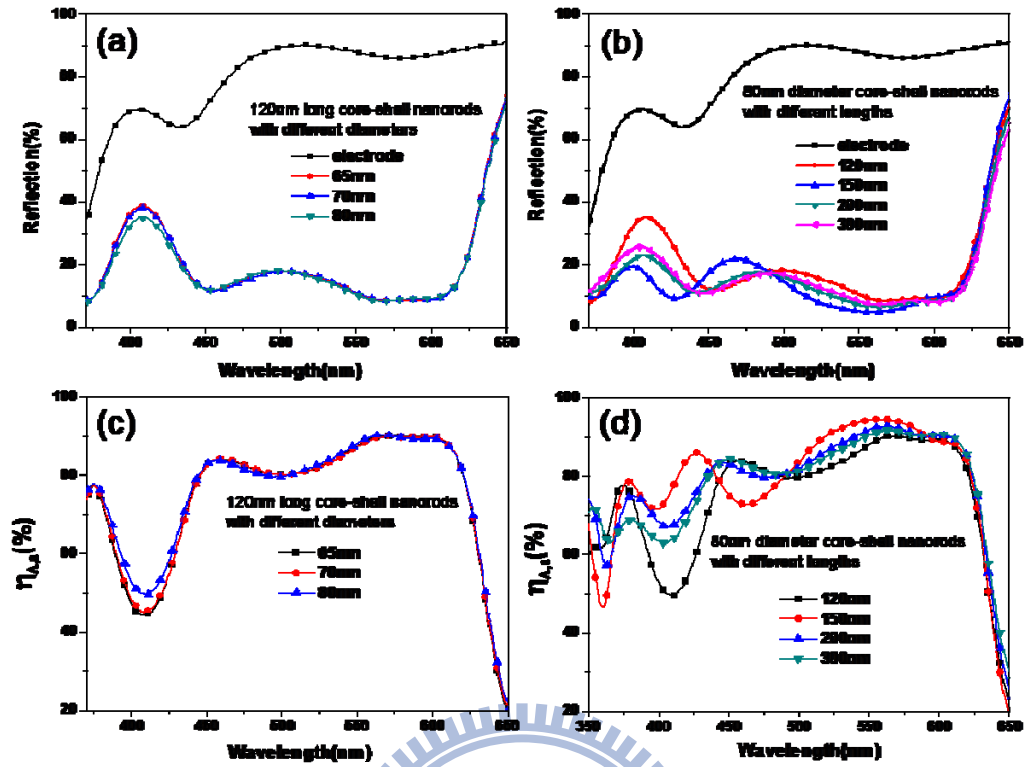


Figure A3-4. (a) and (b) reflectance spectra of PCBM/P3HT nanorod array with different diameters (65nm to 80nm) and length (120nm to 300nm) respectively, solar cell devices. (c) and (d) absorption efficiency ($\eta_{A,a}$) of the devices with different diameters and lengths, respectively.

Chapter 4:

Nanostructured Nanorod Arrays Presenting TiO₂ Nanorods/Poly(3-hexylthiophene) for Solar Cells Application

4-1. Introduction

The development of conjugated polymers for use in organic optoelectronic devices is an active field of research. In particular, polymer heterojunction solar cells have attracted much attention because of their potential application in large-area, flexible, low-cost devices.^[1,2,4-107-112] The power conversion efficiencies (PCEs) of bulk heterojunction (BHJ) solar cells have improved dramatically over the last few years. For example, the PCEs of BHJ solar cells incorporating regioregular poly(3-hexylthiophene) (P3HT) as the donor and [6,6]-phenyl-C₆₁-butyric acid methyl ester (PCBM) as the acceptor have recently reached values of ca. 4–5% under standard solar conditions (AM 1.5G, 100 mW/cm²).^[9-11, 14,113, 114] On the other hand, research into blends of conjugated polymers and inorganic nanocrystal has become quite attractive recently because such systems exhibit high electron mobility and chemical and physical stability. Nanocrystals such as CdSe, PbS, ZnO, and TiO₂ have been used as electron acceptor materials in polymer/inorganic nanocrystal solar cell.^[40, 64, 68, 115-117] Furthermore, the organic-inorganic alternative type of polymer solar cell, based on polymer/nanostructured inorganic nanocrystal device, is also an attractive topic for solar cell applications. In previous studies, a core/shell-structured

PCBM/P3HT nanorod arrays as the active layer, which was fabricated using an anodic aluminum oxide (AAO) membrane, to construct an inverted solar cell possessing more efficient carrier transport was developed.^[102,118]

The one dimensional nanostructure array has been widely applied as electron acceptor materials in organic electronic devices because of efficient charge carrier collection and transport. The TiO₂ and ZnO nanorod and/or nanotube arrays have previously been used as an electron transporting layer that have then been incorporated into photovoltaic cells with P3HT and PCBM blend.^[119-121] The performance of these devices was improved as a result of enhancement in photo-induced charge generation and collection. Furthermore, interpenetrating network of porous metal oxides^[52, 53, 122] and conjugated polymer have been applied as a hybrid polymer/metal oxide solar cell.

In this study, we use anatase TiO₂ nanorods/P3HT arrays as the active layer, which we fabricated using an anodic aluminum oxide (AAO) membrane, to construct an inverted solar cell. Our approach has several advantageous features: (i) the energy level of the highest occupied molecular orbital (HOMO) of the P3HT and the energy level of the lowest unoccupied molecular orbital (LUMO) of the TiO₂ nanorods can match that of the metal oxide electrodes deposited for electron and hole transport respectively; and (ii) the direct transport of electrons and holes along the

phase-separated TiO₂ nanorod-rich region and P3HT-rich region, respectively, occurs in the arrays. Hence, we expected that such composite rod array devices featuring inverted device geometry would provide more-efficient devices.

4-2 Experimental

Regioregular P3HT (4002-E, Rieke Metals), titanium isopropoxide (Alfa, 99.995%), oleic acid (OA) and trimethylamino-N-oxide dehydrate (TMAO), were obtained commercially. Synthesis of TiO₂ nanorods: The anatase titanium dioxide nanorod with high aspect ratio were synthesized by hydrolysis reaction of titanium isopropoxide and base solution according to the literature.^[123] Typically, 35 g of OA was dried at 120 °C for 1.5 h under vigorous stirring in a three-neck flask, after which it was cooled to 90 °C under nitrogen flow. First, 5 mmol of titanium isopropoxide was then added and stirred for 5 min; secondly, 5ml 2 M aqueous TMAO solution was rapidly injected. The mixture was maintained in a closed system at 100 °C for 6 h to promote further crystallization of the product. The TiO₂/OA nanorods were collected as powders by precipitation with ethanol. TiO₂/OA powder (60 mg) was dissolved in pyridine (3 mL) and then stirred at 75 °C for 6 h. Heptane (30 mL) was added to reprecipitate the TiO₂/pyridine NRs.

A solution of titanium isopropoxide (10 wt%) in isopropyl alcohol was spin-coated onto pre-cleaned ITO glass substrates under a N₂ ambient and then it was

converted to 40-nm-thick TiO_x via hydrolysis at room temperature in air for 2 h. The substrate was then heated at 450 °C for 30 min to complete the hydrolysis reaction.

TiO_2 nanorod/P3HT films of various compositions were prepared through solution casting onto ITO/ TiO_x substrates; an AAO membrane was then placed on top of the TiO_2 nanorod/P3HT films. This TiO_2 nanorod:P3HT film/AAO membrane was sandwiched between two glass slides and then placed in an oven and annealed at 120 °C under vacuum. After 6 h, the assembled system was cooled to room temperature.

Dissolving the alumina membranes in 10 wt% NaOH solution released the TiO_2 nanorod/P3HT nanorod array structures, which were dried under vacuum for 12 h prior to characterization. SEM images of the resultant TiO_2 nanorod/P3HT nanostructures were recorded using a JEOL 6500 scanning electron microscope operated at an accelerating voltage of 15 kV. The samples were coated with a thin (ca. 3 nm) layer of Pt prior to SEM imaging.

The current density–voltage (J – V) characteristics of the polymers were measured using devices having the structure ITO/ TiO_x / TiO_2 nanorod:P3HT / MoO_3 /Ag. The ITO-coated glass substrate was pre-cleaned and treated with oxygen plasma prior to use. The TiO_x layer was prepared using the spin-coating process described above. The TiO_2 nanorod/P3HT layer was spin-coated from a chlorobenzene solution. Using a base pressure of less than 1×10^{-6} torr, layers of MoO_3 (20 nm) and Ag (80 nm) were

vacuum-deposited to form the anode.

The devices were tested under simulated AM 1.5G irradiation (100 mW cm^{-2}) using a Xe lamp-based Newport 66902 150W solar simulator equipped with an AM1.5 filter as the white light source; the optical power at the sample was 100 mW cm^{-2} , detected using an OPHIR thermopile 71964. The $J-V$ characteristics were measured using a Keithley 236 source-measure unit. The EQEs were measured using a Keithley 236 source-measure unit coupled with an Oriel Cornerstone 130 monochromator. The light intensity at each wavelength was calibrated using an OPHIR 71580 diode.

The Hole-only sample, used to investigate hole transport in the polymer/ TiO_2 nanorod layers, were fabricated with the structure of ITO/PEDOT/rod arrays. The $J-V$ curves was measured using a conductive atomic force microscopy (C-AFM) experiments using platinum-coated silicon cantilevers [NanoSensors Inc. (PPP-ContPt, spring constant $k = 0.2 \text{ N/m}$), tip diameter $\sim 20\text{nm}$] and a Digital Nanoscope IV operated under ambient conditions. For $J-V$ measurement of C-AFM, we determined the contact area between tip and sample assuming a 20nm diameter circle. The $J-V$ curves from each sample were averaged from four different regions.

4-3 Results and Discussion

Figures 4-1a and 4-1b provide a schematic representation of the anatase TiO₂ NRs/P3HT arrays in an inverted solar cell structure and the energy level diagram for each material, respectively. In this rod-based device architecture, the TiO_x layer between the ITO glass and the active layer is an appropriate material for the electron-collecting ITO bottom electrode. The energy level of the LUMO of TiO_x is -4.4 eV, which suggests that electrons (similar with LUMO of nanocrystal of TiO₂ nanorod; -4.2 eV^[124]) can be injected into the TiO_x interlayer, while the holes from the active layer blend levels can be effectively blocked (HOMO of TiO_x: -7.5 eV). In this study, the configuration of the device, stacked from bottom to top, was ITO/TiO_x/TiO₂ NRs:P3HT arrays/MoO₃/Ag. Here, the hole transport layer (MoO₃) was deposited on the composite rod arrays as a hole-selecting layer.

Figure 4-2(a) displays the TEM image of TiO₂ nanorods with 20-30 nm in length and 5-7 nm in diameter, with an aspect ratio of 4. Figure 4-2(b) shows the XRD patterns of the TiO₂ nanorods, revealing an anatase characteristic pattern.

We used melt-assisted wetting of ordered AAO templates to fabricate the TiO₂ nanorod/P3HT rod array structure. The phase separation of the TiO₂ nanorod/P3HT blends during the wetting of porous AAO membrane was determined by the flow-induced shear stress, and its mechanism was similar to that of PCBM/P3HT rod

arrays as described in a previous report^[102]. Figure 4-3 displays transmission electron microscopic (TEM) images of cross-section and top view of pure P3HT array and TiO₂ nanorod/P3HT array with different weight ratio. Figure 4-3(a) and 4-3(b) show the cross-sectional and top view TEM images of pure P3HT array, respectively. In Figure 4-3 (a) and (b), it was revealed that P3HT rod has a diameter of 80nm and a length of 110nm. The averaged diameter of the P3HT rod was equal to that of the nanopores in the ordered AAO template, revealing our good control over the nanorod diameter. Figure 4-3(c) shows the cross-sectional TEM image of TiO₂/P3HT (1:1, w/w) composite rod arrays; it reveals that these rods consist of the phase separated P3HT-rich region and the TiO₂-rich region, with TiO₂ nanorods bundles aligned at about the same direction of the rod arrays. Figure 4-3(d) provides a TEM top-view image of the TiO₂/P3HT (1:1, w/w) arrays, the dark region of the composite rods represents the TiO₂-rich region, which has a higher electron density than that of the P3HT-rich region.

The TiO₂ nanorods/P3HT composite rod arrays have been characterized using absorption and photoluminescence (PL) spectroscopy. Figure 4-4(a) displays the UV spectra of these rod arrays structure. The absorbance at 250 to 300nm region is increased upon increasing the concentration of TiO₂ nanorods. The vibronic absorption peak of the $\pi-\pi^*$ transition of P3HT is at the 400-650nm region; it is a

manifestation of degree of π - π stacking of thiophene planes. Introducing the TiO₂ nanorods to the polymer, however, weakens this π - π stacking and therefore the vibronic shoulders, causing composite rod arrays to have vibronic shoulders weaker than that of pure P3HT rod array. Figure 4-4(b) displays the photoluminescence (PL) spectra of TiO₂ nanorods/P3HT rod arrays with various weight ratios. The PL spectra are recorded at an excitation wavelength of 500 nm, and the extend of PL quenching increases with the concentration of TiO₂ nanorods as compare to that of the P3HT rod arrays.

Figure 4-5 displays C-AFM images of the TiO₂ nanorods/P3HT (1:1, w/w) rod arrays embedded onto the ITO/PEDOT substrate. Figure 4-5(a) shows the topographic image of the samples; the light regions having a height of ca. 100 nm represent the TiO₂ nanorods/P3HT rod arrays. Figure 4-5(b) shows the current image of TiO₂ nanorods/P3HT rod arrays, measured at a sample bias of -1 V. The current range of the TiO₂ nanorods/P3HT rod arrays was ca. 20 pA. The measured current resulted mainly from the hole transport from Pt to ITO because Pt and ITO have work functions of ca. 5.7 and 4.8 eV, respectively. We observed a variation in the current image between the TiO₂-rich region and P3HT-rich regions, where the bright region for the rod array is the P3HT-rich region and the relative dark region for the rod arrays is the TiO₂-rich region. Therefore, we expected most of the electron/hole pairs to

separate at the p–n interface, such that the electron and hole transport would occur through the TiO₂-rich region (n-type) and P3HT-rich region (p-type) individually and efficiently in this structure.

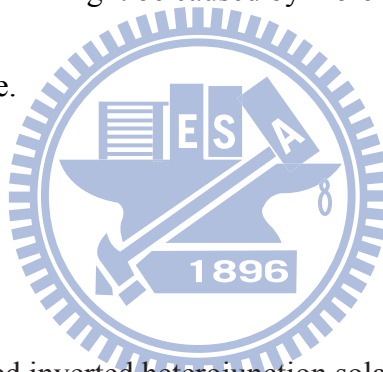
Figure 4-6 presents the dark J – V curves by hole-dominated conductive atomic force microscopy measurement. We determined the hole mobilities by fitting the dark J – V curves into the space charge–limited current (SCLC) model^[106] using the equation

$$J = 9\varepsilon_0\varepsilon_r\mu_h V^2/8L^3 \quad (1)$$

where ε_0 is the permittivity of free space, ε_r is the dielectric constant of the polymer, μ_h is the hole mobility, V is the voltage drop across the device, and L is the polymer thickness. The pure P3HT rod arrays has the highest hole mobility of $1.75 \times 10^{-4} \text{ cm}^2 \text{ V}^{-1} \text{ s}^{-1}$. Upon the incorporation of TiO₂ nanorod, the π – π stacking structure of P3HT is weakened. The hole mobility of the TiO₂ nanorod/P3HT (1:1) blend film is $8.25 \times 10^{-5} \text{ cm}^2 \text{ V}^{-1} \text{ s}^{-1}$. The hole mobility of /P3HT rod arrays was increased to $1.52 \times 10^{-4} \text{ cm}^2 \text{ V}^{-1} \text{ s}^{-1}$ for TiO₂ nanorod/P3HT (1:1) from $1.04 \times 10^{-4} \text{ cm}^2 \text{ V}^{-1} \text{ s}^{-1}$ for TiO₂ nanorod/P3HT (0.8:1).

Figure 4-7 displays the J – V characteristics of solar cell devices incorporating different TiO₂ nanorod concentrations. J – V curves shows that the short current densities (J_{sc}) and power conversion efficient (PCE) increased to 7.47 mA cm^{-2} and

2.41%, respectively, for TiO₂ nanorod/P3HT (1:1, w/w) rod arrays from 5.19 mA cm⁻² and 1.63% for TiO₂ nanorod/P3HT rod arrays (0.8:1, w/w) at a fixed length of 120nm. The open circuit voltage (V_{oc}) increased to 0.67 V for TiO₂ nanorod/P3HT (1:1, w/w) rod arrays from 0.62V for TiO₂ nanorod/P3HT rod arrays (0.8:1, w/w). Table 1 summarizes the performance factors of the devices with different TiO₂ nanorod/P3HT weight ratio with annealing at 120°C for 15min. This improvement in the PCE of the device containing TiO₂ nanorod/P3HT rod arrays over that of the devices containing TiO₂ nanorod/P3HT blend film might be caused by more efficient electrons and holes transport in the rod structure.



4. Conclusion

We have fabricated inverted heterojunction solar cell devices incorporating titanium dioxide nanorod/poly (3-hexylthiophene) (P3HT) rod arrays using melt-assisted anodic alumina oxide template. The transmission electron microscopy and conductance atomic force microscopy images revealed that phase-separated TiO₂ rich (n-type) and P3HT rich (p-type) regions presents in these rod arrays. This improvement in the PCE of the device containing TiO₂ nanorod/P3HT rod arrays over that of the devices containing TiO₂ nanorod/P3HT blend film might be caused by more efficient electrons and holes transport in the rod structure.

Acknowledgements: We are grateful for the financial support provided by the National Science Council through Project NSC 97-2120-M-009-006.



TABLE 1. Electronic parameters of one dimensional structure array devices prepared from various P3HT/TiO₂ nanorod weight ratios.

P3HT/ TiO ₂ weight ratio	J_{sc}^a (mA/cm ²)	V_{oc}^b (V)	FF ^c (%)	η^d (%)
blend film	3.91	0.54	62	1.31
1:0.8	5.19	0.62	51	1.63
1:1	7.47	0.67	48	2.41
1:1.2	6.94	0.67	42	2.15

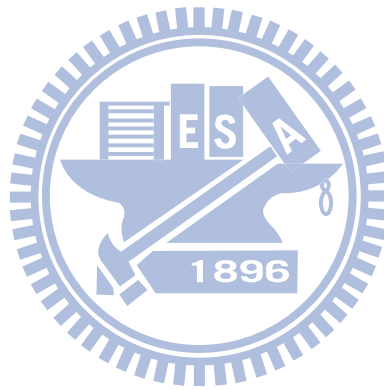
^a Short-circuit current density.

^b Open circuit voltage.

^c Fill factor.

^d Power conversion efficiency.

Annealing condition: 120°C for 15 min.



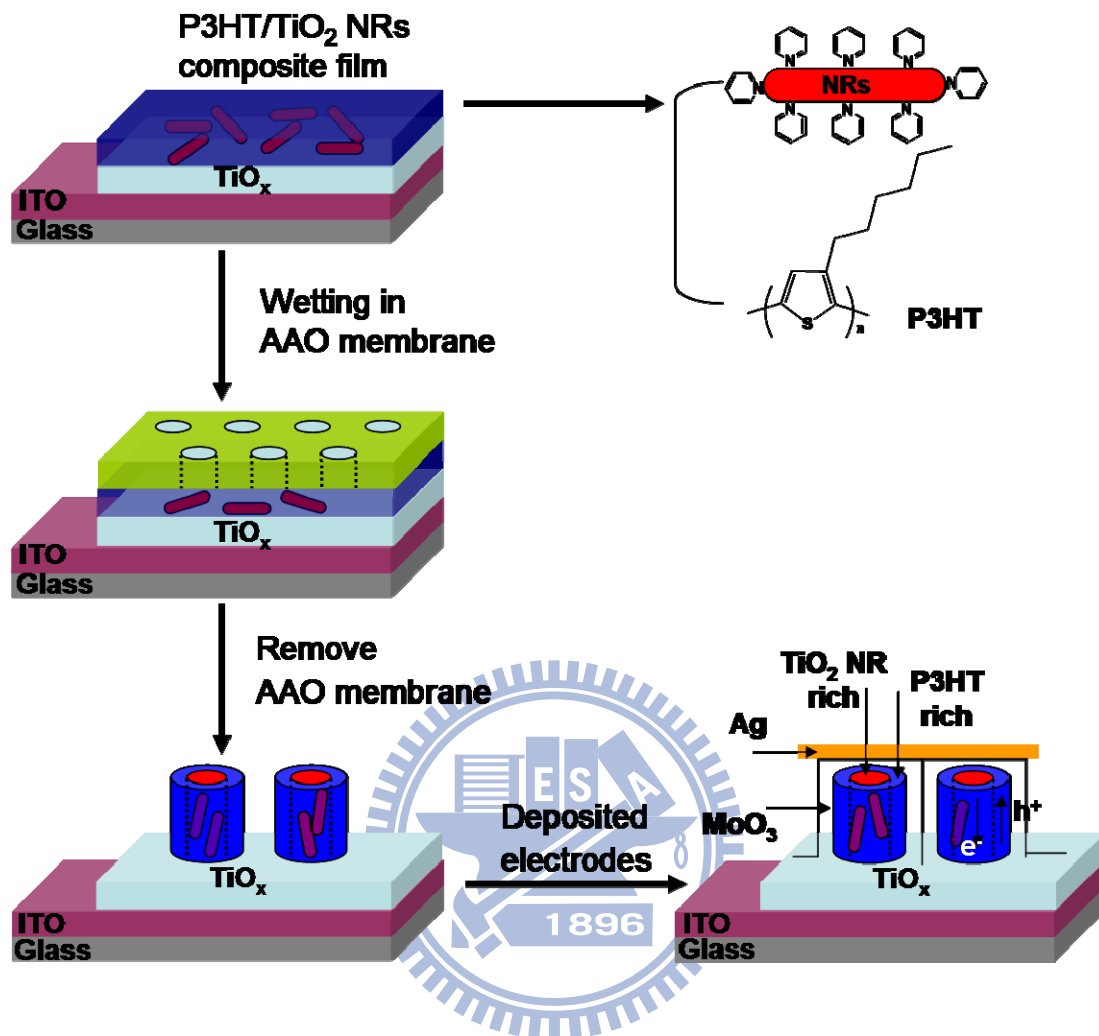


Figure 4-1. Schematic representations of the TiO₂/P3HT nanorod core/shell structure of the inverted solar cell device.

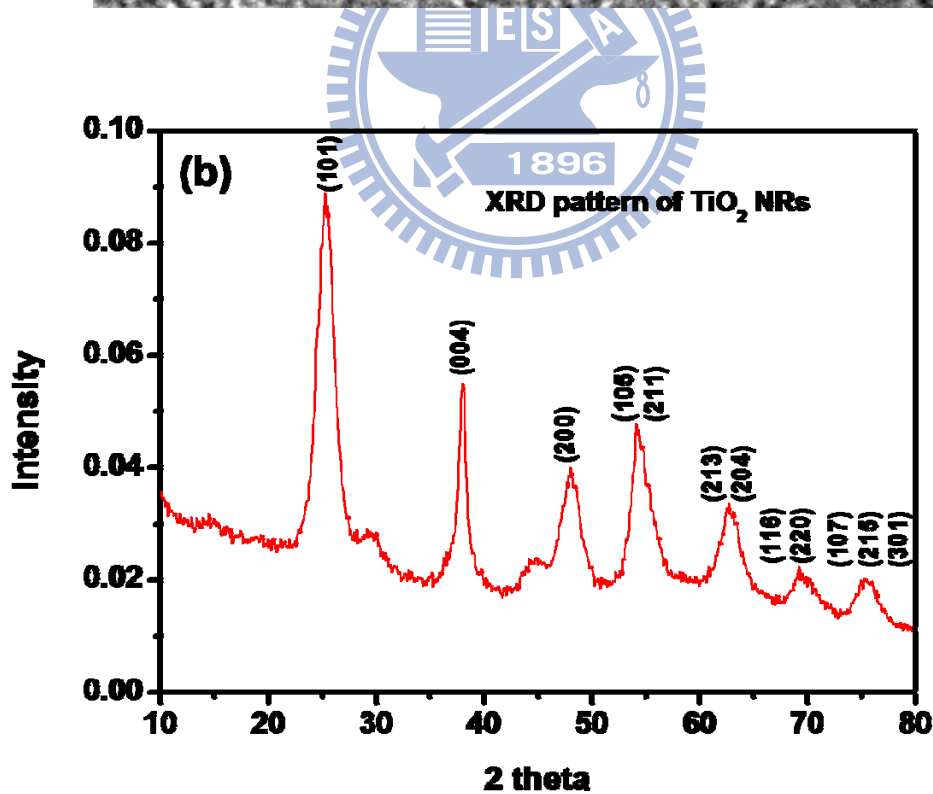
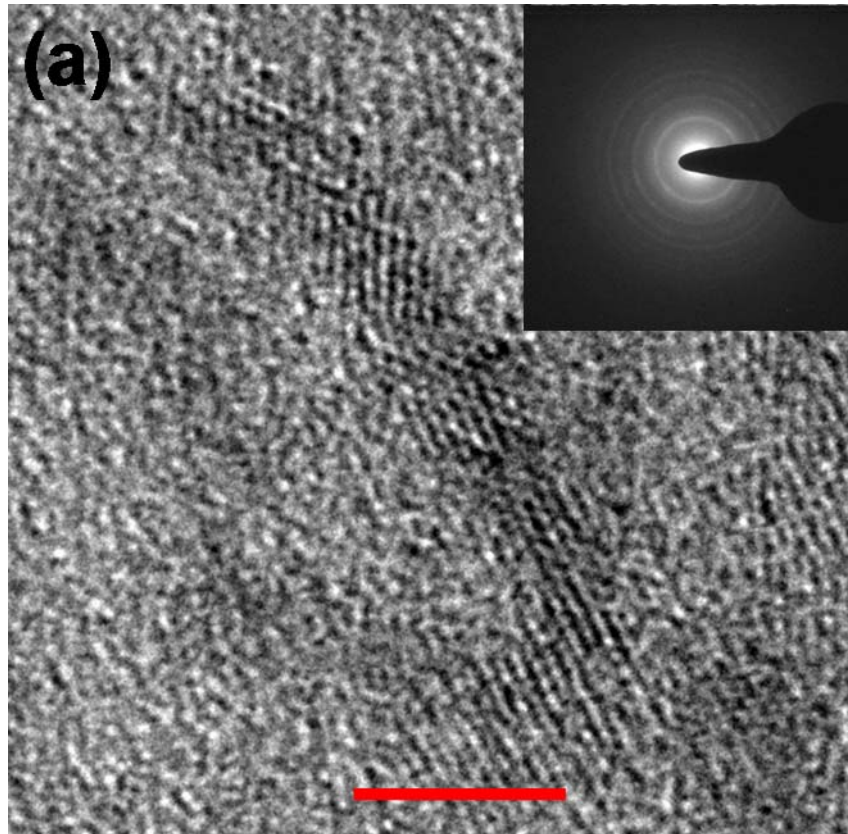


Figure 4-2. (a) High-resolution TEM (HRTEM) image of TiO_2 nanorods. The scale bar is 20nm. (b) X-ray diffraction pattern of TiO_2 nanorods.

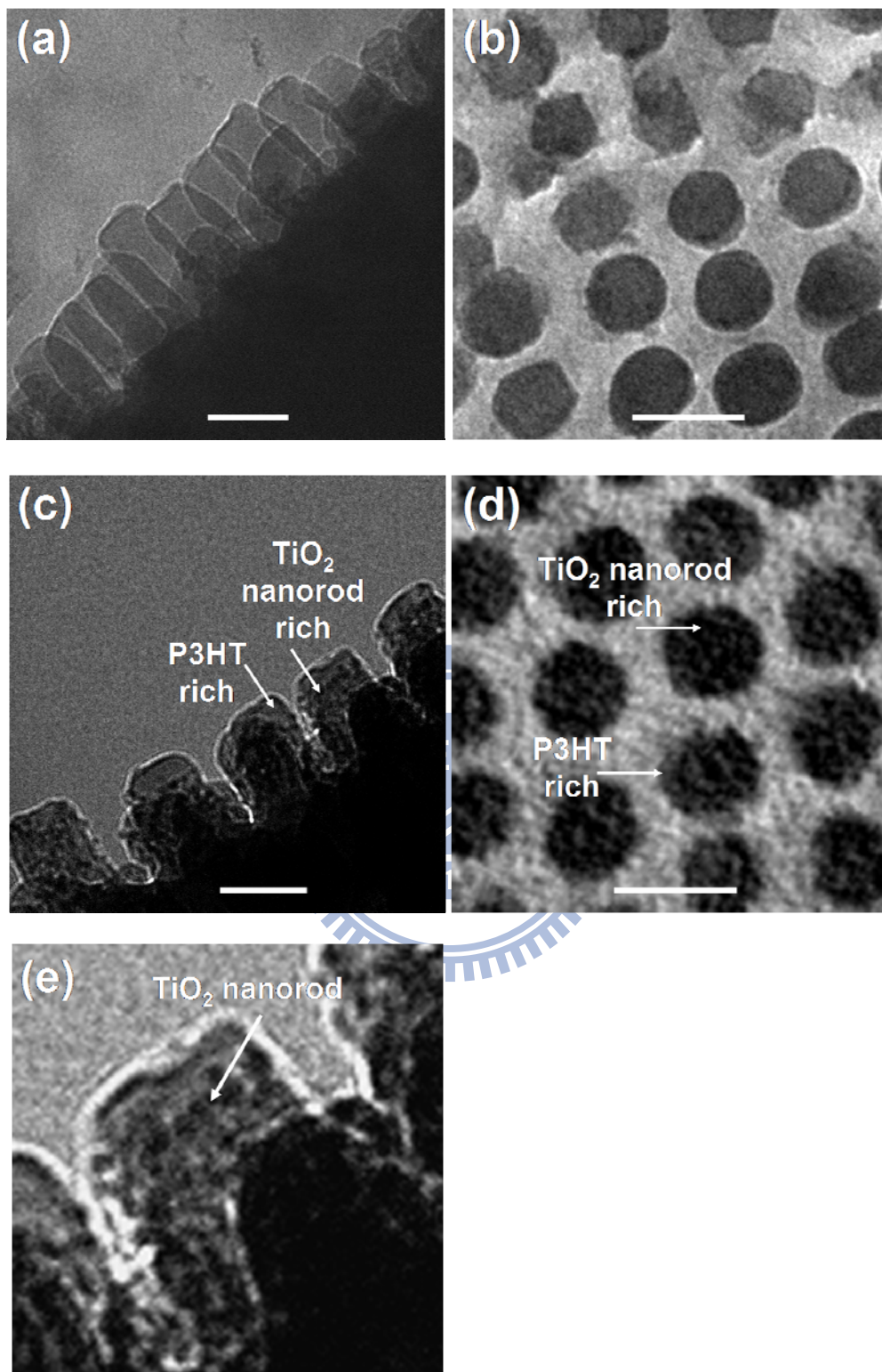


Figure 4-3. The TEM images of cross-section and top view of pure P3HT nanorod array and TiO₂ nanorod/P3HT nanorod array with different weight ratio. (a), (b) for pure P3HT, (c), (d), (e) for TiO₂ nanorod/P3HT: w/w=1/1. The scale bar is 100nm.

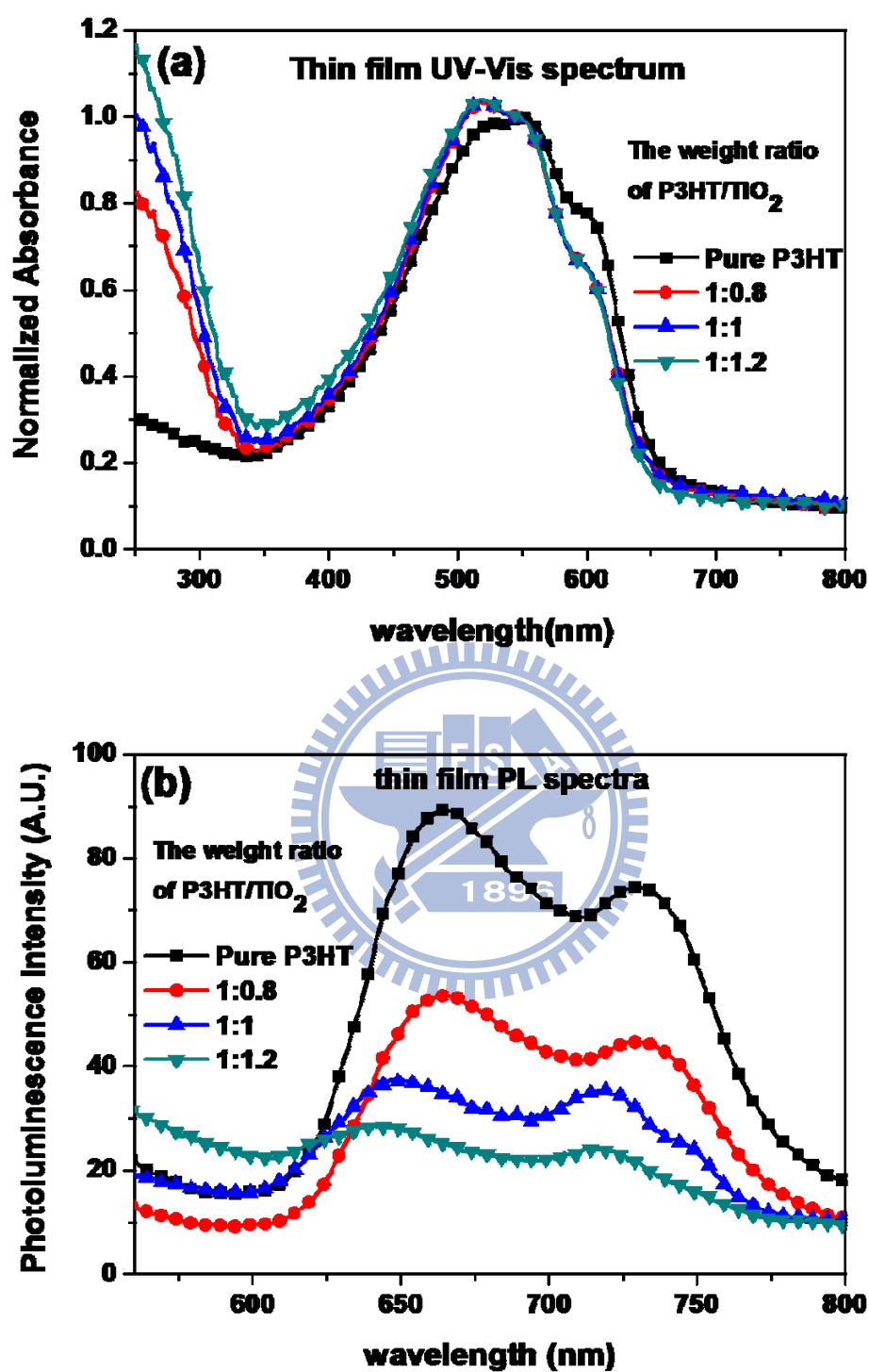


Figure 4-4. (a) Normalized optical absorption spectra of the nanorod arrays with different weight ratio of P3HT/TiO₂ and pure P3HT. (b) PL spectra of nanorod arrays, recorded at an excitation wavelength of 500 nm. The size of the nanorod is 110nm long with 80nm diameter.

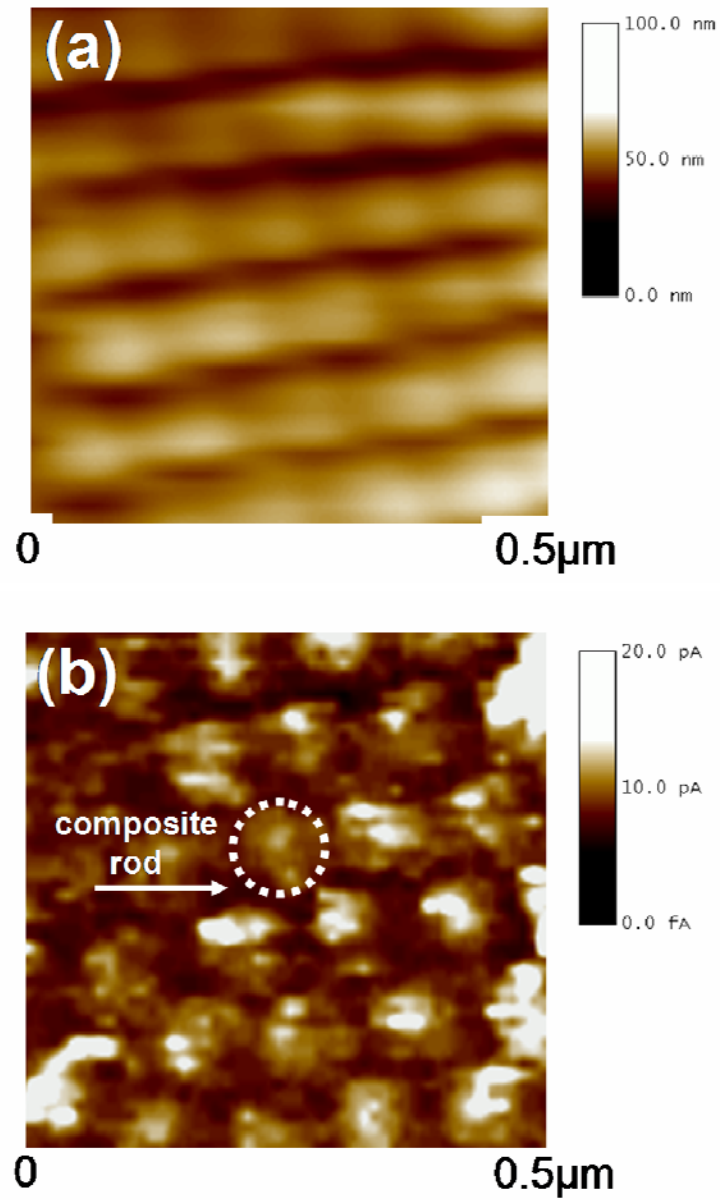


Figure 4-5 C-AFM image (Image size: $0.5 \mu\text{m} \times 0.5 \mu\text{m}$) of TiO_2 nanorod/P3HT array (a) topographic image. (vertical distance: 100 nm) and (b) current images of a thin film of TiO_2 nanorod/P3HT array; Z-range: 20 pA.

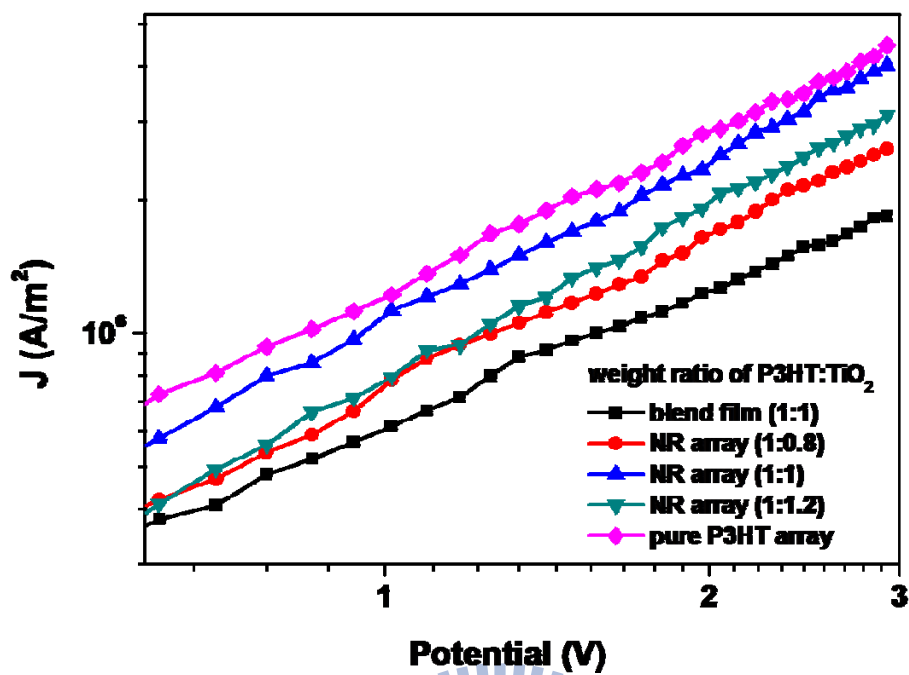
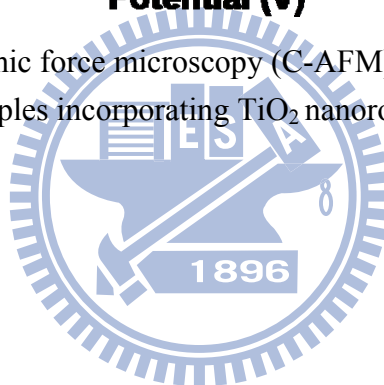


Figure 4-6 Conducting atomic force microscopy (C-AFM) dark $J-V$ curves for hole-dominated carrier samples incorporating TiO_2 nanorod/P3HT arrays.



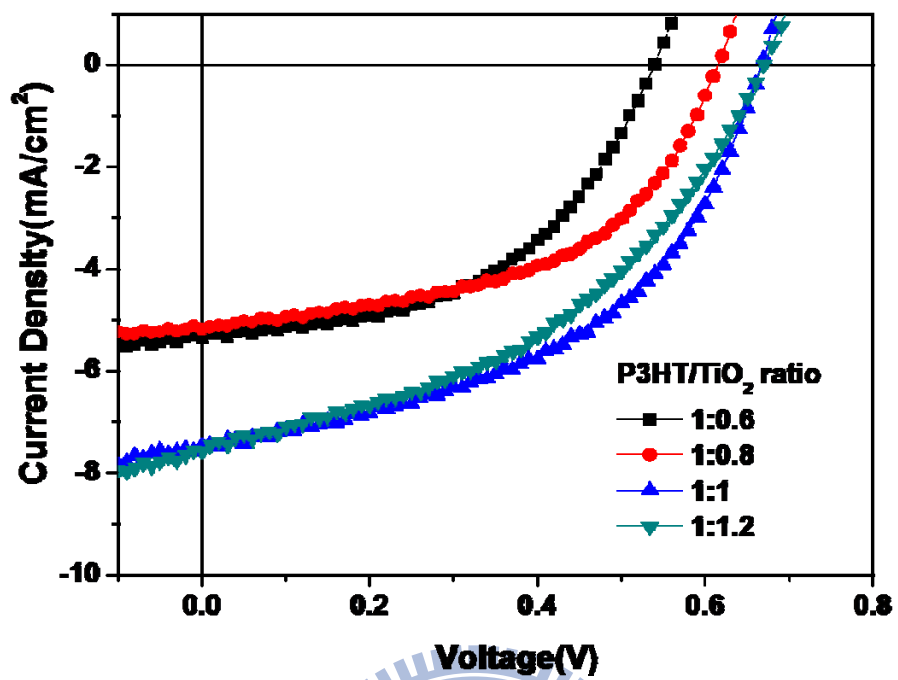
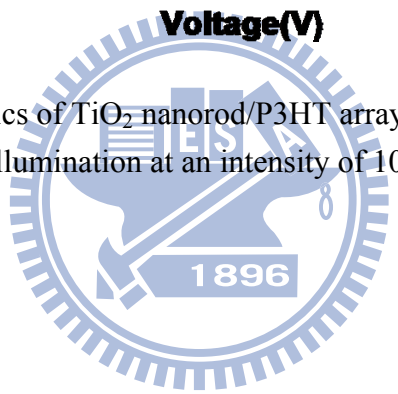


Figure 4-7 J - V characteristics of TiO_2 nanorod/P3HT array devices. Devices were measured under AM 1.5G illumination at an intensity of 100 mW cm^{-2} .



Chapter 5: Synthesis and Characterization of Donor–Acceptor Poly(3-hexylthiophene) Copolymers Presenting 1,3,4- Oxadiazole Units and Their Application to Photovoltaic Cells

5-1 Introduction

Conjugated polymers possessing extended delocalized π electrons are being investigated intensively for their potential uses in such organic optoelectronic devices as light emitting diodes (LEDs), thin film transistors, and photovoltaic cells incorporating bulk heterojunctions.^[1,10, 107, 110,107, 125-129] Bulk heterojunctions based on blends of poly(3-hexylthiophene) (P3HT) and [6,6]-phenyl-C₆₁-butyric acid methyl ester (PCBM) have recently reached power conversion efficiencies of ca. 4–5% under standard solar illumination (AM 1.5G, 100 mW cm⁻²).^[12, 92, 114, 130,131] Research into conjugated polymers containing electron donor–acceptor pairs in the polymeric main chain and/or side chains has become quite attractive recently^[14, 78, 80-85] because such system exhibit tunable electronic properties and enlarged spectral absorption ranges. Alternatively, the introduction of a side-chain electron-acceptor unit—usually a conjugated species that absorbs a wavelength different from that of the conjugated polymer—can increase the breadth of the wavelengths of light absorbed. Furthermore, the photogenerated excitons can be dissociated into electrons and holes more efficiently in these types of conjugated polymer because of the internal field produced by the inherent dipole moment resulting from the

donor–acceptor molecular structure, with subsequent charge transfer to nearby n-type nanoparticles (e.g., PCBM). In previous studies, we developed a new class of conjugated polymers containing side chain–tethered conjugated acceptor moieties that not only absorb light more effectively but also exhibit enhanced charge transfer ability—two desirable properties for photovoltaics applications.^[4,89,90]

Most polythiophene derivatives are good hole-transport materials, but exhibit low electron mobility. Oxadiazole-containing polymers have been applied widely as electron transporting and hole blocking materials in organic electronic devices^[132-135] (e.g., organic LEDs) because of the strong electron withdrawing ability of the heterocycle, their good thermal and chemical properties,^[136-138] and the tenability of the charge carrier mobility of attached materials.^[139,140] Oxadiazole units have previously been incorporated as side chains on poly(phenylenevinylene) (PPV) and polyfluorene (PF) derivatives that have then been incorporated into photovoltaic cells without PCBM.^[141] The performance of these devices was improved as a result of increases in the electron mobility and rate of exciton dissociation in the photoactive layer. Furthermore, PPV derivatives featuring branched oxadiazole units within the PPV main chain have been applied as a PCBM blend to provide a photovoltaic cell exhibiting a PCE of 1.6%.^[142] In contrast, the photovoltaic behavior of oxadiazole-attached polythiophene copolymers has not been reported previously.

In this present study, we synthesized a donor–acceptor thiophene-type copolymer presenting electron-withdrawing 1,3,4-oxadiazole moieties as side chains for application in photovoltaic cells. Schemes 1 and 2 display our synthetic approach toward a thiophene monomer modified with an electron-withdrawing moiety and its subsequent polymerization.



5-2 Experimental

Materials

2,5-Dibromo-3-hexylthiophene (**M1**) and 4,4,5,5-tetramethyl-2-(thiophen-3-yl)-1,3,2-dioxaborolane were synthesized according to literature procedures.^[143-147] The synthetic routes toward monomer **2** (**M2**) and polymers **P05–P20** are presented in Schemes 1 and 2; procedures for the syntheses of their intermediates are described below. The 3M ether solution of methylmagnesium bromide was purchased from TCI. PCBM was purchased from Nano-C.

Regioregular P3HT was purchased from Rieke Metals (4002-E).

Poly(ethylenedioxythiophene)/poly(styrenesulfonate) (PEDOT/PSS) was purchased from Baytron (P VP A1 4083). All other chemicals and solvents were purchased in reagent grade from Aldrich, Acros, TCI, or Lancaster Chemical and used as received.

Measurement and Characterization

¹H and ¹³C nuclear magnetic resonance (NMR) spectra were recorded using a Varian Unity-300 NMR spectrometer. Thermogravimetric analysis (TGA) of the polythiophene derivatives was performed using a TA Instruments Q500 apparatus operated at a heating rate of 20 °C min⁻¹ under a N₂ flow. Differential scanning calorimetry (DSC) was performed using a Perkin–Elmer Pyris 7 instrument operated at a heating rate of 20 °C min⁻¹ under N₂ flow; samples were heated from 30 to 200

°C, cooled to 20 °C, and then heated again from 30 to 200 °C. Elemental analysis (EA) of the polymers was performed using a Heraeus CHN-OS Rapid instrument. UV–Vis spectra were measured using an HP 8453 diode array spectrophotometer. PL spectra were recorded using a Hitachi F-4500 luminescence spectrometer. We used a Waters chromatography unit interfaced to a Waters 2414 differential refractometer. Three 5- μm Waters styragel columns were connected in series in decreasing order of pore size (10^4 , 10^3 , and 10^2 Å); THF was the eluent and standard polystyrene samples were used for calibration. Cyclic voltammetry (CV) was performed using a BAS 100 electrochemical analyzer, operated at a potential scan rate of 50 mV s^{-1} ; the redox behavior of each polymer was investigated using a solution of 0.1 M tetrabutylammonium hexafluorophosphate ($n\text{-Bu}_4\text{NPF}_6$) in anhydrous acetonitrile as the electrolyte; the potentials were measured against a Ag/Ag^+ (0.01 M AgNO_3) reference electrode; ferrocene/ferrocenium ion (Fc/Fc^+) was used as the internal standard. The onset potentials were determined from the intersection of two tangents drawn at the rising and background currents of the cyclic voltammogram. The topographies of the polymer/PCBM films were measured through tapping-mode atomic force microscopy (AFM) using a Digital Instruments Nanoscope IIIa apparatus under ambient conditions; AFM samples were prepared by spin-coating solutions of polymer/PCBM blends in chlorobenzene onto indium tin oxide (ITO)/PEDOT

substrates, followed by annealing at 150 °C for 10 min.

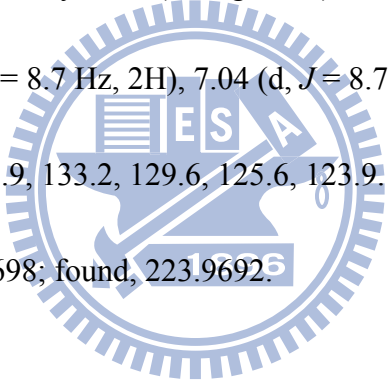
Device Fabrication and Characterization of Polymer Solar Cell

Current density–voltage (J – V) measurements were performed using devices having a sandwich structure [ITO/PEDOT:PSS/polymer:PCBM (1:1, w/w)/Ca/Al]. The ITO-coated glass substrate was pre-cleaned and treated with oxygen plasma prior to use. The polymer/PCBM layers were spin-coated from their corresponding dichlorobenzene solutions (20 mg mL⁻¹) at 1500 rpm. The thickness of the polymer/PCBM layers was ca. 100 nm. The active layers of the devices were thermally annealed at 150 °C for 10 min prior to electrode deposition. Using a base pressure of less than 1×10^{-6} torr, layers of Ca (20 nm) and Al (100 nm) were vacuum-deposited to form the anode. The effective area of one cell was 0.04 cm².

The devices were tested under simulated AM 1.5G irradiation (100 mW cm⁻²) using a Xe lamp–based Newport 66902 150-W solar simulator equipped with an AM1.5 filter as the white light source; the optical power at the sample was 100 mW cm⁻², detected using an OPHIR thermopile 71964. The J – V characteristics were measured using a Keithley 236 source-measure unit. The external quantum efficiencies (EQEs) were measured using a Keithley 236 source-measure unit coupled with an Oriel Cornerstone 130 monochromator. The light intensity at each

wavelength was calibrated using an OPHIR 71580 diode.

5-(4-Bromophenyl)-2H-tetrazole (1). A mixture of 4-bromobenzonitrile (5.00 g, 27.6 mmol), sodium azide (5.35 g, 82.3 mmol), NH₄Cl (4.40 g, 82.2 mmol), and DMF (15 mL) was heated for 4 h under N₂ in an oil bath maintained at a bath temperature of 150 °C. After cooling to room temperature, the solution was poured into 1 N HCl (150 mL) and stirred for 30 min. After filtering, the solid product was washed with water (3 × 300 mL) and dried to yield **1** (5.30 g, 85%). ¹H NMR (300 MHz, DMSO-*d*₆, ppm): 7.20 (d, *J* = 8.7 Hz, 2H), 7.04 (d, *J* = 8.7 Hz, 2H). ¹³C NMR (75 MHz, DMSO-*d*₆, ppm): 155.9, 133.2, 129.6, 125.6, 123.9. HRMS-EI (*m/z*): [M⁺] calcd. for C₇H₅BrN₄, 223.9698; found, 223.9692.



2-(4-Bromophenyl)-5-(4-*tert*-butylphenyl)-1,3,4-oxadiazole (2).

4-*tert*-Butylbenzoyl chloride (3.25 g, 16.5 mmol) was added dropwise to a solution of **1** (2.50 g, 11.1 mmol) in pyridine (30 mL) and then the mixture was heated for 6 h under N₂ in an oil bath maintained at 130 °C. After cooling to room temperature, the solution was poured into water (300 mL). The solid product was filtered off, washed with water (5 × 300 mL), and dried to yield **2** (3.25 g, 82%). ¹H NMR (300 MHz, CDCl₃, ppm): 8.04 (d, *J* = 8.7 Hz, 2H), 7.99 (d, *J* = 8.4 Hz, 2H), 7.66 (d, *J* = 8.7 Hz,

2H), 7.54 (d, $J = 8.4$, 2H), 1.34 (s, 9H). ^{13}C NMR (75 MHz, CDCl_3 , ppm): 164.2, 163.2, 155.1, 132.5, 128.6, 126.6, 126.3, 125.6, 122.6, 120.5, 34.9, 30.8. HRMS-EI (m/z): [M^+] calcd. for $\text{C}_{18}\text{H}_{17}\text{BrN}_2\text{O}$, 356.0524; found, 356.0527.

2-(4-*tert*-Butylphenyl)-5-[4-(thiophen-3-yl)phenyl]-1,3,4-oxadiazole (3). 2 M

aqueous potassium carbonate (11 mL) was added via syringe to a solution of **2** (3.00 g, 8.40 mmol), 4,4,5,5-tetramethyl-2-(thiophen-3-yl)-1,3,2-dioxaborolane (1.80 g, 8.53 mmol), and tetrakis(triphenylphosphine)palladium (2 mol%) in toluene (22 mL) in a 50-mL two-neck flask. The mixture was then stirred overnight at 90 °C under N_2 . After cooling to room temperature, the solution was washed with water and back-extracted with EtOAc. The organic layer was dried (MgSO_4) and concentrated to yield **3** (2.70 g, 90%). ^1H NMR (300 MHz, CDCl_3 , ppm): 8.17 (d, $J = 8.1$ Hz, 2H), 8.08 (d, $J = 8.1$ Hz, 2H), 7.77 (d, $J = 8.1$ Hz, 2H), 7.61–7.59 (m, 1H), 7.56 (d, $J = 8.4$ Hz, 2H), 7.48–7.43 (m, 2H), 1.38 (s, 9H). ^{13}C NMR (75 MHz, CDCl_3 , ppm): 164.6, 164.2, 155.3, 141.0, 138.8, 127.4, 126.8, 126.7, 126.2, 126.0, 124.3, 122.5, 121.7, 121.1, 35.1, 31.1. HRMS-EI (m/z): [M^+] calcd. for $\text{C}_{22}\text{H}_{20}\text{N}_2\text{OS}$, 360.1296; found, 360.1287.

2-(4-*tert*-Butylphenyl)-5-[4-(2,5-dibromothiophen-3-yl)phenyl]-1,3,4-oxadiazole

(M2). *N*-Bromosuccinimide (NBS, 2.00 g, 11.2 mmol) was added portionwise to a solution of **3** (2.00 g, 5.55 mmol) in THF (20 mL) and acetic acid (20 mL) and then the mixture was stirred and heated at 80 °C for 6 h. After cooling to room temperature, the solution was washed sequentially with water (2 × 200 mL), saturated NaHCO₃ (1 × 200 mL), and then water again (1 × 200 mL). Following extraction with EtOAc, the organic layer was dried (MgSO₄) and concentrated to yield the monomer **M2** (2.64 g, 92%). ¹H NMR (300 MHz, CDCl₃, ppm): 8.18 (d, *J* = 8.7 Hz, 2H), 8.06 (d, *J* = 8.7 Hz, 2H), 7.67 (d, *J* = 8.4 Hz, 2H), 7.55 (d, *J* = 8.4 Hz, 2H), 7.07 (s, 1H), 1.37 (s, 9H). ¹³C NMR (75 MHz, CDCl₃, ppm): 164.8, 163.9, 155.4, 140.8, 137.1, 131.3, 129.1, 127.0, 126.8, 126.0, 123.5, 121.0, 111.8, 108.7, 35.1, 31.1. HRMS-EI (*m/z*): [M⁺] calcd. for C₂₂H₁₈Br₂N₂OS, 517.9507; found, 517.9457.

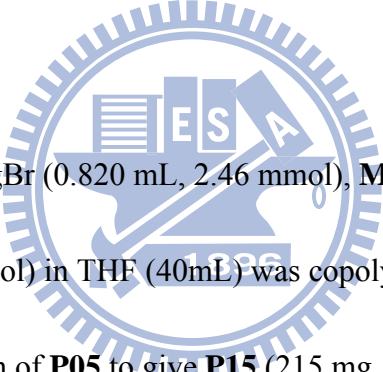
Preparation of Polythiophene Derivatives. All polymers were synthesized through Grignard metathesis polymerization in THF according to procedures similar to those described in the literature.^[143-145] The Grignard metathesis polymerizations of **M1** and **M2** are presented in Scheme 2.

Poly(3-hexylthiophene) (P3HT). CH₃MgBr (1.50 mL, 4.50 mmol) was added via syringe to a stirred solution of 2,5-dibromo-3-hexylthiophene (1.60 g, 4.50 mmol) in

freshly distilled THF (80 mL) in a three-neck 100-mL round-bottom flask. The solution was heated under reflux for 2 h and then Ni(dppp)Cl₂ (12 mg, 0.02 mmol) was added. The mixture was stirred at 95°C for 2.5h before the reaction was quenched through the addition of MeOH. The solid polymer was washed with MeOH and hexane within a Soxhlet extractor; it was then dissolved through Soxhlet extraction with CHCl₃, the solvent was evaporated, and the residue dried under vacuum to yield poly(3-hexylthiophene) (0.51 g, 61%). The weight-average molecular weights (M_w) and polydispersity (PDI) are 15.9 kg mol⁻¹ and 1.26 respectively. ¹H NMR (300 MHz, CDCl₃, ppm): 6.96 (s, 1H), 2.79 (t, 2H); 0.89–0.81, 1.43–1.15, and 1.72–1.45 (m, 11H). ¹³C NMR (75 MHz, CDCl₃, ppm): 139.8, 133.7, 130.4, 128.5, 31.9, 30.6, 29.6, 29.4, 22.7, 14.2. Anal. Calcd: C, 72.23; H, 8.49. Found: C, 72.10; H, 8.30.

P05. CH₃MgBr (0.820 mL, 2.46 mmol) was added via syringe to a stirred solution of 2,5-dibromo-3-hexylthiophene (760 mg, 2.33 mmol), **M2** (63.5 mg, 0.122 mmol), and freshly distilled THF (40 mL) in a three-neck 100-mL round-bottom flask. The solution was heated under reflux for 2 h and then Ni(dppp)Cl₂ (6 mg, 0.01 mmol) was added. The mixture was stirred at 95°C for 2.5 h and then the reaction was quenched through the addition of MeOH. The solid polymer was washed with

MeOH and hexane within a Soxhlet extractor; it was then dissolved through Soxhlet extraction with CHCl_3 , the solvent was evaporated, and the residue dried under vacuum to yield **P05** (202 mg, 46%). The M_w and PDI are 25.7 kg mol^{-1} and 1.36 respectively. $^1\text{H NMR}$ (300 MHz, CDCl_3 , ppm): 8.3–7.9 (br, 0.25H), 7.7–7.4 (m, 0.25H), 6.96 (s, 1.09H), 2.78 (br, 2.12H), 1.66–1.36 (m, 7.31H), 0.88 (s, 2.98H). $^{13}\text{C NMR}$ (75 MHz, CDCl_3 , ppm): 140.1, 133.9, 130.7, 129.3, 128.8, 128.5, 127.3, 127.0, 126.3, 31.9, 31.4, 30.7, 29.7, 29.5, 22.9, 14.4. Anal. Calcd: C, 72.30; H, 8.32; N, 0.39. Found: C, 70.15; H, 7.83; N, 0.39.



P15. A mixture of CH_3MgBr (0.820 mL, 2.46 mmol), **M1** (680 mg, 2.08 mmol), and **M2** (191 mg, 0.368 mmol) in THF (40 mL) was copolymerized using the method described for the preparation of **P05** to give **P15** (215 mg, 44%). The M_w and PDI are 19.6 kg mol^{-1} and 1.36 respectively. $^1\text{H NMR}$ (300 MHz, CDCl_3 , ppm): 8.3–7.9 (br, 0.64H), 7.7–7.4 (m, 0.65H), 6.96 (s, 1.08H), 2.78 (t, 1.75H), 1.66–1.36 (m, 7.38H), 0.89 (s, 3.1H). $^{13}\text{C NMR}$ (75 MHz, CDCl_3 , ppm): 140.1, 133.9, 130.7, 129.3, 128.8, 128.5, 127.0, 126.3, 125.5, 31.9, 31.4, 30.7, 29.7, 29.5, 22.9, 14.4. Anal. Calcd: C, 72.45; H, 7.98; N, 1.17. Found: C, 69.91; H, 7.72; N, 1.24.

P20. A mixture of CH_3MgBr (0.820 mL, 2.46 mmol), **M1** (640 mg, 1.96 mmol),

and **M2** (254 mg, 0.488 mmol) in THF (40 mL) was copolymerized using the method described for the preparation of **P05** to give **P15** (218 mg, 43%). The M_w and PDI are 13.8 kg mol^{-1} and 1.36 respectively. ^1H NMR (300 MHz, CDCl_3 , ppm): 8.3–7.9 (br, 0.66H), 7.7–7.4 (m, 0.72H), 6.96 (s, 0.75H), 2.78 (br, 1.33H), 1.66–1.36 (m, 9.7H), 0.89 (s, 1.83H). ^{13}C NMR (75 MHz, CDCl_3 , ppm): 140.1, 133.9, 130.7, 129.3, 128.8, 128.5, 127.0, 126.3, 125.5, 31.9, 31.4, 30.7, 29.7, 29.5, 22.9, 14.4. Anal. Calcd: C, 72.53; H, 7.80; N, 1.56. Found: C, 70.33; H, 7.70; N, 2.03.

5-3 Results and Discussion

Schemes 1 and 2 illustrate the synthetic routes that we followed for the preparation of the monomers and copolymers. Starting from 4-bromobenzonitrile, compounds **1** and **2** were prepared via tetrazole routes with relative high yields and simple workup procedures.^[148] The Suzuki coupling of compound **2** with 4,4,5,5-tetramethyl-2-(thiophen-3-yl)-1,3,2-dioxaborolane furnished the desired compound **3**, which we then brominated with NBS to generate the monomer **M2**. As indicated in Scheme 2, the copolymers were obtained through Grignard metathesis polymerization using various monomer **M1/M2** mixtures. The resulting copolymers **P05–P20** are soluble in common organic solvents, including toluene, THF, CHCl_3 , and chlorobenzene. We characterized the synthesized monomers and copolymers using ^1H and ^{13}C NMR spectroscopy and mass spectrometry.

In the ^1H NMR spectrum of **P15**, the peak at 6.96 ppm (CH proton of the thiophene ring) is absent, while broad peaks at 7.9–8.3, 7.4–7.6 (CH protons on the phenyl group), and 0.8–3.0 (hexyl chain and *tert*-butyl group protons) ppm confirm that the copolymer of **M1** and **M2** had formed. We confirmed that the copolymers and the self-made P3HT possessed head-to-tail (regioregular) configurations because the signal at 6.96 ppm was present in the spectra without any other peaks nearby.^[139,140] Table 1 display the actual ratio of polymers, molecular weights, degradation temperatures, and glass transition temperatures of all of our synthesized copolymers. The actual content of oxadiazole pendant side chain groups for P05, P15 and P20 as estimated from elemental analysis is 5, 16, and 26 mol% respectively. The number molecular weights (M_n) of our polymers ranged from 11.2 to 18.9 kg mol⁻¹, with polydispersity indices (PDIs) ranging from 1.24 to 1.36. Each copolymer exhibited outstanding thermal stability, with 5% weight losses temperatures (T_d) greater than 350 °C under N₂ atmosphere. The glass transition temperatures (T_g) increased from 55.8°C for the self-made P3HT to 92.1 °C for **P20**, due to the stronger interchain interactions among the copolymers.

Optical Properties

Figure 5-1(a) displays UV–Vis spectra of the polymers in THF solution (9.6×10^{-5}

M). The small peak at 304 nm was caused by the presence of conjugated 1,3,4-oxadiazole moieties that were not fully coplanar with the polythiophene chain, owing to steric hindrance. The dihedral angle between the plane of oxadiazole moiety and that of thiophene is 32.11° as determined by molecular modeling (ChemBio3D, see Appendix, Figure A5-2.). The absorption maximum wavelength of comonomer (compound 3) is 314nm which is closed to the absorption of 1,3,4-oxadiazole moieties in copolymer. The π - π^* transitions were responsible for the maximum absorptions (λ_{\max}) occurring at ca. 445 nm for P3HT and at 446 nm for **P15**. Figure 5-1(b) displays UV-Vis spectra of the polymers in the solid state with film thickness 90nm on quartz. For P3HT, the peak of the π - π^* transition had red-shifted from 445 nm in solution to 521 nm in the solid state; for **P15**, the red-shift was from 446 to 518 nm. These data indicate that efficient π stacking and intermolecular interactions occurred in the films. The vibronic absorption shoulders in the P3HT and **P05-P20** film are a manifestation of high degree of π - π stacking of thiophene planes. Introducing the 1,3,4-oxadiazole moieties to the polymer side chain, however, weakens this π - π stacking and therefore the vibronic shoulders, causing P15 to have less red-shifted shoulders than that of P3HT. The optical band gaps (E_g^{opt}) of P3HT and **P05-P20**, estimated from the onsets of the absorptions in their solid films are quite close to one another, in the range 1.89–1.91 eV as shown in the Table

2.

Figure 5-2 displays photoluminescence (PL) spectra of polymer films for self-made P3HT and copolymer P05-P20. The thickness of film is 90nm on ITO substrate. The PL spectra are recorded at an excitation wavelength of 450 nm and quenched relative to that of pure P3HT, with the degree of quenching increasing upon increasing the content of 1,3,4-oxadiazole units in the copolymer.

Electrochemical Properties

We used CV to investigate the redox properties of the copolymers and, thereby, estimate the energy levels of their highest occupied molecular orbitals (HOMOs) and lowest unoccupied molecular orbitals (LUMOs). Figure 5-3 displays the electrochemical behavior of the copolymers in solid films; Table 2 summarizes the relevant data. The 1,3,4-oxadiazole-containing copolymers **P05–P20** exhibited reversible reductions; their onset potentials (ca. 1.74–1.76 V) were slightly lower than that of the self-made P3HT (1.80 V). The CV traces of **P05–P20** feature reversible oxidations; we assign the onset potentials at 0.34–0.38 V (i.e., very close to 0.37 V) to oxidation of the self-made P3HT. From the onset potentials of the copolymers, we estimated HOMO energy levels of the self-made P3HT and **P05–P20** to be 5.17, 5.18, 5.17, and 5.14 eV, respectively, with LUMO energy levels of 3.00, 3.05, 3.04, and

3.06 eV, respectively, according to the energy level of the ferrocene reference (4.8 eV below vacuum level)^[149] the electrochemical band gaps of the self-made **P3HT** and **P05–P20** were, therefore, 2.17, 2.13, 2.13, and 2.08 eV, respectively. For the copolymers **P05–P20**, the introduction of electron-withdrawing groups on the side chains resulted in slightly lower LUMO energy levels and lower electrochemical band gaps relative to those of the self-made P3HT.

Photovoltaic Properties

Figure 5-4 displays the photocurrents of diodes having the structure ITO/PEDOT:PSS/polymer:PCBM (1:1, w/w)/Ca/Al that we illuminated under AM 1.5 G conditions (100 mW cm^{-2}), as well as the dark currents measured for self-made P3HT/PCBM and **P15/PCBM** blends. The short circuit current density (J_{sc}) increased upon increasing the content of 1,3,4-oxadiazole moieties, presumably because of enhanced light absorption at lower wavelengths. Table 3 lists the short-circuit current densities, open-circuit voltages, and PCEs of the heterojunction polymer photovoltaic cells.

The devices based on the self-made P3HT/PCBM and **P05–P15/PCBM** exhibited open circuit voltages (V_{oc}) of 0.59–0.65 V. Although these values are related to the difference between the HOMO energy level of the copolymers and the

LUMO energy level of PCBM,^[23] they are also influenced by many other factors, including solvent effects and the miscibility of copolymer and PCBM.

The short-circuit current density (J_{sc}) of the device containing the copolymer featuring 15 mol% 1,3,4-oxadiazole units (**P15**) and PCBM was 8.80 mA cm^{-2} , an improvement of 36% from the value of 6.45 mA cm^{-2} measured for the device containing self-made poly(3-hexylthiophene). The PCE of the device prepared from the self-made P3HT and PCBM was 2.05%, in agreement with values reported in the literature^[150]. Although the PCE of a device that was prepared using commercially available high-molecular-weight P3HT ($M_n = 33,000$, 198 repeating units) and PCBM was much higher i.e. 3.40% under the same processing condition as shown in Table 3, we are comparing the effect of different molecular structures on their photovoltaic devices performance at the same effective polymer chain length—the average number of repeating units in the polythiophene-oxadiazole copolymer **P15** ($M_n = 14,500$) and the self-made P3HT ($M_n = 12,600$) were 75 and 76, respectively. Nevertheless, the PCE of the **P15**/PCBM device was 2.50%, 22% higher than the PCE of 2.05% of the device featuring P3HT/PCBM as the active layer. The shape of the EQE curve of the **P15**/PCBM device in Figure 5-5(a) resembles the shape of the absorption spectrum of the active layer in Figure 5-5(b), suggesting that the absorbed photons contributed to the induced photocurrent. The EQEs of **P15**/PCBM were at least 10%

higher than those of the self-made P3HT/PCBM at wavelengths in the range 320–460 nm. Although the oxadiazole side chains provide the absorption at short wavelength region (around 304nm), they also weaken the degree of π - π stacking of thiophene planes, resulting weaker vibronic absorption shoulders. Therefore, the content of oxadiazole side chains should be optimized to provide an additional absorption region and to possess suitable degree of polymer chain ordering for better device performance. The copolymer **P05** only has a small absorption at 304nm but with decreased chain ordering, see figure A5-4 in the appendix. The copolymer **P20** provide much larger absorption at 304nm but the excess oxadiazole moieties decreased chain ordering more intensively. Therefore, the device by copolymer **P15** shows the optimal performance. Figure A5-4 shows the synchrotron grazing-incidence x-ray diffraction patterns of self-made P3HT and **P05-P15**.

Figure 5-6 displays the surface morphologies determined from AFM measurements. Samples of the self-made P3HT and the copolymer **P05-P20/PCBM** (1:1 w/w) blended films were spin-coated from their corresponding chlorobenzene solutions and then annealed at 150 °C for 10 min—i.e., conditions identical to the procedure used to fabricate the active layers of the devices. The root-mean-square (RMS) roughness of the self-made P3HT and **P05-P20** blends were 1.33, 1.531, 0.88 and 1.44 nm, respectively. The larger RMS value for the **P20/PCBM** film suggests

its significantly large phase separation. This suitable phase separation and surface roughness facilitated the improved charge transport and carrier collection efficiency, resulting in reduced charge recombination and an increased short circuit current density. From the AFM images, we assume that the homogeneous morphology of **P15** may have had a significant influence on the device performance.

5-4 Conclusions

We have used Grignard metathesis polymerization to prepare a series of thiophene-based copolymers through conjugation with electron-withdrawing 1,3,4-oxadiazole moieties in the polymer side chains. We observed PL quenching for the copolymers incorporating pendent electron-deficient 1,3,4-oxadiazole moieties on their side chains. The photocurrents of devices were enhanced in the presence of an optimal amount of the 1,3,4-oxadiazole moieties, thereby leading to improved power conversion efficiencies. The photovoltaic device based on the copolymer **P15** and PCBM exhibited a PCE of 2.50% under AM 1.5 illumination (100 mW cm^{-2}). The EQE of the device incorporating this polythiophene presenting side chain-tethered 1,3,4-oxadiazole units was greater than that of the device incorporating low-molecular-weight poly(3-hexylthiophene); as a result, its short circuit current density was also much higher.

Table 5-1. Polymerization Data and Thermal Properties of the Copolymers

Polymer	Feed ratio m:n	Actual ratio [*]	Yield (%)	M_n (10^3)	M_w (10^3)	PDI	DSC (T_g , °C)	TGA (T_d , °C)
P3HT	0:n	0:n	68	12.6	15.9	1.26	55.8	381.2
P05	0.5:9.5	0.5:9.5	65	18.9	25.7	1.36	86.9	364.7
P15	1.5:8.5	1.6:8.4	56	14.5	19.6	1.36	91.8	360.4
P20	2:8	2.6:7.4	62	11.2	13.8	1.24	92.1	355.9

^{*}: measured by elemental analysis.

Table 5-2. Optical and Redox Properties of the Copolymers

polymer	λ_{\max} (nm) solution	λ_{\max} (nm) film	E_g^{opt} (eV) ^a	E_{ox} (V)	E_{red} (V)	HOMO (eV) ^b	LUMO (eV) ^b
Self-made P3HT	445	521 (553,605)	1.91	0.37	1.80	5.17	3.00
P05	446	521 (546,601)	1.91	0.38	1.75	5.18	3.05
P15	446	518 (545,600)	1.90	0.37	1.76	5.17	3.04
P20	446	517 (545,600)	1.89	0.34	1.74	5.14	3.06

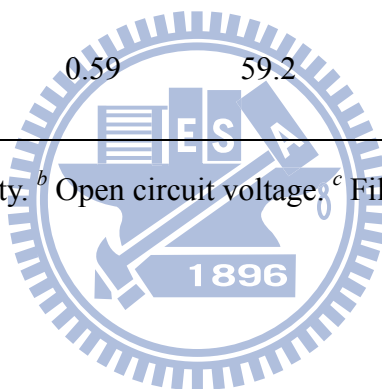
^a Estimated from the onset wavelength absorptions of the solid films. ^b Calculated from the corresponding onset potentials.

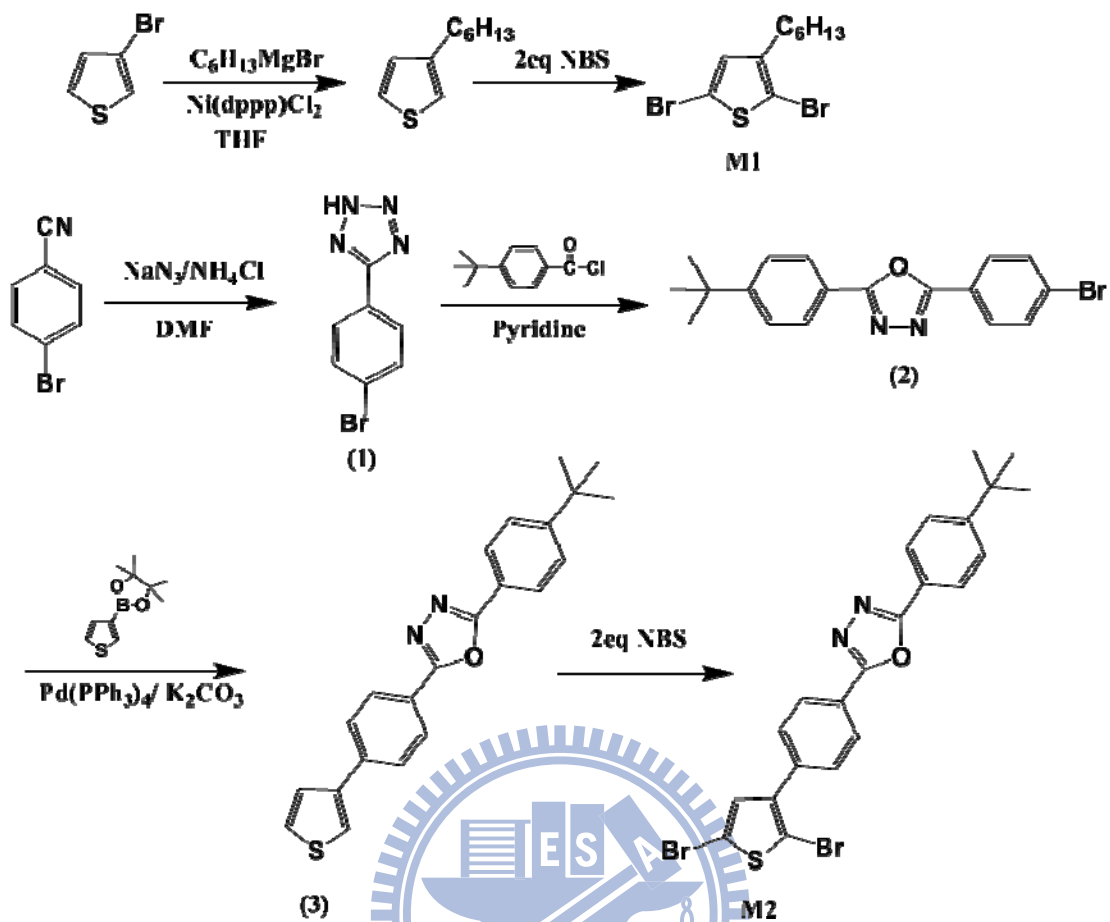
Table 5-3. Photovoltaic Properties of Polymer Photovoltaic Cells Incorporating

Blends (1:1, w/w) of P3HT/PCBM and **P05–P20**/PCBM.

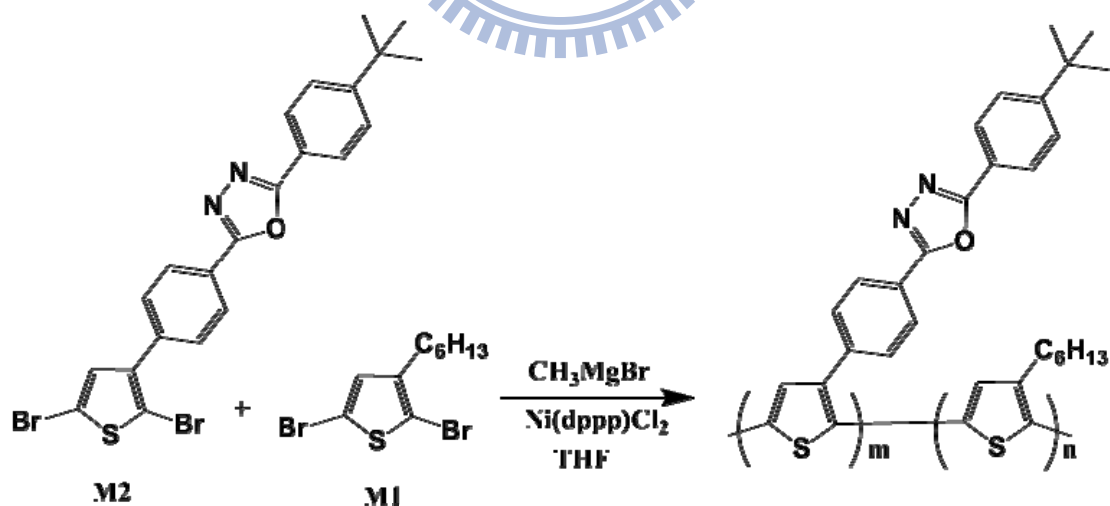
Polymer	J_{sc}^a (mA cm ⁻²)	V_{oc}^b (V)	FF ^c (%)	η^d (%)
Self-made				
P3HT (Mn=12,600)	6.45	0.63	50.0	2.05
P05	7.40	0.59	40.7	1.79
P15	8.80	0.65	43.8	2.50
P20	3.39	0.60	40.8	0.83
Commercial				
P3HT (Mn=33,000)	9.79	0.59	59.2	3.42

^a Short-circuit current density. ^b Open circuit voltage. ^c Fill factor. ^d Power conversion efficiency.





Scheme 5-1: Synthetic Routes Toward M1 and M2.



Scheme 5-2: Synthetic Route Toward the Copolymers.

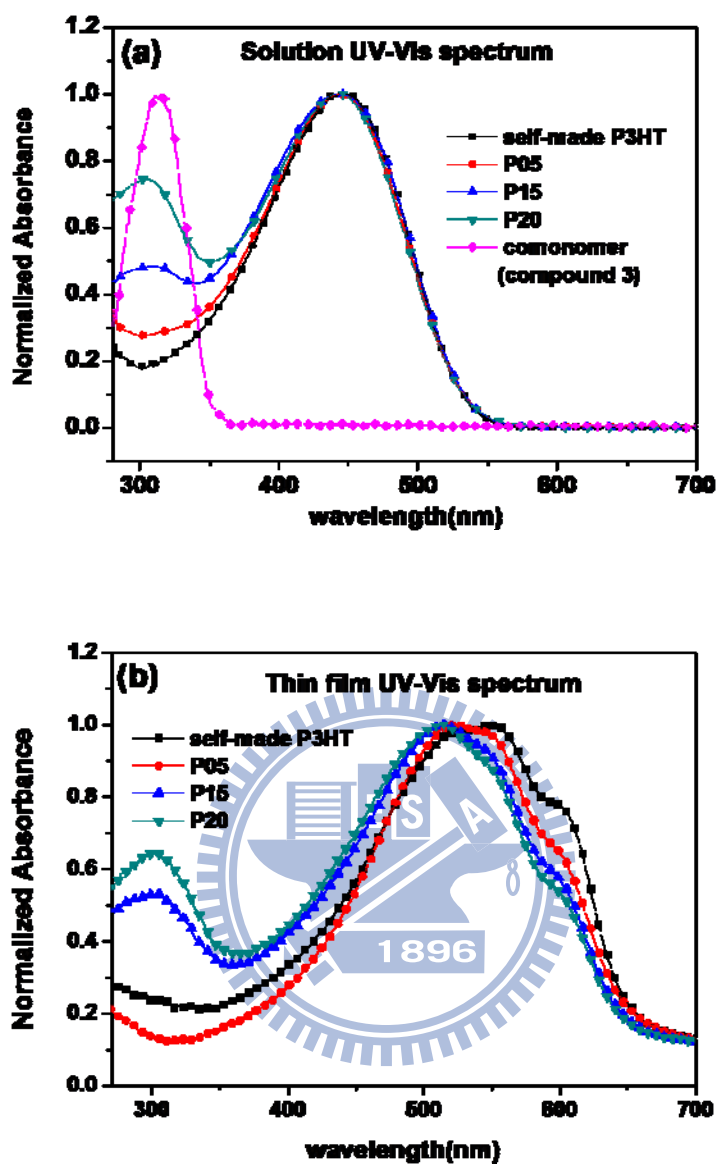


Figure 5-1. Normalized optical absorption spectra of the self-made P3HT, the copolymers **P05-P20** and comonomer (compound 3) in (a) THF solution (9.6×10^{-5} M) and (b) self-made P3HT and the copolymers **P05-P20** as thin films (the thickness of film is 90nm on quartz.)

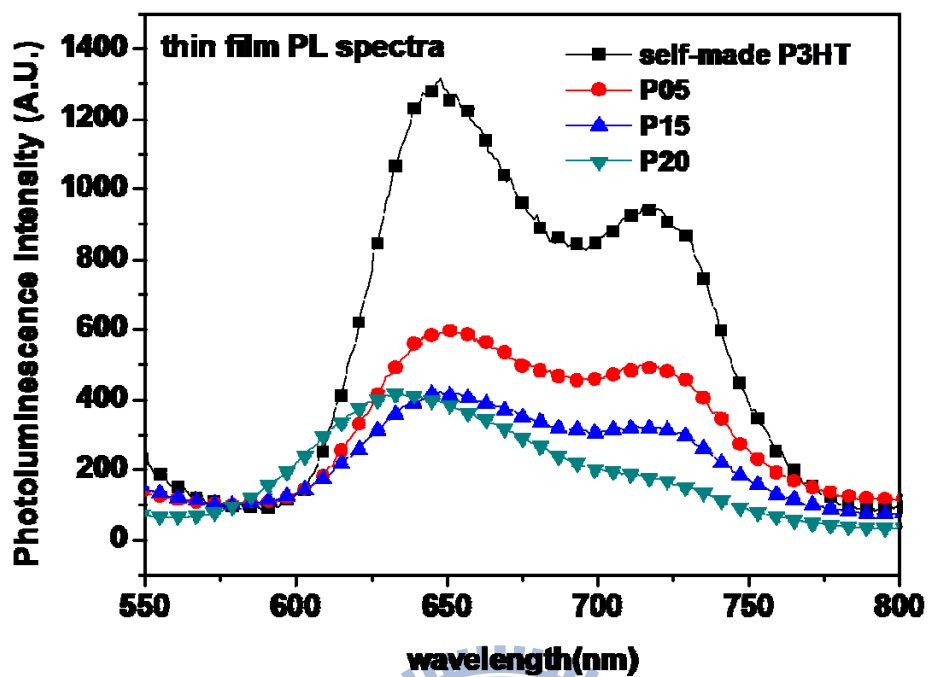


Figure 5-2: PL spectra of films of the self-made P3HT and the copolymers **P05**, **P15**, and **P20**, recorded at an excitation wavelength of 450 nm. The thickness of film is 90nm on ITO substrate.

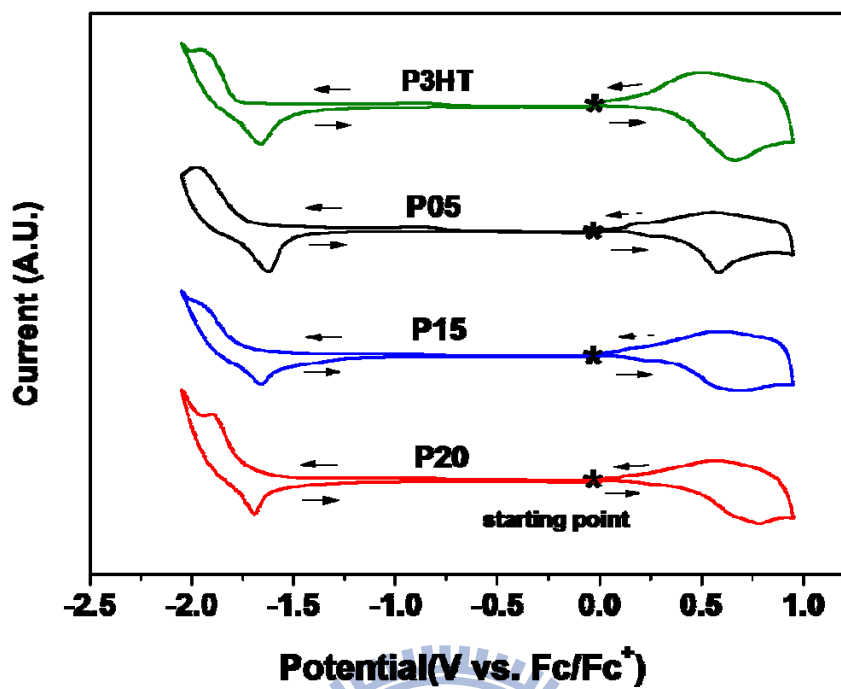


Figure 5-3: Cyclic voltammograms of films of the self-made P3HT and the copolymers **P05**, **P15**, and **P20**, recorded at a scan rate of 50 mV/s.

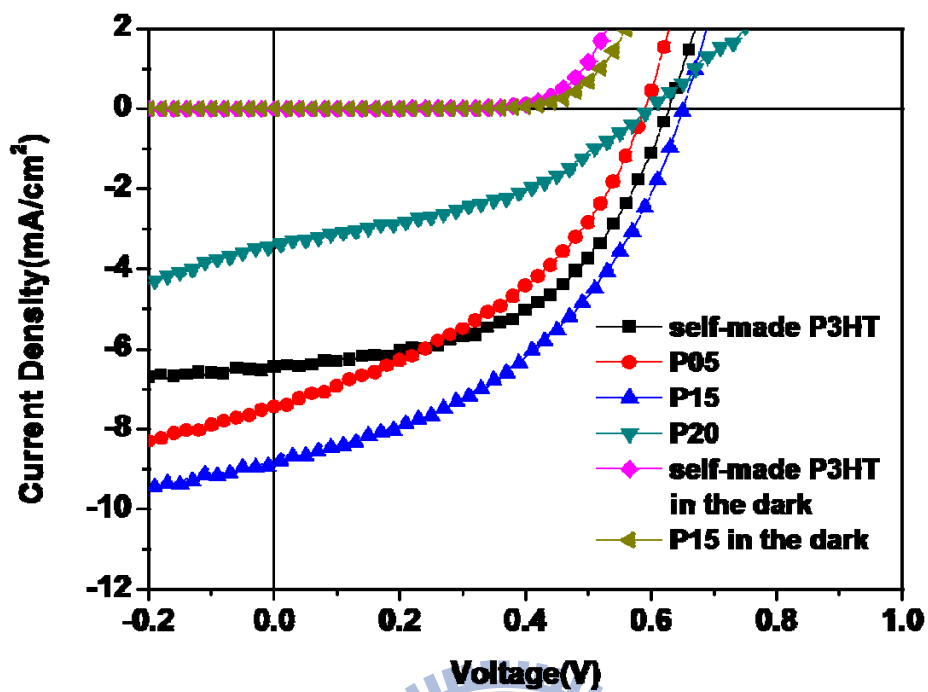


Figure 5-4: Current density–voltage characteristics of illuminated (AM 1.5G, 100 mW cm^{-2}) polymer photovoltaic cells incorporating PCBM blends of the self-made P3HT and the copolymers **P05**, **P15** and **P20**.

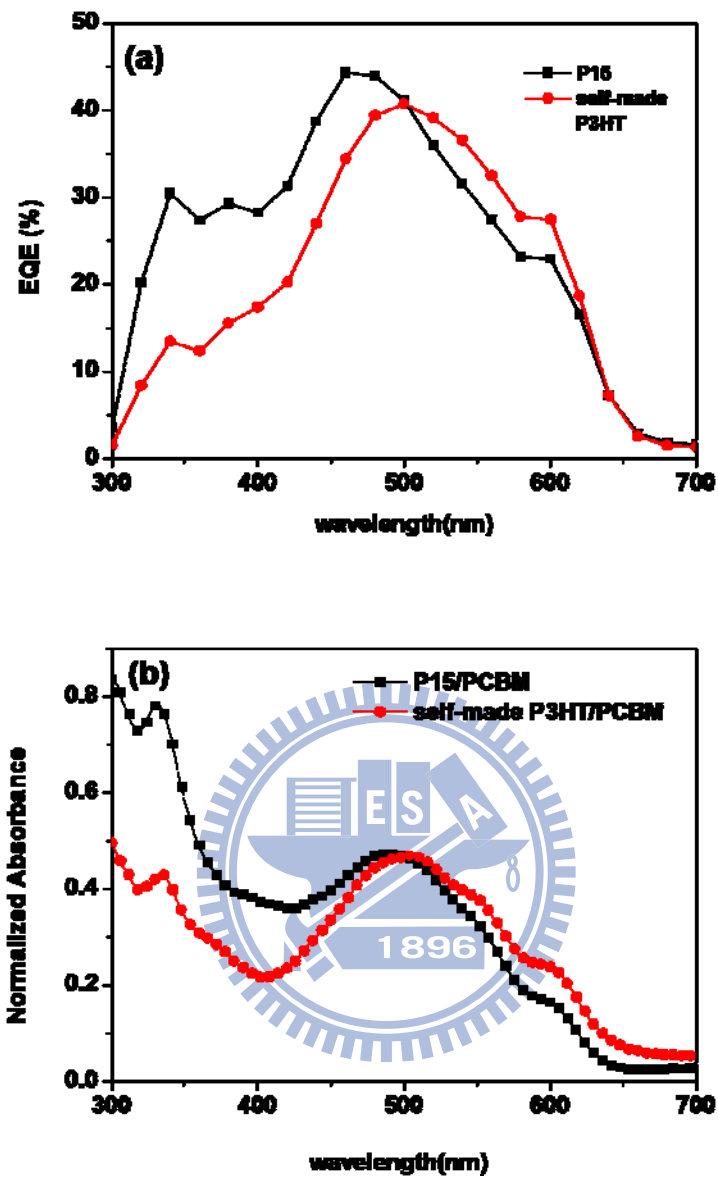


Figure 5-5: (a) EQEs of solar cells incorporating copolymer **P15/PCBM** and the self-made P3HT/PCBM blends. (b) Absorption spectra of the copolymer **P15/PCBM** and the self-made P3HT/PCBM at blend ratios of 1:1.

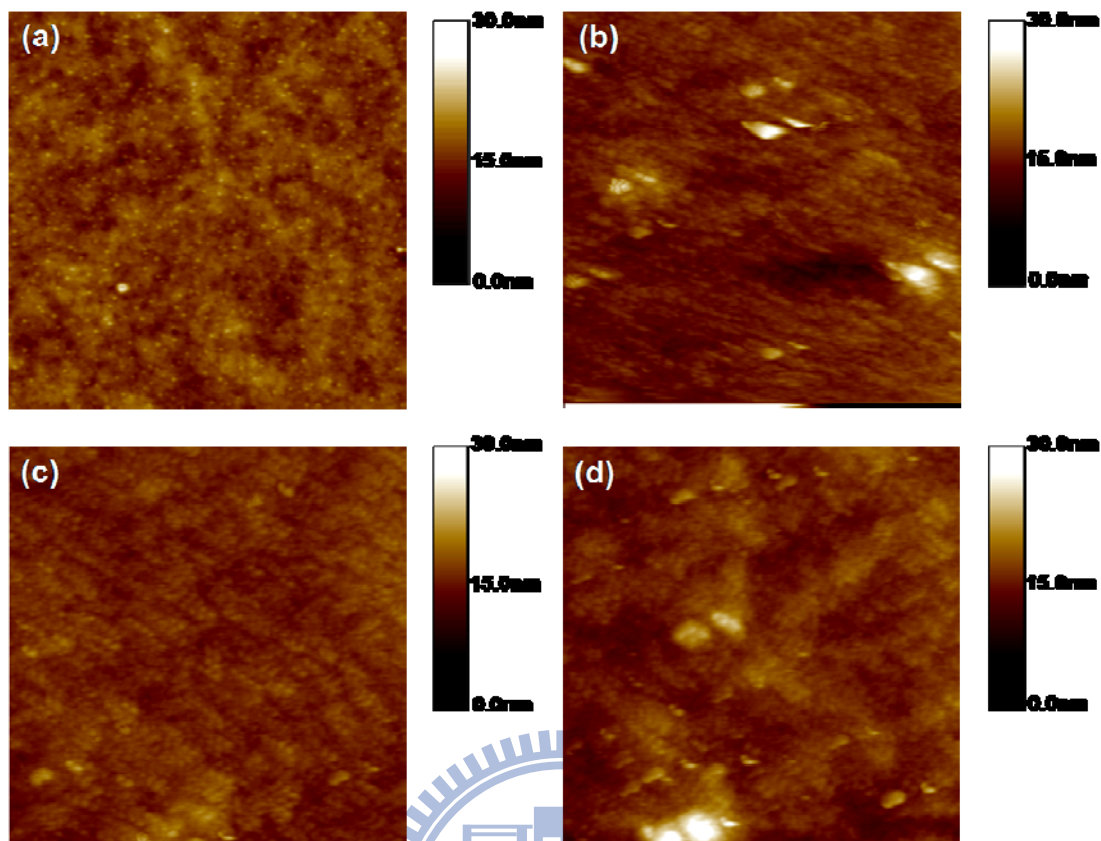
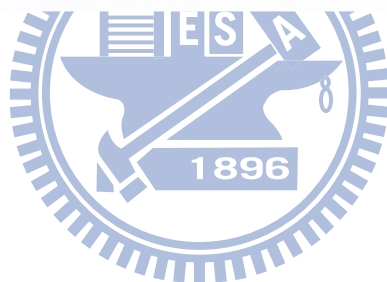
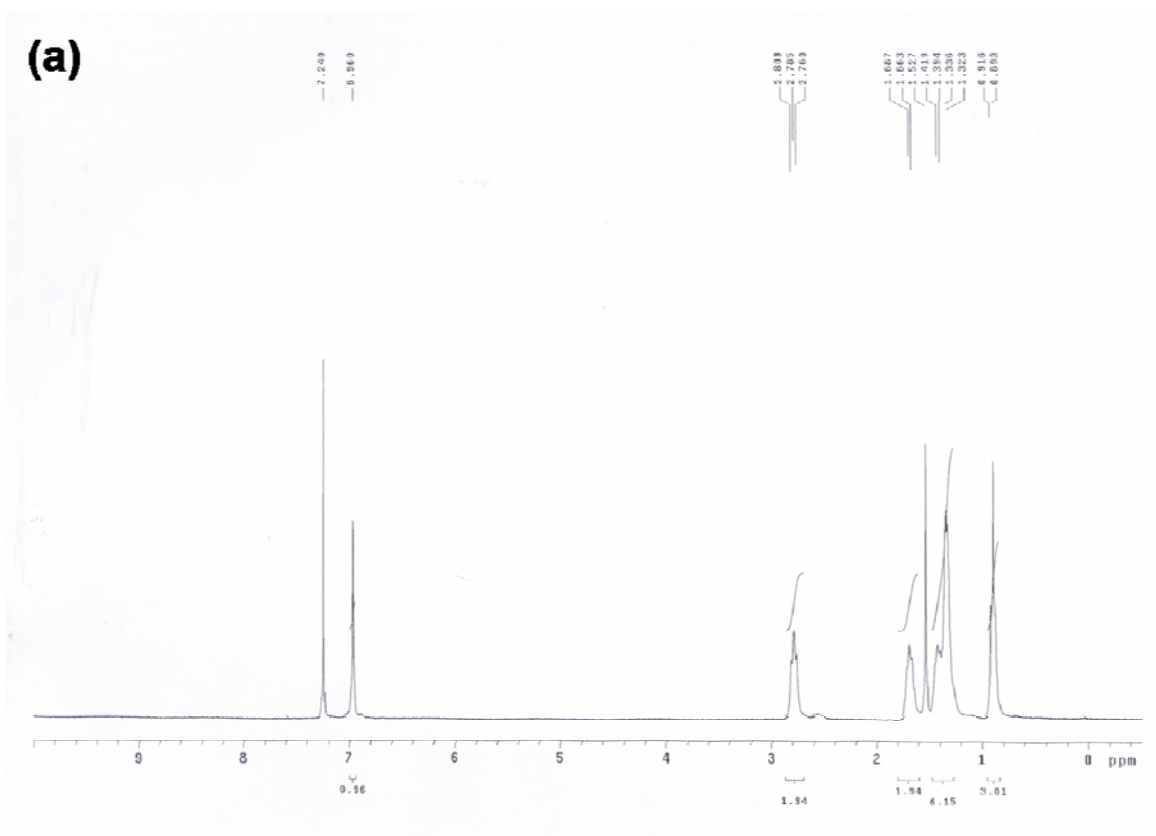
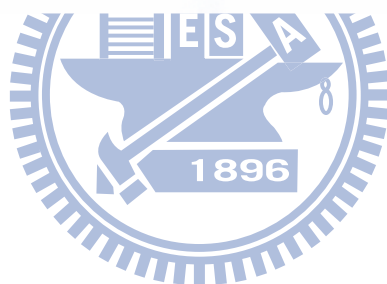
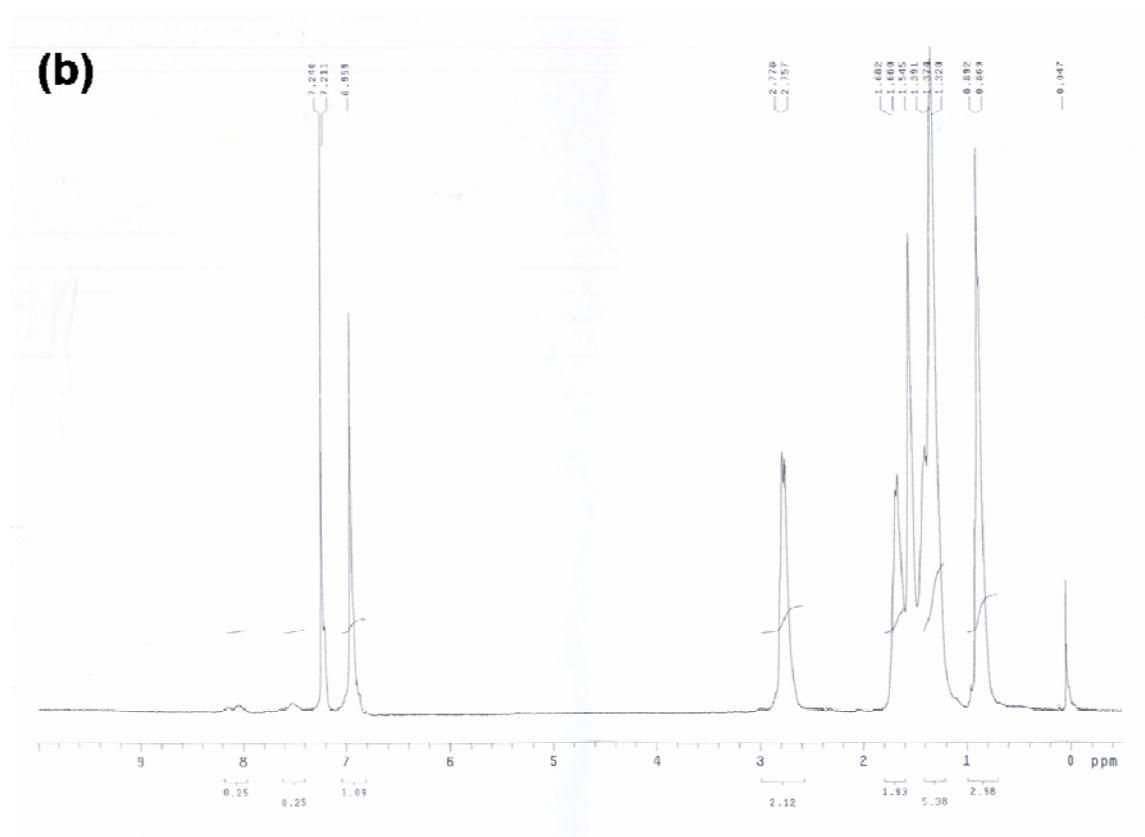
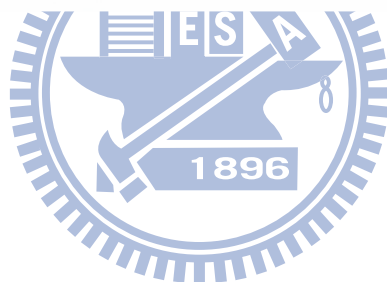
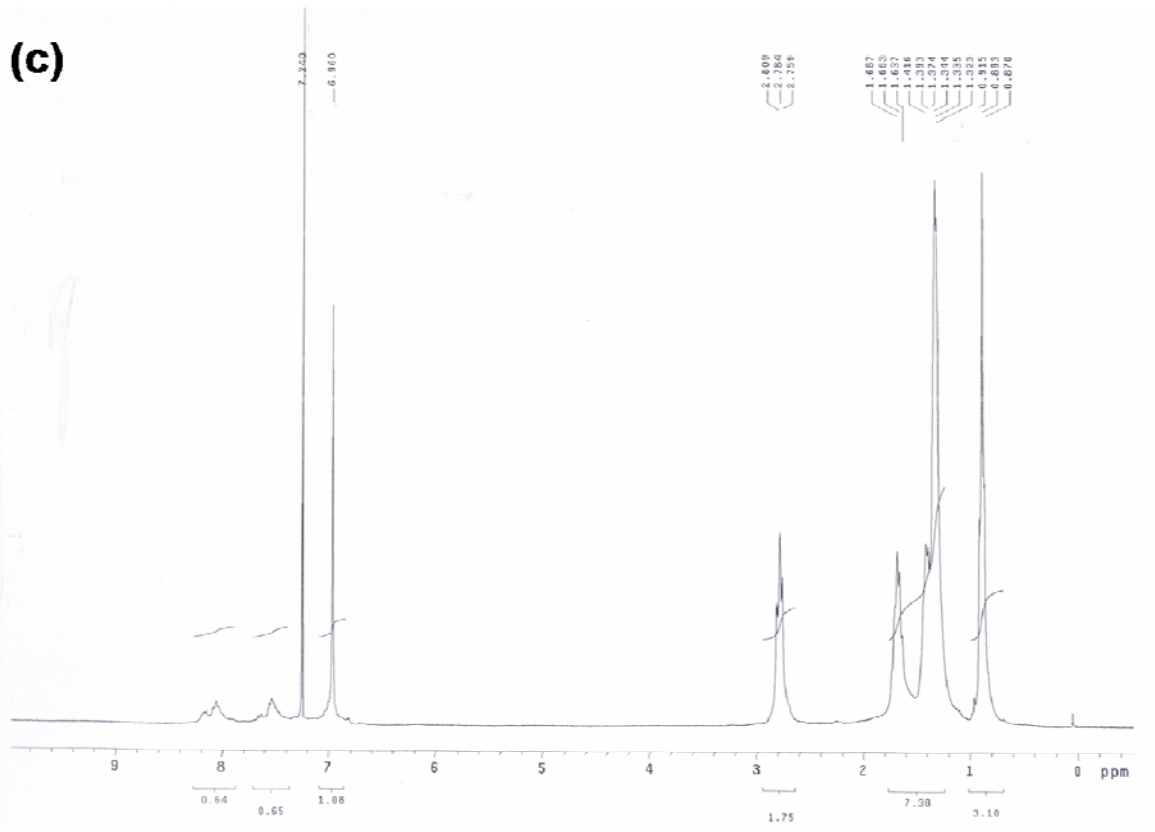


Figure 5-6: Topographic AFM images of films of PCBM blends (1:1, w/w) with (a) the self-made P3HT and (b–d) the copolymers (b) **P05**, (c) **P15**, and (d) **P20**. Image size: $2.5\ \mu\text{m} \times 2.5\ \mu\text{m}$.







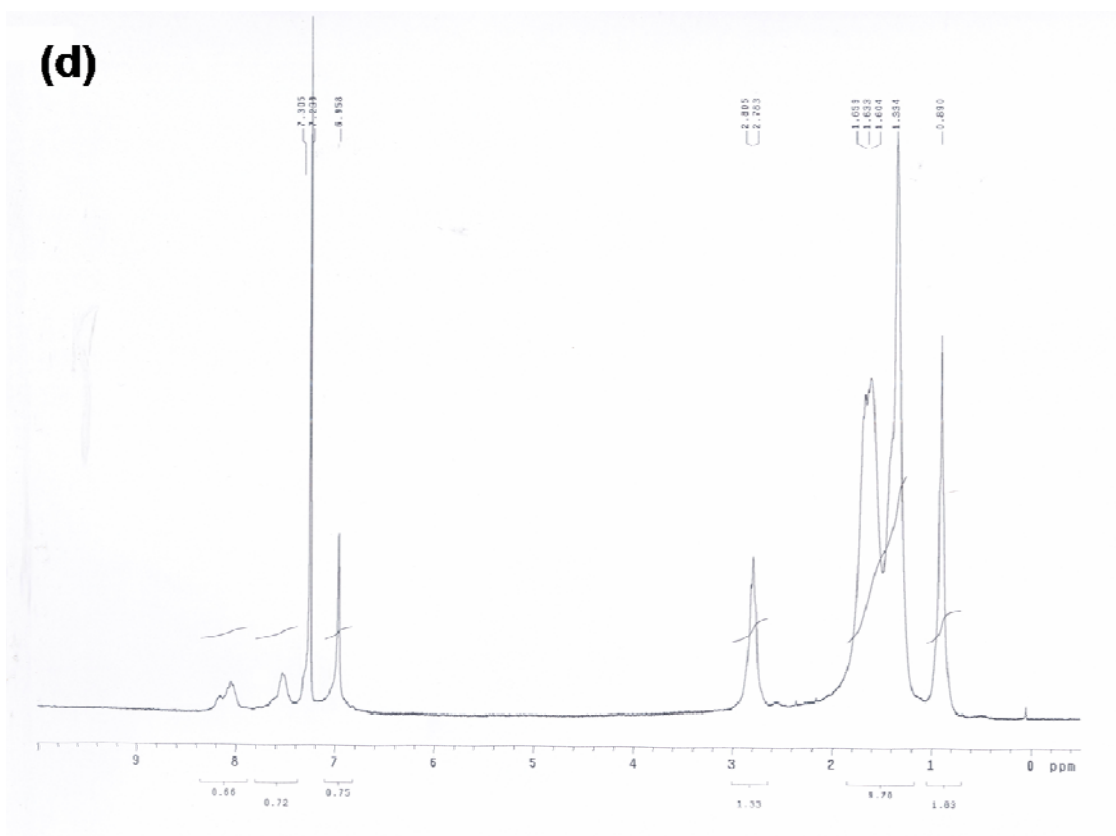


Figure A5-1 display the ^1H NMR spectra of self-made P3HT and copolymer **P05-P20**. (a) self-made P3HT, (b) P05, (c) P15, (d) P20.

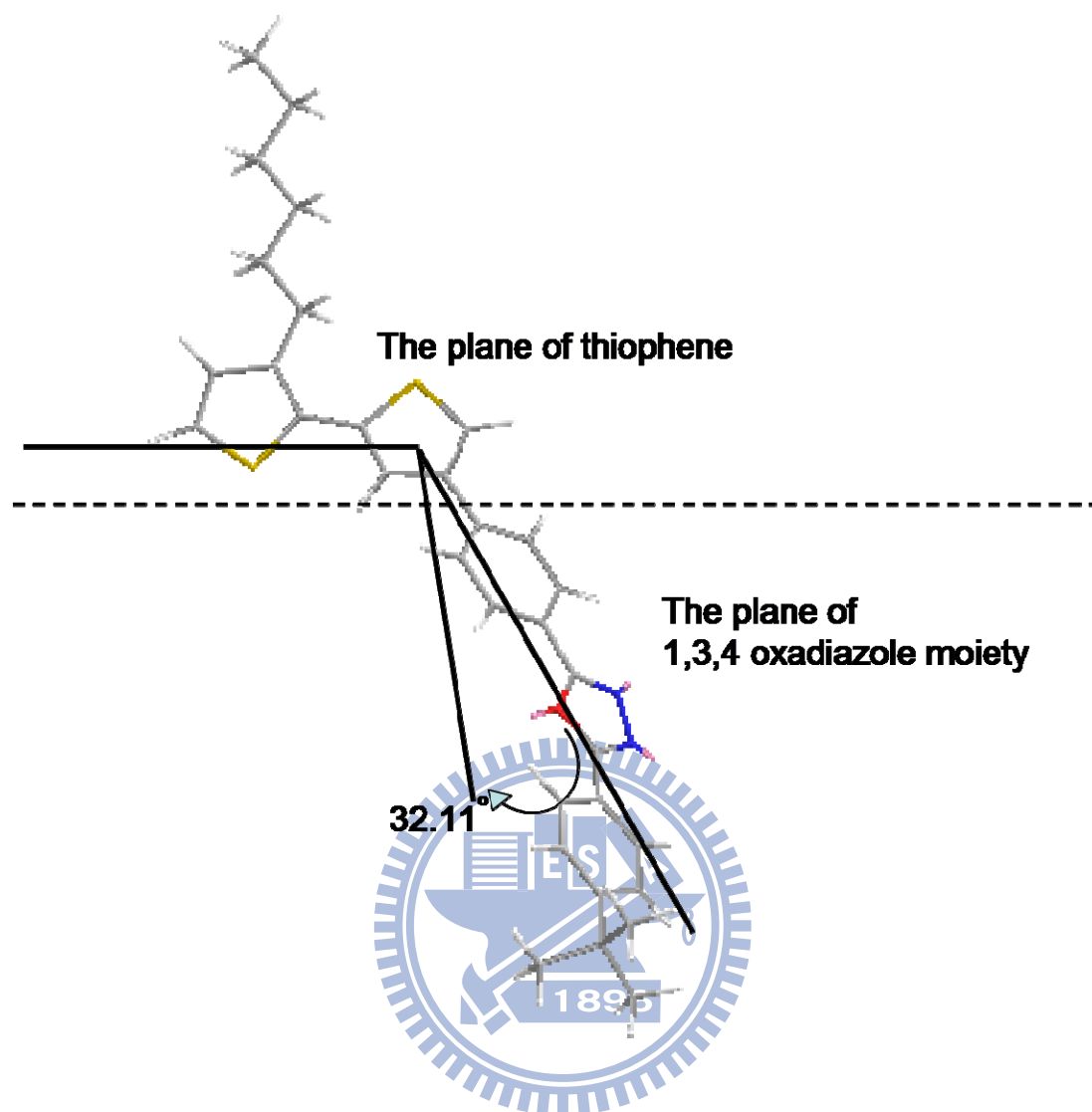


Figure A5-2. shows the dihedral angel between the plane of thiophene and the plane of 1,3,4-oxadiazole moiety simulated from the ChemBio3D Ultra software. The dihedral angel between the polymeric main chain and the 1,3,4-oxadiazole moiety is 32.11°.

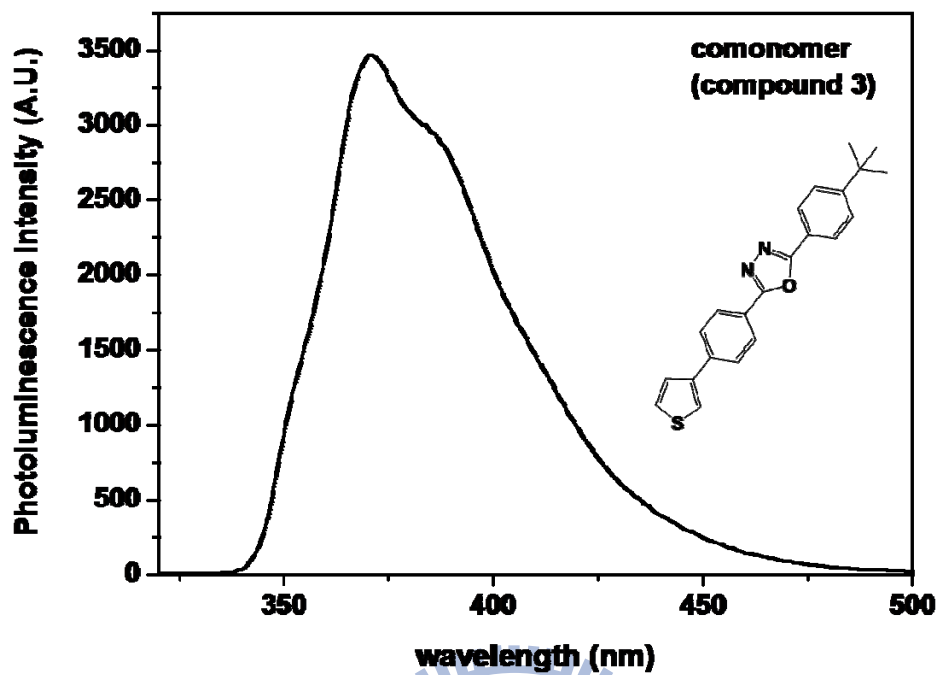


Figure A5-3. The Photoluminescence of the comonomer (compound 3) in THF solution (9.6×10^{-5} M) recorded at an excitation wavelength of 310 nm.



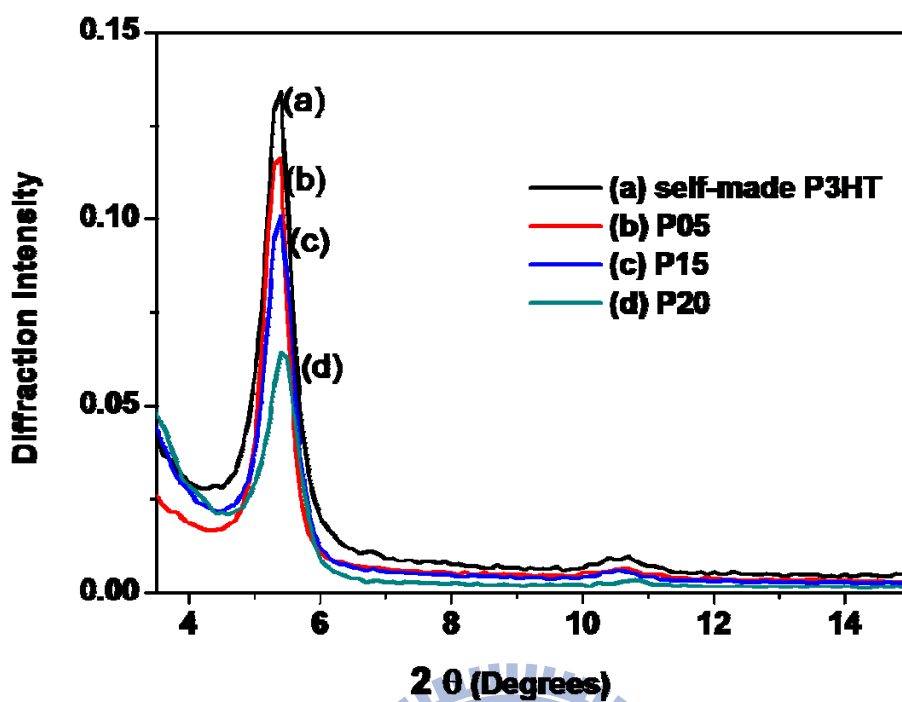


Figure A5-4. Synchrotron Grazing-incidence XRD diffraction diagrams of self-made P3HT and copolymer P05-P20 as-cast films (100nm on ITO substrate), identically annealed at 150°C for 10 min. The decrease at $2\theta \sim 5^\circ$ (interchain distance of interdigitated alkyl chain in Polythiophene backbone) is observed obviously for P20. That means ordering of polymer chain is decreased.

Chapter 6: Conclusions

We have used the melt-assisted wetting of porous alumina templates to fabricate vertical nanorod arrays of P3HT and PCBM having core-shell nanostructures for application in polymer solar cells. The C-AFM current images revealed the difference of charge transport behavior of the core and shell moieties. As a result of superior carrier transport, the internal and external quantum efficiencies of these core/shell nanorod inverted solar cells were both higher than those of the corresponding conventional inverted BHJ device. The optimized nanorod array structure had a high hole mobility that was over one order magnitude greater than that of the conventional BHJ structure; the corresponding device displayed more efficient carrier transport, which contributed to a higher short-circuit current density and PCE, relative to those of the conventional device. Furthermore, this approach is also applied for TiO₂ nanorod/P3HT rod array device for solar cell application.

The development of novel materials for solar cell application, we have used Grignard metathesis polymerization to prepare a series of thiophene-based copolymers through conjugation with electron-withdrawing 1,3,4-oxadiazole moieties in the polymer side chains. The photocurrents of devices were enhanced in the presence of an optimal amount of the 1,3,4-oxadiazole moieties, thereby leading to improved power conversion efficiencies. The photovoltaic device based on the copolymer **P15** and PCBM exhibited a PCE of 2.50% under AM 1.5 illumination (100 mW cm⁻²). The EQE of the device incorporating this polythiophene presenting side chain-tethered 1,3,4-oxadiazole units was greater than that of the device incorporating low-molecular-weight poly(3-hexylthiophene); as a result, its short circuit current density was also much higher.

Reference

- [1] G. Yu, J. Gao, J. C. Hummelen, F. Wudl, and A. J. Heeger, *Science* **1995**, 270, 1789.
- [2] K. M. Coakley and M. D. McGehee, *Chem. Mater.* **2004**, 16, 4533.
- [3] Y. Y. Lin, D. Y. Wang, H. C. Yen, H. L. Chen, C. C. Chen, C. M. Chen, C. Y. Tang and C. W. Chen, *Nanotechnology* **2009**, 20, 405207.
- [4] Y. T. Chang, S. L. Hsu, M. H. Su, and K. H. Wei, *Adv. Mater.* **2009**, 21, 2093.
- [5] C. Dridi, V. Barlier, H. Chaabane, J. Davenas and H. B. Ouada, *Nanotechnology* **2008**, 19, 375201.
- [6] J. Peet, M. L. Senatore, A. J. Heeger, and G. C. Bazan, *Adv. Mater.* **2009**, 21, 1521.
- [7] C. C. Oey, A. B. Djuricic, H. Wang, K. K. Y. Man, W. K. Chan, M. H. Xie, Y. H. Leung, A. Pandey, J. M. Nunzi and P. C. Chui, *Nanotechnology* **2006**, 17, 706.
- [8] A. Kumar, G. Li, Z. Hong and Y. Yang, *Nanotechnology* **2009**, 20, 165202.
- [9] A. Hadipour, B. D. Boer, and P. W. M. Blom, *Adv. Funct. Mater.* **2008**, 18, 169.
- [10] M. Y. Chiu, U. S. Jeng, C. H. Su, K. S. Liang, and K. H. Wei, *Adv. Mater.* **2008**, 20, 2573.
- [11] L. M. Chen, Z. Hong, G. Li, and Y. Yang, *Adv. Mater.* **2009**, 21, 1434.
- [12] G. K. Mor, K. Shankar, M. Paulose, O. K. Varghese, and C. A. Grimes, *Appl. Phys. Lett.* **2007**, 91, 152111.
- [13] H.-Y. Chen, J. Hou¹, S. Zhang, Y. Liang, G. Yang, Y. Yang, L. Yu, Y. Wu and G. Li, *Nat. Photonics* **2009**, 3, 649.
- [14] C. J. Brabec, N. S. Sariciftci, and J. C. Hummelen, *Adv. Funct. Mater.* **2001**, 11, 15.
- [15] R. Koeppe, and N. S. Sariciftci, *Photochem. Photobiol. Sci.* **2006**, 5, 1122.
- [16] Photoinduced Electron Transfer (Eds.: M. A. Fox, M. Chanon), Elsevier,

Amsterdam, **1988**.

- [17] H. Hoppe, N. S. Sariciftci, *J. Mater. Res.* **2004**, 19, 1924.
- [18] C. J. Brabec, A. Cravino, D. Meissner, N. S. Sariciftci, T. Fromherz, M. T. Rispens, L. Sanchez, and J. C. Hummelen, *Adv. Funct. Mater.* **2001**, 11, 374.
- [19] A. Gadisa, M. Svensson, M. R. Andersson, and O. Inganäs, *Appl. Phys. Lett.* **2004**, 84, 1609.
- [20] J.-L. Brédas, D. Beljonne, V. Coropceanu, and J. Cornil, *Chem. Rev.*, **2004**, 104, 4971.
- [21] C. J. Brabec, C. Winder, N. S. Sariciftci, J. C. Hummelen, A. Dhanabalan, P. A. van Hal, and R. A. J. Janssen, *Adv. Funct. Mater.* **2002**, 12, 709.
- [22] L. J. A. Koster, V. D. Mihailetchi, and P. W. M. Blom, *Appl. Phys. Lett.* **2006**, 88, 093511.
- [23] M. C. Scharber, D. Mühlbacher, M. Koppe, P. Denk, C. Waldauf, A. J. Heeger, and C. J. Brabec, *Adv. Mater.* **2006**, 18, 789.
- [24] H. Hoppe, and N. S. Sariciftci, *J. Mater. Chem.* **2004**, 19, 1924.
- [25] J. Rostalski and D. Meissner, *Sol. Energy Mater. Sol. Cells* **2000**, 61, 87.
- [26] E. G. Wang, L. Wang, L. F. Lan, C. Luo, W. L. Zhuang, J. B. Peng, and Y. Cao, *Appl. Phys. Lett.* **2008**, 92, 033307.
- [27] N. Blouin, A. Michaud, D. Gendron, S. Wakim, E. Blair, R. Plesu, M. BelletTte, G. Durocher, Y. Tao, and M. Leclerc, *J. Am. Chem. Soc.* **2008**, 130, 732.
- [28] S. H. Park, A. Roy, S. Beaupre, S. Cho, N. Coates, J. S. Moon, D. Moses, M. Leclerc, K. Lee, A. J. Heeger, *Nat. Photonics* **2009**, 3, 297.
- [29] L. Huo, J. Hou, S. Zhang, H.-Y. Chen, and Y. Yang, *Angew. Chem. Int. Ed.* **2010**, 49, 1500.
- [30] Y. Liang, Z. Xu, J. Xia, S.-T. Tsai, Y. Wu, G. Li, C. Ray, and L. Yu, *Adv. Mater.* **2010**, 22, 1.

- [31] Y. Liang, D. Feng, Y. Wu, S.-T. Tsai, G. Li, C. Ray, L. Yu, *J. Am. Chem. Soc.* **2009**, 131, 7792.
- [32] H. Hoop, and N. S. Sariciftci, *Adv. Polym. Sci.* **2008**, 214, 1.
- [33] B. C. Thompson and J. M. J. Frechet, *Angew. Chem. Int. Ed.* **2008**, 47, 58.
- [34] J. Peet, A. J. Heeger, and G. C. Bazan, *Acc. Chem. Res.* **2009**, 42, 1700.
- [35] G. Dennler, M. C. Scharber, and C. J. Brabec, *Adv. Mater.* **2009**, 21, 1323.
- [36] S. Gunes, H. Neugebauer, and N. S. Sariciftci, *Chem. Rev.* **2007**, 107, 1324.
- [37] R. A. Janssen, J. C. Hummelen, and N. S. Sariciftci, *MRS Bull.* **2005**, 30, 33.
- [38] G. Zhao, Y. He, Z. Xu, J. Hou, M. Zhang, J. Min, H.-Y. Chen, M. Ye, Z. Hong, Y. Yang, and Y. Li, *Adv. Funct. Mater.* **2010**, 20, 1480.
- [39] S. A. Backer, K. Sivula, D. F. Kavulak, and J. M. J. Frechet, *Chem. Mater.* **2007**, 19, 2927.
- [40] W. U. Huynh, J. J. Dittmer, and A. P. Alivisatos, *Science* **2002**, 295, 2425.
- [41] B. Sun, E. Marx, and N. C. Greenham, *Nano Lett.* **2003**, 3, 961.
- [42] B. Sun, H. J. Snaith, A. S. Dhoot, S. Westenhoff, and N. C. Greenham, *J. Appl. Phys.* **2005**, 97, 014 941.
- [43] C. Y. Kwong, A. B. Djurišić, P. C. Chui, K. W. Cheng, and W. K. Chan, *Chem. Phys. Lett.* **2004**, 384, 372.
- [44] W. J. E. Beek, M. M. Wienk, and R. A. J. Janssen, *Adv. Mater.* **2004**, 16, 1009.
- [45] W. J. E. Beek, M. M. Wienk, M. Kemerink, X. Yang, and R. A. J. Janssen, *J. Phys. Chem. B* **2005**, 109, 9505.
- [46] S. A. McDonald, G. Konstantatos, S. Zhang, P. W. Cyr, E. J. D. Klem, L. Levina, and E. H. Sargent, *Nat. Mater.* **2005**, 4, 138.
- [47] A. A. R. Watt, D. Blake, J. H. Warner, E. A. Thomsen, E. L. Tavenner, H. Rubinsztein-Dunlop, and P. Meredith, *J. Phys. D* **2005**, 38, 2006.
- [48] D. Qi, M. Fischbein, M. Drndic, and S. Šelmic, *Appl. Phys. Lett.* **2005**, 86, 093

103.

- [49] K. R. Choudhury, Y. Sahoo, T. Y. Ohulchansky, and P. N. Prasad, *Appl. Phys. Lett.* **2005**, 87, 073 110.
- [50] E. Arici, H. Hoppe, F. Schäffler, D. Meissner, M. A. Malik, and N. S. Sariciftci, *Appl. Phys. A* **2004**, 79, 59.
- [51] K. Coakley, and M. D. McGehee, *Appl. Phys. Lett.* **2003**, 83, 3380.
- [52] K. Coakley, Y. Liu, M. D. McGehee, K. L. Frindell, and G. D. Stucky, *Adv. Funct. Mater.* **2003**, 13, 301.
- [53] P. Ravirajan, S. A. Haque, J. R. Durrant, D. D. C. Bradley, and J. Nelson, *Adv. Funct. Mater.* **2005**, 15, 609.
- [54] G. P. Bartholomew, and A. J. Heeger, *Adv. Funct. Mater.* **2005**, 15, 677.
- [55] P. Ravirajan, D. D. C. Bradley, J. Nelson, S. A. Haque, J. R. Durrant, H. J. P. Smit, and J. M. Kroon, *Appl. Phys. Lett.* **2005**, 86, 143 101.
- [56] H. Wang, C. C. Oey, A. B. Djurišić, M. H. Xie, Y. H. Leung, K. K. Y. Man, W. K. Chan, A. Pandey, J.-M. Nunzi, and P. C. Chui, *Appl. Phys. Lett.* **2005**, 87, 023 507.
- [57] D. O Carroll, I. Lieberwirth, and G. Redmond, *small* **2007**, 3, 1178.
- [58] S. A. L. Weber, N. Haberkorn, P. Theato, and R. d. Berger, *Nano Lett.* **2010**, 10, 1194.
- [59] J. S. Kim, Y. Park, D. Y. Lee, J. H. Lee, J. H. Park, J. K. Kim, and K. Cho, *Adv. Funct. Mater.* **2010**, 20, 540.
- [60] F. Heslot, A. M. Cazabat, P. Levinson, and N. Fraysse, *Phys. Rev. Lett.* **1990**, 65, 599.
- [61] M. Zhang, P. Dobriyal, J.-T. Chen, and T. P. Russell, *Nano Lett.* **2006**, 6, 1075.
- [62] M. P. de Jong, L. J. V. Ijzendoorn, and M. J. A. de Voigt, *Appl. Phys. Lett.* **2006**, 77, 2255.

- [63] K. W. Wong, H. L. Yip, Y. Luo, K. Y. Wong, and W. M. Lau, *Appl. Phys. Lett.* **2006**, 80, 2788.
- [64] C. Waldauf, M. Morana, P. Denk, P. Schilinsky, K. Coakley, S. A. Choulis, and C. J. Brabec *Appl. Phys. Lett.* **2006**, 89, 233517.
- [65] M. S. White, D. C. Olson, S. E. Shaheen, N. Kopidakis, and D. S. Ginley *Appl. Phys. Lett.* **2006**, 89, 143517.
- [66] S. K. Hau, H. L. Yip, H. Ma, and Alex K.-Y. Jen *Appl. Phys. Lett.* **2006**, 93, 233304.
- [67] R. Steim, S. A. Choulis, P. Schilinsky, and C. J. Brabec *Appl. Phys. Lett.* **2006**, 92, 093303.
- [68] A. K. K. Kyaw, X. W. Sun, C. Y. Jiang, G. Q. Lo, D. W. Zhao, and D. L. Kwong *Appl. Phys. Lett.* **2008**, 93, 221107.
- [69] H. Schmidt, H. Flügge, T. Winkler, T. Bülow, T. Riedl, and W. Kowalsky *Appl. Phys. Lett.* **2009**, 94, 243302.
- [70] H. H. Liao, L. M. Chen, Z. Xu, G. Li, and Y. Yang *Appl. Phys. Lett.* **2008**, 92, 173303.
- [71] L.-W. Chong, Y.-N. Chou, Y.-L. Lee, T.-C. Wena, T.-F. Guo, *Org. Electron.* **2009**, 10, 1141.
- [72] S. K. Hau, H.-L. Yip, O. Acton, N. S. Baek, H. Ma and A. K.-Y. Jen, *J. Mater. Chem.*, **2008**, 18, 5113.
- [73] F. Yang, M. Stheim, and S. R. Forrest, *Nat. Mater.* **2005**, 4, 37.
- [74] S. S. Kim, J. Jo, C. Chun, J. C. Hong, and D.-Y. Kim, *J. Photochem. Photobiol. A: Chem.* **2007**, 188, 364.
- [75] S. M. Lindner, S. Huttner, A. Chiche, M. Thelakkat, and G. Krausch, *Angew. Chem. Int. Ed.* **2006**, 45, 3364.
- [76] R. Otero, D. Eciija, G. Fernandez, J. M. Gallego, L. Sanchez, N. Martin, and R.

- Miranda, *Nano Lett.* **2007**, 7, 2602.
- [77] F. A. Castro, H. Benmansour, C. F. O. Graeff, F. Nuesch, E. Tutis, R. Hany, *Chem. Mater.* **2006**, 18, 5504.
- [78] L. J. Huo, Z. Tan, X. Wang, Y. Zhou, M. F. Han, and Y. F. Li, *J. Polym. Sci. Part A: Polym. Chem.* **2008**, 46, 4038.
- [79] A. C. Arias, J. D. MacKenzie, I. McCulloch, J. Rivnay and A. Salleo, *Chem. Rev.* **2010**, 110, 3.
- [80] Z. Bao, Z. Peng, M. E. Galvin, and E. A. Chandross, *Chem. Mater.* **1998**, 10, 1201.
- [81] Q. Peng, J. Xu, and W. Zheng, *J. Polym. Sci. Part A: Polym. Chem.* **2009**, 47, 3399.
- [82] M.-H. Lai, C.-C. Chueh, W.-C. Chen, J.-L. Wu, F.-C. Chen, *J. Polym. Sci. Part A: Polym. Chem.* **2009**, 47, 973.
- [83] M.-C. Yuan, M.-H. Su, M.-Y. Chiu, and K.-H. Wei, *J. Polym. Sci. Part A: Polym. Chem.* **2010**, 48, 1298.
- [84] F. Huang, K.-S. Chen, H.-L. Yip, S. K. Hau, O. Acton, Y. Zhang, J. D. Luo, A. K.-Y. Jen, *J. Am. Chem. Soc.* **2009**, 131, 13886.
- [85] S. Zhang, Y. Guo, H. Fan, Y. Liu, H.-Y. Chen, G. Yang, X. Zhan, Y. Liu, Y. F. Li, and Y. Yang, *J. Polym. Sci. Part A: Polym. Chem.* **2009**, 47, 5498.
- [86] B. Y. Yu, A. Tsai, S. P. Tsai, K. T. Wong, Y. Yang, C. W. Chu, and J. J. Shyue, *Nanotechnology* **2008**, 19, 255202.
- [87] W. Ma, C. Yang, X. Gong, K. Lee, and A. J. Heeger, *Adv. Funct. Mater.* **2005**, 15, 1617.
- [88] C. Y. Kwong, W. C. H. Choy, A. B. Djurisic, P. C. Chui, K. W. Cheng and W.K. Chan, *Nanotechnology* **2004**, 15, 1156.

- [89] Y. T. Chang, S. L. Hsu, M. H. Su, and K. H. Wei, *Adv. Funct. Mater.* **2007**, 17, 3326.
- [90] Y. T. Chang, S. L. Hsu, G. Y. Chen, M. H. Su, K. H. Wei, T. A. Singh and E. W. G. Diau, *Adv. Funct. Mater.* **2008**, 18, 2356.
- [91] J. Y. Kim, K. Lee, N. E. Coates, D. Moses, T. Q. Nguyen, M. Dante, and A. J. Heeger, *Science* **2007**, 317, 222.
- [92] G. Li, V. Shrotriya, J. Huang, Y. Yao, T. Moriarty, K. Emery, and Y. Yang, *Nat. Mater.* **2005**, 4, 864.
- [93] A. Hadipour, B. D. Boer, and P. W. M. Blom, *Adv. Funct. Mater.* **2008**, 18, 1.
- [94] J. T. Chen, M. Zhang, and T. P. Russell, *Nano Lett.* **2007**, 7, 183.
- [95] M. Steinhart, R. B. Wehrspohn, U. Gosele, and J. H. Wendorff, *Angew. Chem. Int. Ed.* **2004**, 43, 1334.
- [96] S. H. Lee, D. H. Park, K. Kim, and J. Joo, *Appl. Phys. Lett.* **2007**, 91, 263102.
- [97] K. M. Coakley, B. S. Srinivasan, J. M. Ziebarth, C. Goh, Y. Liu, and M. D. McGehee, *Adv. Funct. Mater.* **2005**, 15, 1927.
- [98] O. G. Reid, K. Munechika, and D. S. Ginger, *Nano Lett.* **2008**, 8, 1602.
- [99] V. D. Mihaiketchi, H. Xie, B. D. Boer, L. J. A. Koster, and P. W. M. Blom, *Adv. Funct. Mater.* **2006**, 16, 699.
- [100] D. Duche, L. Escoubas, J. J. Simon, P. Torchio, W. Vervisch, and F. Flory, *Appl. Phys. Lett.* **2008**, 92, 193310.
- [101] A. C. Mayer, S. R. Scully, B. E. Hardin, M. W. Rowell, and M. D. McGehee, *Mater. Today* **2007**, 10, 28.
- [102] H. S. Wang, L. H. Lin, S. Y. Chen, Y. L. Wang, and K. H. Wei, *Nanotechnology* **2009**, 20, 075201.
- [103] Z. Xu, L. M. Chen, G. Yang, C. H. Huang, J. Hou, Y. Wu, G. Li, C. S. Hsu, and Y. Yang, *Adv. Funct. Mater.* **2009**, 19, 1227.

- [104] J. Jo, S. I. Na, S. S. Kim, T. W. Lee, Y. Chung, S. J. Kang, D. Vak, and D. Y. Kim, *Adv. Funct. Mater.* **2009**, 19, 2398.
- [105] C. Melzer, E. J. Koop, V. D. Mihailetschi, and P. W. M. Blom, *Adv. Funct. Mater.* **2004**, 14 865.
- [106] V. D. Mihailetschi, L. J. A. Koster, P. W. M. Blom, C. Melzer, B. de Boer, J. K. J. van Duren, R. A. J. Janssen, *Adv. Funct. Mater.* **2005**, 15, 795.
- [107] A. M. Ramos, M. T. Rispens, J. K. J. van Duren, J. C. Hummelen, and R. A. J. Janssen, *J. Am. Chem. Soc.* **2001**, 123, 6714.
- [108] G. Kalita, S. Adhikari, H. R. Aryal, R. Afre, T. Soga, M. Sharon, W. Koichi and M. Umeno, *J. Phys. D: Appl. Phys.* **2009**, 42, 115104.
- [109] K. Tajima, Y. Suzuki, and K. Hashimoto, *J. Phys. Chem. C* **2008**, 112, 8507.
- [110] C. Ego, D. Marsitzky, S. Becker, J. Zhang, A. C. Grimsdale, K. Müllen, J. D. MacKenzie, C. Silva and R. H. Friend, *J. Am. Chem. Soc.* 2003, 125, 437.
- [111] S. M. Tuladhar, S. A. Choulis, C. B. Nielsen, W. N. George, J. H.G. Steinke, D. D. C. Bradley and J. Nelson, *Org. Electron.* **2009**, 10, 562.
- [112] F.-C. Chen and C.-H. Lin, *J. Phys. D: Appl. Phys.* **2010**, 43, 025104.
- [113] K. Kim, J. Liu, M. A. G. Namboothiry and D. L. Carroll, *Appl. Phys. Lett.* **2007**, 90, 163511.
- [114] Y. Kim, S. Cook, S. M. Tuladhar, S. A. Choulis, J. Nelson, J. R. Durrant, D. D. C. Bradley, M. Giles, I. McCulloch, C.-S. Ha, and M. Ree, *Nat. Mater.* **2006**, 5, 197.
- [115] Y.-Y. Lin, T.-H. Chu, S.-S. Li, C.-H. Chuang, C.-H. Chang, W.-F. Su, C.-P. Chang, M.-W. Chu and C.-W. Chen, *J. Am. Chem. Soc.* **2009**, 131, 3644.
- [116] W. J. E. Beek, M. M. Wienk and R. A. J. Janssen, *Adv. Funct. Mater.* **2006**, 16, 1112.
- [117] S. Gunes, K. P. Fritz, H. Neugebauer, N. S. Sariciftci, S. Kumar and G. D.

- Scholes, *Sol. Energ. Mat. Sol. C.* **2007**, 91, 420.
- [118] H. S. Wang, S. Y. Chen, M. H. Su, Y. L. Wang and K. H. Wei, *Nanotechnology* **2010**, 21, 145203.
- [119] J.-S. Huang, C.-Y. Chou, M.-Y. Liu, K.-H. Tsai, W.-H. Lin and C.-F. Lin, *Org. Electron.* **2009**, 10, 1060.
- [120] Q. Wei, K. Hirota, K. Tajima, and K. Hashimoto, *Chem. Mater.* **2006**, 18, 5080.
- [121] K. Takanezawa, K. Hirota, Q.-S. Wei, K. Tajima and K. Hashimoto *J. Phys. Chem. C* **2007**, 111, 7218.
- [122] S. Günes, H. Neugebauer, N. S. Sariciftci, J. Roither, M. Kovalenko, G. Pillwein and W. Heiss, *Adv. Funct. Mater.* **2006**, 16, 1095.
- [123] P. D. Cozzoli, A. Kornowski and H. Weller, *J. Am. Chem. Soc.* **2003**, 125, 14539.
- [124] Y.-T. Lin, T.-W. Zeng, W.-Z. Lai, C.-W. Chen, Y.-Y. Lin, Y.-S. Chang and W.-F. Su, *Nanotechnology* **2006**, 17, 5781.
- [125] D. A. M. Egbe, L. H. Nguyen, K. Schmidtke, A. Wild, C. Sieber, S. Guenes, and N. S. Sariciftci, *J. Polym. Sci. Part A: Polym. Chem.* **2007**, 45, 1619.
- [126] W. H. Tang, T. Kietzke, P. Vemulamada, and Z.-K. Chen, *J. Polym. Sci. Part A: Polym. Chem.* **2007**, 45, 5266.
- [127] F. Zhang, E. Perzon, X. J. Wang, W. Mammo, M. R. Andersson, and O. Inganäs, *Adv. Funct. Mater.* **2005**, 15, 745.
- [128] Y. Lee, K.-I. Fukukawa, J. Bang, C. J. Hawker, and J. K. Kim, *J. Polym. Sci. Part A: Polym. Chem.* **2008**, 46, 8200.
- [129] Y. J. He, W. P. Wu, Y. Q. Liu, and Y. F. Li, *J. Polym. Sci. Part A: Polym. Chem.* **2009**, 47, 5304.
- [130] K. Sivula, Z. T. Ball, N. Watanabe, and J. M. J. Fréchet, *Adv. Mater.* **2006**, 18, 206.

- [131] T. Erb, U. Zhokhavets, G. Gobsch, S. Raleva, B. Stühn, P. Schilinsky, C. Waldauf, and C. J. Brabec, *Adv. Funct. Mater.* **2005**, 15, 1193.
- [132] S.-C. Kim, S.-M. Park, J. S. Park, S.-J. Lee, S.-H. Jin, Y.-S. Gal, and J. W. Lee, *J. Polym. Sci Part A: Polym. Chem.* **2008**, 46, 1098.
- [133] Z.-K. Chen, H. Meng, Y.-H. Lai, and W. Huang, *Macromolecules* **1999**, 32, 4351.
- [134] J. A. Mikroyannidis, I. K. Spiliopoulos, T. S. Kasimis, A. P. Kulkarni, and S. A. Jenekhe, *J. Polym. Sci. Part A: Polym. Chem.* **2004**, 42, 2112.
- [135] S. H. Jin, M. Y. Kim, J. Y. Kim, K. Lee, and Y. S. Gal, *J. Am. Chem. Soc.* **2004**, 126, 2474.
- [136] B. Rev Schultz, M. Bruma, and L. Brehmer, *Adv. Mater.* **1997**, 9, 601.
- [137] Y. Zhang, F. Huang, Y. Chi, and A. K.-Y. Jen, *Adv. Mater.* **2008**, 20, 1565.
- [138] P. Wang, C. P. Chai, F. Z. Wang, Y. T. Chuai, X. F. Chen, X. H. Fan, D. C. Zou, and Q. F. Zou, *J. Polym. Sci Part A: Polym. Chem.* **2008**, 46, 1843.
- [139] C. Adachi, T. Tsutsui, and S. Saito, *Appl. Phys. Lett.* **1989**, 55, 1489.
- [140] K. Lee, H.-J. Kim, J. C. Cho, and J. S. Kim, *Macromolecules* **2007**, 40, 6457.
- [141] S. P. Huang, J. L. Liao, H. E. Tseng, T. H. Jen, J. Y. Liou, and S. A. Chen, *Synth. Met.* **2006**, 156, 949.
- [142] S. P. Wen, J. N. Pei, Y. H. Zhou, L. L. Xue, B. Xu, Y. W. Li, and W. J. Tian, *J. Polym. Sci. Part A: Polym. Chem.* **2009**, 47, 1003.
- [143] R. D. McCullough, R. D. Lowe, M. Jayaraman, and D. L. Anderson, *J. Org. Chem.* **1993**, 58, 904.
- [144] M. C. Iovu, E. E. Sheina, R. R. Gil, and R. D. McCullough, *Macromolecules* **2005**, 38, 8649.
- [145] E. E. Sheina, S. M. Khersonsky, E. G. Jones, and R. D. McCullough, *Chem Mater.* **2005**, 17, 3317.

- [146] L.-H. Xie, T. Fu, X.-Y. Hou, C. Tang, Y.-R. Hua, R.-J. Wang, Q.-L. Fan, B. Peng, W. Wei, and W. Huang, *Tetrahedron Lett.* **2006**, 47, 6421.
- [147] M. Nicolas, B. Fabre, G. Marchand, and J. Simonet, *Eur. J. Org. Chem.* **2000**, 1703.
- [148] M. Greczmiel, and P. Strohriegl, *Macromolecules* **1997**, 30, 6042.
- [149] J. Pommerehne, H. Vestweber, W. Guss, R. F. Mahrt, H. Bäessler, M. Porsch, and J. Daub, *Adv. Mater.* **1995**, 7, 551.
- [150] P. Schilinsky, U. Asawapirom, U. Scherf, M. Biele, and C. J. Brabec, *Chem. Mater.* **2005**, 17, 2175.



著作目錄

1. Chia-Hung Chou, So-Lin Hsu, Siao-Wei Yeh, **Hsu-Shen Wang**, Kung-Hwa Wei
“Enhanced Luminance and Thermal Properties of Polyphenylenevinylene Copolymer
Presenting Side-Chain-Tethered Silsesquioxane Units” *Macromolecules* **2005**, *38*,
9117. (SCI; IF: 4.539)
2. Chia-Hung Chou, **Hsu-Shen Wang**, Kung-Hwa Wei and Jung Y. Huang,
“Thiophenol-modified CdS nanoparticles enhance the luminescence of benzoxy
dendron-substituted polyfluorene copolymers,” *Advanced Functional Materials* **2006**,
16, 909, (SCI; IF: 6.990)
3. **Hsu-Shen Wang**, Li-Hua Lin, Shih-Yung Chen, Yuh-Lin Wang, and Kung-Hwa Wei,
“Ordered Polythiophene/Fullerene Composite Core–Shell Nanorod Arrays for Solar
Cell Applications”, *Nanotechnology*, **2009** *20*, 075201. (SCI; IF: 3.137)
4. **Hsu-Shen Wang**, Shih-Yung Chen, Ming-Hsin Su, Yuh-Lin Wang and
Kung-Hwa Wei, “Inverted Heterojunction Solar Cells Incorporating Fullerene/
Polythiophene Composite Core/Shell Nanorod Arrays”, *Nanotechnology*, **2010** *21*,
145203. (SCI; IF: 3.137)
5. **Hsu-Shen Wang**, Ming-Shin Su, and Kung-Hwa Wei, “Synthesis and
Characterization of Donor–Acceptor Poly(3-hexylthiophene) Copolymers Presenting
1,3,4-Oxadiazole Units and Their Application to Photovoltaic Cells”, *Journal of
Polymer Science Part A: Polymer Chemistry*, **2010** *48*, 3331. (SCI; IF: 3.971)
6. **Hsu-Shen Wang**, Shih-Yung Chen, Yuh-Lin Wang, and Kung-Hwa Wei,
“Nanostructured Arrays Presenting TiO₂ nanorods/ Poly(3-hexylthiophene) for Solar
Cells Application”, *Journal of Nanoscience and Nanotechnology*, **2010** accepted. (SCI;
IF: 1.435)

----- Original Message -----

From: "Alex Wotherspoon" <nano@iop.org>

To: <khwei@mail.nctu.edu.tw>

Sent: Monday, March 22, 2010 8:32 AM

Subject: Your article in **Nanotechnology Highlights of 2009**

> Dear Professor Wei,

>

> **Nanotechnology Highlights of 2009**

>

> I am pleased to inform you that your article has been selected to be part
> of Nanotechnology's Highlights of 2009 collection. As part of this
> collection, your article will be free to read until the end of 2010 to gain
> maximum exposure and readership. We have also produced a brochure
> showcasing your abstract along with the collection to distribute at
> international nanotechnology conferences throughout the year.

>

> If you would like to share this news with your colleagues, please pass on
> the following links for the online collection and the brochure.

> -----

> Online Highlights of 2009 collection

> <http://herald.iop.org/nanohighlights/m62/ljc/240521/link/3326>

>

> Download the Nanotechnology Highlights brochure

> <http://herald.iop.org/highlightsbrochure/m62/ljc/240521/link/3327>

> -----

> Congratulations once again, and thank you for contributing such an
> excellent article to the journal, I look forward to working with you again
> in the near future.

>

> With kind regards,

>

> Alex Wotherspoon

> Publisher

> Nanotechnology

> *Data Protection*

> The Institute of Physics (and other companies in its group, including IOP
> Publishing Limited) may like to send you further notifications like this.

> If you would prefer not to receive these, then please reply to this e-mail
> with the word "unsubscribe" in the subject line. We will never rent or
> sell your e-mail address to any third parties.

>

學經歷資料



- 姓名：王旭生
- 性別：男
- 生日：67 年 11 月 28 日
- 電子郵件信箱：mongalbbs.mse93g@nctu.edu.tw
- 聯絡電話：(學校) 03-5731771 (手機) 0937935972
- 通訊地址：新竹市 300 大學路 1001 號
國立交通大學材料與工程研究所
永久地址：台北縣土城市青雲路 110 巷 7 號

學歷

- | | |
|------------------------|-------------------|
| 博士候選人：國立交通大學材料科學與工程研究所 | 2004. 9 ~ 2010. 7 |
| 研究所：國立中央大學化學研究所 | 2002. 9 ~ 2004. 6 |
| 大學：靜宜大學應用化學系 | 1998. 9 ~ 2002. 6 |

專長

- 有機光電材料(Polymer Solar cell)：
 1. 元件奈米結構製備與分析
 2. 奈米顆粒及奈米複合材料。
 3. 新穎材料分子設計及合成。
- 有機/無機奈米複合材料：
 1. 無機物/高分子混成材之奈米結構及界面改質分散技術。
- 分析儀器操作：

原子力顯微鏡(AFM; conducting, tapping, contact mode, DI Multimode 管理者, D3100)、穿透式電子顯微鏡(TEM, JEOL 2010, FEI Spirit TWIN 120 keV)、掃描式電子顯微鏡(SEM, JEOL 6500, JEOL 6700)、核磁共振光譜儀(Varian NMR and Bruker NMR)、微差掃描卡計(DSC)、熱重量分析儀(TGA)、質譜儀(Mass)、凝膠滲透層析儀(GPC)、微光光譜儀(Uv-vis)、螢光光譜儀(PL)、循環伏安計(CV)、 α -step 薄膜測厚儀、超薄切片機、拉曼光譜儀、紅外線光譜儀(FT-IR)。有機光電元件製作機台(蒸鍍機、手套箱、UVO-Cleaner、元件封膠機、旋轉塗佈機(Spin coater)、實際參與機台設計與架設)、太陽光電量測設備(Keithley 236, 太陽光模擬器、外部量子效率量測設備, 參與儀器架設)、交通大學奈米中心無塵室使用資格。